Parameterization of clinopyroxene growth kinetics via crystal size distribution (CSD) analysis: Insights into the temporal scales of magma dynamics at Mt. Etna volcano

[1*]Piergiorgio Moschini, [1,2]Silvio Mollo, [1]Mario Gaeta, [3]Sara Fanara, [2]Manuela Nazzari, [4]Chiara Maria Petrone, [2]Piergiorgio Scarlato

[1]Department of Earth Sciences, Sapienza - University of Rome, P. le Aldo Moro 5, 00185 Roma, Italy

[2]Istituto Nazionale di Geofisica e Vulcanologia - Department Roma 1, Via di Vigna Murata 605, 00143 Roma, Italy

[3]Abteilung Experimentelle und Angewandte Mineralogie, Georg August Universität Göttingen, Goldschmidtstraße 1, 37077 Göttingen, Germany

[4]The Natural History Museum, Department of Earth Sciences, Cromwell Road, SW7 5BD, London, United Kingdom

*Corresponding author:
Piergiorgio Moschini
piergiorgio.moschini@uniroma1.it
Department of Earth Sciences
Sapienza - University of Rome
P. le Aldo Moro 5
00185 Roma, Italy

Abstract

There is increasing recognition that both textural and compositional changes of clinopyroxene crystallizing from mafic alkaline magmas are the direct expression of complex dynamic processes extending over a broad range of spatial and temporal scales. Among others, supersaturation and relaxation phenomena play a key role in controlling the final crystal cargo of variably undercooled magmas erupted from active alkaline volcanoes. Following this line of reasoning, we have carried out isothermal-isobaric, decompression, and cooling rate experiments on a basalt interpreted as the parental magma of mafic alkaline eruptions at Mt. Etna volcano (Sicily, Italy). The main purpose is to reconstruct and quantify the textural changes (i.e., length of major and minor axes, surface area per unit volume, area fraction, and maximum growth rate) of clinopyroxene at variable pressures (30-300 MPa), temperatures (1,050-1,100 °C), volatile contents (0-5 wt.% H_2O and 0-0.2 wt.% CO_2), and equilibration times (0.25-72 h). Melt supersaturation, corresponding to a degree of undercooling variable from 14 to 125 °C, drives the formation of clinopyroxene crystals with different textures and sizes as a function of growth rate and relaxation time. By integrating experimental data and thermodynamic modeling, the transition between interface-controlled (euhedral morphologies) and diffusion-controlled (anhedral morphologies) growth regimes has been determined to occur at degrees of undercooling higher than 30 °C. The decrease of clinopyroxene growth rate with increasing the equilibration time is combined with the crystal size distribution (CSD) analysis of naturally undercooled clinopyroxene crystals erupted during 2011-2012 lava fountain episodes at Mt. Etna volcano. Results indicate that the crystallization of microlites and microphenocrysts is on the order of ~10^0-10^1 min (large undercooling, short equilibration time) and ~10^1-10^2 h (small undercooling, long equilibration time), respectively. This temporal information allows to better constrain the cooling-decompression paths of Etnean magmas rising and accelerating along a vertically extended, highly dynamic plumbing system. While clinopyroxene microlites develop during the fast ascent of magmas (~10^0-10^1 m s^{-1}) within the uppermost part of the conduit or immediately before ejection from the vent, the onset of microphenocryst crystallization occurs at depth and continues within the plumbing system during the slow ascent of magmas (~10^{-2} m s^{-1}) that migrate through interconnected storage regions.

Keywords: basalt; clinopyroxene; crystallization kinetics; crystal size distribution (CSD); magma cooling and decompression; magma ascent rate; Mt. Etna volcano.

Research Highlights

Clinopyroxenes from magmas erupted at Mt. Etna volcano have been investigated

Undercooling and relaxation time control the crystal growth rate and euhedrality

Time scales of magma dynamics are quantified by textural parameterization and CSD

Microlites record fast ascent of magmas along the uppermost part of the conduit

Microphenocrysts reflect slow growth within interconnected reservoirs at depth

Parameterization of clinopyroxene growth kinetics via crystal size distribution (CSD) analysis: Insights into the temporal scales of magma dynamics at Mt. Etna volcano

[1*]Piergiorgio Moschini, [1,2]Silvio Mollo, [1]Mario Gaeta, [3]Sara Fanara, [2]Manuela Nazzari, [4]Chiara Maria Petrone, [2]Piergiorgio Scarlato

[1]Department of Earth Sciences, Sapienza - University of Rome, P. le Aldo Moro 5, 00185 Roma, Italy

[2]Istituto Nazionale di Geofisica e Vulcanologia - Department Roma 1, Via di Vigna Murata 605, 00143 Roma, Italy

[3]Abteilung Experimentelle und Angewandte Mineralogie, Georg August Universität Göttingen, Goldschmidtstraße 1, 37077 Göttingen, Germany

[4]The Natural History Museum, Department of Earth Sciences, Cromwell Road, SW7 5BD, London, United Kingdom

*Corresponding author:
Piergiorgio Moschini
piergiorgio.moschini@uniroma1.it
Department of Earth Sciences
Sapienza - University of Rome
P. le Aldo Moro 5
00185 Roma, Italy

Abstract

There is increasing recognition that both textural and compositional changes of clinopyroxene crystallizing from mafic alkaline magmas are the direct expression of complex dynamic processes extending over a broad range of spatial and temporal scales. Among others, supersaturation and relaxation phenomena play a key role in controlling the final crystal cargo of variably undercooled magmas erupted from active alkaline volcanoes. Following this line of reasoning, we have carried out isothermal-isobaric, decompression, and cooling rate experiments on a basalt interpreted as the parental magma of mafic alkaline eruptions at Mt. Etna volcano (Sicily, Italy). The main purpose is to reconstruct and quantify the textural changes (i.e., length of major and minor axes, surface area per unit volume, area fraction, and maximum growth rate) of clinopyroxene at variable pressures (30-300 MPa), temperatures (1,050-1,100 °C), volatile contents (0-5 wt.% H_2O and 0-0.2 wt.% CO_2), and equilibration times (0.25-72 h). Melt supersaturation, corresponding to a degree of undercooling variable from 14 to 125 °C, drives the formation of clinopyroxene crystals with different textures and sizes as a function of growth rate and relaxation time. By integrating experimental data and thermodynamic modeling, the transition between interface-controlled (euhedral morphologies) and diffusion-controlled (anhedral morphologies) growth regimes has been determined to occur at degrees of undercooling higher than 30 °C. The decrease of clinopyroxene growth rate with increasing the equilibration time is combined with the crystal size distribution (CSD) analysis of naturally undercooled clinopyroxene crystals erupted during 2011-2012 lava fountain episodes at Mt. Etna volcano. Results indicate that the crystallization of microlites and microphenocrysts is on the order of ~10^0-10^1 min (large undercooling, short equilibration time) and ~10^1-10^2 h (small undercooling, long equilibration time), respectively. This temporal information allows to better constrain the cooling-decompression paths of Etnean magmas rising and accelerating along a vertically extended, highly dynamic plumbing system. While clinopyroxene microlites develop during the fast ascent of magmas (~10^0-10^1 m s^{-1}) within the uppermost part of the conduit or immediately before ejection from the vent, the onset of microphenocryst crystallization occurs at depth and continues within the plumbing system during the slow ascent of magmas (~10^{-2} m s^{-1}) that migrate through interconnected storage regions.

Keywords: basalt; clinopyroxene; crystallization kinetics; crystal size distribution (CSD); magma cooling and decompression; magma ascent rate; Mt. Etna volcano.

1. Introduction

Clinopyroxene is an important recorder of the physico-chemical changes explored by mafic alkaline magmas typically occurring in intraplate settings. Owing to its ubiquitous crystallization over a broad range of pressures, temperatures, and volatile contents (e.g., Mollo et al., 2018), a gamut of studies have investigated the clinopyroxene textural and compositional variations in alkaline products, with the main purpose of elucidating pre-eruptive magma storage conditions at depth and syn-eruptive dynamics during ascent of magma towards the surface (e.g., Petrone et al., 2016, 2018; Ubide and Kamber, 2018).

While the stability field of clinopyroxene is intrinsically related to the intensive and extensive variables governing the thermodynamic reactions at the interface between crystal, melt, and fluid phases, a certain degree of undercooling (ΔT) is essential to promote the growth and textural maturation of clinopyroxene. ΔT is the thermodynamic driving force of crystallization and can be defined as the difference between the temperature at which a specific mineral saturates the melt and the temperature of a naturally solidifying system. In single-step undercooling experiments characterized by a rapid, large drop in pressure-temperature, the melt composition can be assumed constant during the decompression-cooling path controlling ΔT. As a consequence, the degree of supersaturation of the mineral-forming components can be linked and quantified directly through the magnitude of ΔT (Shea and Hammer, 2013 and references therein). Several reviews examined the phenomenological aspects related to the kinetics of crystal nucleation and growth (e.g., Kirkpatrick, 1981; Cashman, 1990; Lasaga, 1998; Hammer, 2006; Iezzi et al., 2014; Mollo and Hammer, 2017; Giuliani et al., 2020), along with increasing emphasis on the importance of magma supersaturation state to resolve specific petrological and volcanological problems involving the environmental conditions of magmatic reservoirs and their dynamic evolutions.

Recently, some authors (Hammer et al., 2016; Welsch et al., 2016; Ubide et al., 2019a, 2019b; Di Stefano et al., 2020) focused their attention on the profound effect exercised by ΔT on the morphology and composition of clinopyroxene growing from mafic alkaline magmas, such as those erupted at Haleakala (Hawaii) and Mt. Etna and Stromboli (Italy). These authors documented that systematic departure from equilibrium arises by composite growth histories driven by imbalance between the rate at which the crystal surfaces advance and the rate of cation diffusion in the melt. In particular, for magmas erupted at Mt. Etna, it has been experimentally found that strong supersaturation effects correspond to large ΔT, leading to disequilibrium uptake of incompatible cations at the crystal-melt interface. These rate-limiting concentration gradients promote high nucleation rates and fast development of small, anhedral clinopyroxene crystals (Polacci et al., 2018; Arzilli et al., 2019; Masotta et al., 2020). Conversely, under the driving force of small ΔT, the bulk system attempts to return to a near-equilibrium

state between the advancing crystal surfaces and the melt composition. Because of the effect of growth kinetics, large, euhedral clinopyroxene crystals develop by minimizing the interfacial free energy between crystal and surrounding melt. Time-series experiments have also outlined that the shift from a diffusion-controlled to an interface-controlled growth regime is intimately governed by relaxation phenomena lowering the concentration gradients at the crystal-melt interface and leading to a steady-state textural maturation of clinopyroxene (Pontesilli et al., 2019). After initial supersaturation effects, the growth rate of clinopyroxene progressively decreases with increasing relaxation time, thereby approaching to a near-equilibrium condition where attachment/detachment reactions of cations from the melt onto the crystalline surface (and *vice versa*) occur at the same rate (Pontesilli et al., 2019). These time-series experiments also corroborate the textural maturation model proposed by Welsch et al. (2016) for the growth of large clinopyroxene phenocrysts from ankaramite lava flows erupted at Haleakala. According to the authors, the external morphology, chemical variation, and internal structure of these phenocrysts testify to a continuous growth rate decrease over time, in response to less effective supersaturation conditions driving gradual transition between diffusion-controlled and interface-controlled regimes (Welsch et al., 2016).

On the basis of previous laboratory data from Pontesilli et al. (2019) and Masotta et al. (2020), we have conducted complementary isothermal-isobaric, decompression, and cooling rate experiments on a primitive basalt from Mt. Etna, in order to assess the control of supersaturation and relaxation phenomena on clinopyroxene crystallization. In agreement with crystal growth thermodynamics and kinetics, the textural maturation of clinopyroxene is attained at small undercoolings and long equilibration times. Under such conditions, we measure a growth rate decay of six orders of magnitude that is modeled as a function of relaxation kinetics. This empirical relationship is interpolated to the algebraic expression of crystal size distribution (CSD) analysis, with the final purpose of quantifying the time scale of crystallization during decompression-cooling of mafic alkaline magmas. As a test case, microlites and microphenocrysts from scoria clasts ejected during 2011-2012 lava fountains at Mt. Etna have been considered. Results from calculations give rise to a conceptual model for the time scale of magma dynamics recorded by the (dis)equilibrium textural evolution of clinopyroxene and for the rapid acceleration of magma ascending within the volcanic conduit, immediately before eruption at the vent.

2. Methods

2.1. Experimental strategy

The starting material used for the experiments is a natural basalt from the Monte Maletto Formation erupted at Mt. Etna around 7,000 years ago. Monte Maletto Formation comprises basaltic to trachybasaltic products that have been interpreted by numerous authors as the parental compositions of historic and recent Etnean eruptions (see the review study of Mollo et al., 2018 and references therein). The powdered rock was melted to ensure homogeneity of the final starting material at the HP-HT Laboratory of Experimental Volcanology and Geophysics of the Istituto Nazionale di Geofisica e Vulcanologia (INGV), Rome, Italy. A crucible containing the natural powder was loaded in a 1 atm vertical tube CO–CO_2 gas-mixing furnace at 1,300 °C for 1 h. The redox state was 2 log unit above the Ni-NiO buffer (NNO+2), comparable to that estimated at the Mt. Etna (Mollo et al., 2015a). Iron loss was kept to < 5% of the initial amount by adopting an Fe pre-saturated Pt crucible. The quenched glass was analyzed by scanning electron microscopy and no crystalline phases were detected. Twenty microprobe analyses of the glass yielded an average composition (in wt.%) of 47.56 (±0.39) SiO_2, 1.48 (±0.11) TiO_2, 15.42 (±0.23) Al_2O_3, 10.79 (±0.17) FeO_{tot}, 0.21 (±0.04) MnO, 7.98 (±0.15) MgO, 12.13 (±0.18) CaO, 2.61 (±0.13) Na_2O, 1.25 (±0.12) K_2O, and 0.57 (±0.04) P_2O_5.

Isothermal and decompression experiments were carried out in an internally heated pressure vessel (IHPV) equipped with a continuum decompression system and a rapid quenching device (drop quench) at the Abteilung Experimentelle und Angewandte Mineralogie, Georg August Universität Göttingen (Germany). The powdered starting glass was loaded in Fe-presaturated Pt-capsules. Isobaric experiments (*Experimental Set ISO*) were conducted at 300 MPa and temperatures of 1,100 (*ISO-1100*), 1,075 (*ISO-1075*), and 1,050 °C (*ISO-1050*) that were kept constant over an equilibration time of ~24 hours (Table 1). The experiments were heated directly to the target temperature at a rate of 50 °C/min and were carried out under nominally anhydrous and hydrous conditions, corresponding to 0 wt.% $H_2O_{initial}$ (*ISO-0H2O*, i.e., nominally anhydrous system), 2 wt.% $H_2O_{initial}$ (*ISO-2H2O*), 5 wt.% $H_2O_{initial}$ (*ISO-5H2O*), and 2 wt.% $H_2O_{initial}$ + 0.2 wt.% $CO_{2initial}$ (*ISO-H2O+CO2*). H_2O and CO_2 were added as deionized water and oxalic acid, respectively. Decompression experiments (*Experimental Set ΔP*) were conducted at the same temperatures and anhydrous-hydrous conditions by depressurizing the charges from 300 to 30 MPa at slow (*ΔPs*) and fast (*ΔPf*) rates of 0.018 and 0.98 MPa s^{-1}, respectively (Table 1). Pressures, temperatures, and melt-H_2O+CO_2 contents have been selected in order to reproduce the most common crystallization-degassing path of magmas at Mt. Etna, as derived by thermobarometric-hygrometric calculations and melt inclusion data (Mollo et al., 2018 and references therein). Slow to fast decompression experiments correspond to magma ascent velocities in the range of 0.45-24.5 m s^{-1}, in agreement with previous estimates suggested by geophysical, crystallochemical, and numerical studies

focusing on magma conduit dynamics at Mt. Etna (Aloisi et al., 2006; Mollo et al., 2015b; La Spina et al., 2016; Giuffrida et al., 2017). Note that the solubility of H_2O in this melt composition is ~2.9 and ~0.5 wt.% at 300 (i.e., fluid-absent) and 30 (i.e., fluid-present) MPa, respectively, as derived by the thermodynamic model of Duan (2014) and corroborated by numerous studies carried out on mafic alkaline magmas (Mollo et al., 2018 and references therein). Coherently, magma dynamics at Mt. Etna volcano are frequently recognized as the result of complex crystallization regimes that, at shallow crustal levels, change from H_2O-undersaturated to H_2O-saturated (i.e., $P_{H2O} = P_{total}$) conditions, in conjunction with abundant volatile degassing (Mollo et al., 2015b, 2018; Perinelli et al., 2016, 2018). The temperature was monitored by three S-type (Pt90Rh10/Pt with uncertainty of ±3 °C) thermocouples and pressure was recorded by a transducer, calibrated against a Heise tube gauge with accuracy ±5 MPa. Experiments were quenched using a drop quench device imposing a cooling rate of ~150 °C s^{-1}. Recovered charges were mounted in epoxy and polished thin sections was produced from the epoxy blocks. The use of Ar as a pressure medium provided an intrinsic fO_2 variable from NNO+2 to NNO+4 (Schanofski et al., 2019). Within the sample capsule, fH_2 was controlled by hydrogen permeation through the capsule walls driven by the fugacity gradient between the pressure medium and the capsule interior. This in turn determined the fO_2 inside the capsule through the equilibrium $H_2 + 1/2\ O_2 \leftrightarrow H_2O$. However, under fluid-present conditions and with the addition of CO_2, the redox state of the system changed in response to the variable activity of H_2O in the melt (Botcharnikov et al. 2008). In this respect, the redox state of the system was estimated at the end of experimental runs through the oxygen barometer of Ishibashi (2013) based on spinel–melt equilibria and with uncertainty (±0.3 log unit). This model was calibrated using an alkaline data set, returning fO_2 estimates variable from NNO+1.9 and NNO+2.3 buffer (Mollo et al., 2015a).

Cooling rate experiments (Table 1) were carried out in a non-end loaded piston cylinder apparatus ("QUICKpress", Depths of the Earth co.) using a 19-mm NaCl-pyrex-graphite-MgO assembly that produced an apparent redox state close to NNO+2 buffer (Mollo and Masotta, 2014). The assembly was loaded with a Fe-presaturated Pt-capsule containing the hydrous (2 wt.% $H_2O_{initial}$) glass. The capsules were surrounded by powdered pyrophyllite to prevent H_2O loss and enhance stress homogenization during initial compression. After cold pressurization to a nominal pressure 10% higher than desired, the pressure was decreased down to 300 MPa. The temperature was monitored by a factory-calibrated C-type (W-5Re/W-26Re) thermocouple, which gives an uncertainty of ±3 °C. Following Masotta et al. (2020), the experiments were carried out by heating the starting glass to superliquidus condition of 1,300 °C at a rate of 80 °C min^{-1}. After 30 min, the temperature was cooled to 1,050 °C at the same rate of 80 °C min^{-1} (*Experimental Set CR*). This isothermal condition was kept constant for 0.25 (*CR-025*),

0.5 (*CR-05*), 1 (*CR-1*), 4 (*CR-4*), 24 (*CR-24*), and 72 (*CR-72*) hours, before isobaric quench at a rate of 100 °C s^{-1} (Table 1).

As a whole, *Experimental Set ISO*, *Experimental Set ΔP*, and *Experimental Set CR* were carried out at the temperatures (i.e., 1,100, 1,075, and 1,050 °C) more frequently encountered during the crystallization of clinopyroxene at Mt. Etna volcano (e.g., Mollo et al., 2018). Similarly, the pressure condition of 300 MPa corresponds to a magma storage region at an intermediate depth of 7-13 km (Murru et al., 1999) where microphenocrysts of clinopyroxene initiate to nucleate and grow during magma ascent towards the surface (e.g., Mollo et al., 2015b). In this context, *Experimental Set ISO* approached from the solidus directly to the subliquidus temperature (i.e., nominal $\Delta T = 0$) in order to quantify the textural parameters of clinopyroxene under interface-controlled growth regimes. Conversely, *Experimental Set ΔP* and *Experimental Set CR* were designed to impose variable supersaturation conditions (i.e., actual ΔT = 14-125 °C; Table 1), leading to diffusion-controlled growth regimes and clinopyroxene textural changes.

2.2. Image processing and CSD correction

Photomicrographs of the experimental products were collected in backscattered electron (BSE) mode of a JEOL 6500F field emission gun scanning electron microscope (FE-SEM) equipped with an energy-dispersive spectrometer (EDS) detector at the HP-HT Lab of INGV.

The acquired photomicrographs were processed via NIH Image J software and reduced to binary type images (i.e., black and white color) by grey level thresholding (i.e., image segmentation; Armienti, 2008). The segmentation method was employed to identify clinopyroxene microphenocrysts and microlites relative to other mineral phases (Fig. 1). The uncertainty associated with the segmentation process and the identification of larger crystals growing by attachment of smaller ones has been evaluated according to the method reported in Pontesilli et al. (2019) and based on the addition/subtraction of pixel layers around each crystal in the binary image. A Matlab© code (see Supplementary Material 1) was developed to perform image processing operations in conjunction with NIH Image J. The retrieved textural parameters were 1) the equal-area best-fit ellipses and lengths of major (L) and minor (W) axes (Fig. 1), 2) the surface area per unit volume (S_v^P as 3D aspect ratio; Table1), and 3) the area fraction of a given population within a plane that is comparable to its volume fraction (ϕ). Following one of the most common methods reported in literature (cf. Pontesilli et al., 2019 and references therein), L and W data were used to calculate the maximum growth rate (G_{max} in mm s^{-1}) of clinopyroxene, as an average of the ten largest crystals measured in each experimental run (Supplementary Material 2):

$$G_{max} = (L\ W)^{0.5} / (2\ t) \quad (1)$$

where t is the experimental time.

The magnitude of S_v^P was determined for the experimental crystals as (Hammer, 2006; First and Hammer, 2016):

$$S_v^P = S_v^T / \phi \quad (2)$$

S_v^T is the total interfacial area of a population per unit volume of sample and can be expressed as $2 \times N_L$, where N_L is the density of phase boundary intersections in a given length of randomly oriented test line. The Matlab© code from this study allows to overlay the desired number of circular test lines over a binary type image (Fig. 1) and determine the N_L value by counting the locus of points where crystal-melt boundaries intersect the test lines. The lower is the magnitude of S_v^P parameter, the higher is the crystal euhedrality. Therefore, clinopyroxene crystals characterized by S_v^P < 1,000 mm^{-1} are interpreted as euhedral, whereas crystal with S_v^P >1,000 mm^{-1} are anhedral (Hammer, 2008). S_v^P data listed in Table 1 are the mean resulting from the analysis of eight binary type images for sample, each one overlaid by six circles with radius variable as a function of BSE image magnification (Fig. 1).

CSD analysis was carried out on BSE images of natural rock samples from 2011-2012 lava fountains outpoured at Mt. Etna volcano. Textural data were collected at ×500 and ×100 magnifications for microlites (<0.1 mm) and microphenocrysts (≥0.1 mm) populations, respectively, and then combined each other to obtain one single CSD curve. Intersection planar data were converted in volume data by applying stereological correction (Higgins, 2000), in order to gain information on the contribution of larger crystals to the population of smaller ones. This correction method accounts for 1) potential cut-section effects in case of larger crystals are cut by a plane shifted with respect to the center, therefore contributing to smaller crystal populations, and 2) intersection probability effects when, for a poly-disperse distribution, smaller crystals are less likely to be intersected by a plane than larger crystals (Higgins, 2000). The crystal shape, assumed as the crystal aspect ratio S:I:L of short:intermediate:long dimensions (Higgins, 2000), was determined by the Excel© spreadsheet *CSDslice* developed by Morgan and Jerram (2006). Through this model, 2D raw data were compared with a crystal habit database (i.e., S:I:L of 1:10:10, 1:1:10, and 1:1:1) to constrain the five best-matching crystal shapes. The best linear binning was selected for each sample by the procedure reported in Armienti (2008) for the minimization

of residuals between the particles effectively measured and those re-calculated by CSD analysis (zeroth moment of the distribution):

$$N_{tot} = Area \sum L_i \, N_V(L_i) \quad (3)$$

where L_i is the major axis length of crystal and N_V is the volumetric number density. This latter parameter is calculated as the ratio of the area number density (N_A) to the characteristic crystal size (L_D). The routine of Armienti (2008) requires also the minimization of residuals between the measured volume crystal fraction and the volume resulting from CSD analysis (third moment of the distribution):

$$V_f = \sum N_V\,(L_i)\,\frac{4}{3}\pi\left(\frac{L_i}{2}\right)^3 = \frac{\pi}{6}\sum {L_i}^3 N_V(L_i) \quad (4)$$

According to Eqns. (3) and (4), a linear binning ΔL of 0.02 mm was derived, for a total of 21 classes ranging from 0.006 to 0.406 mm. Crystals with L < 0.006 mm (i.e., artefacts caused by image segmentation) and crystal fragments at the edge of photomicrographs were removed from the dataset (Armienti et al., 1994). The program *CSDCorrection*s 1.38 of Higgins (2000) was finally employed to calculate a binned CSD curve for different crystal size classes by specifying the crystal shape values reported in Supplementary Material 3, rock fabric of massive type, and crystal roundness factor of 0.5. The formulated CSD diagrams are in the form of semi-logarithmic plots based on ln *N(L)* vs. *L* that describe the evolution of crystal size as (Marsh, 1988):

$$\ln N(L) = \frac{-L}{G\,\tau} + \ln N_0 \quad (5)$$

where *N(L)* is the number of crystals per size of length *L* per unit volume (i.e., the density distribution of crystals per unit volume per bin size), *G* is the crystal growth rate, τ is the time of a system crystallizing at steady state, and N_0 is the nucleation density (i.e., the number of crystals of zero size). When the dominant size of the crystal population results from steady growth over an appropriate duration of time, the linear regression fit of CSD curve has slope $m = 1 / (G \times \tau)$ and intercept $b = \ln(N_0)$. According to previous works focused on crystallization kinetics (see the review study of Giuliani et al., 2020 and references therein), the decrease of *m* with increasing crystal size may reflect the growth of early-formed nuclei by agglomeration and attachment. Under such kinetic growth conditions, both *m* and *b* parameters

286 are strictly correlated with the variation of temperature as a function of time, and G_{max} linearly decreases
287 with decreasing $\Delta T/\Delta \tau$ (cf. Giuliani et al., 2020). CSD statistics were obtained from the quantitative study
288 of 16 thin sections and 243 photomicrographs. CSD plots were constructed considering ~1,500-4,000
289 crystals.
290
291 *2.3. Microanalysis*
292 Major element concentrations were obtained at the HP-HT Lab of INGV using a JEOL-JXA8200
293 electron probe micro-analyzer (EPMA) equipped with five wavelength dispersive spectrometers
294 (Supplementary Material 4). For glasses, a slightly defocused 3 μm beam was used with a counting time
295 of 5 s on background and 15 s on peak. For crystals, beam size was 1 μm with a counting time of 20 and
296 10 s on peak and background, respectively. The following standards were used for calibration: jadeite
297 (Si and Na), corundum (Al), forsterite (Mg), andradite (Fe), rutile (Ti), orthoclase (K), barite (Ba), apatite
298 (P), spessartine (Mn) and chromite (Cr). Sodium and potassium were analyzed first to prevent alkali
299 migration effects. The precision of the microprobe was measured through the analysis of well-
300 characterized synthetic standards. Based on counting statistics, analytical uncertainties relative to their
301 reported concentrations indicate that precision and accuracy were better than 5% for all cations.
302
303 **3. Results**
304 *3.1. Textural features*
305 Selected BSE photomicrographs representative of run products from *Experimental Set ISO*,
306 *Experimental Set ΔP*, and *Experimental Set CR* are displayed in Figs. 1 and 2 (note that photomicrographs
307 of all the experiments are reported in Supplementary Material 2). The mineral assemblage consists of
308 abundant clinopyroxene and titanomagnetite, with subordinate plagioclase (in order of crystallization
309 sequence).
310 Clinopyroxene crystals from *Experimental Set ISO* show euhedral morphologies, with a great
311 number of well-faced crystals (Figs. 1 and 2) and L_{max} variable from 0.07 to 0.23 mm (Supplementary
312 Material 2). Run products are characterized by a dense mosaic of either isolated or aggregated microlites,
313 suggesting rapid attainment of an interface-controlled crystal growth regime. Indeed, most of
314 clinopyroxene crystallization initiated upon crossing the glass transition temperature (Tg = 723 °C,
315 Giordano et al., 2005) and further continued over time (i.e., there is no effective ΔT caused by cooling
316 and/or decompression). The amount of residual glass found in the experimental charges increases with
317 increasing T and $H_2O_{initial}$ (Figs. 1 and 2, and Supplementary Material 2). In contrast, the presence of CO_2

lowers the amount of H_2O dissolved in the melt, raising the liquidus temperature of the experimental system and increasing the crystal content (Supplementary Material 2).

Clinopyroxene crystals from *Experimental Set ΔP* consist of sector-zoned crystals with prismatic shapes and well-formed planar edges (Figs. 1 and 2, and Supplementary Material 2). L_{max} ranges from 0.02 to 0.25 mm, depicting an increasing trend with increasing T and $H_2O_{initial}$. Under slow decompression regimes, the crystal size substantially increases due to the effect of sluggish decompression-driven crystal growth kinetics. Therefore, L_{max} measured for *ΔPs-1100-5H2O* (0.14-0.25 mm) is much higher than that determined for *ΔPf-1100-5H2O* (0.06-0.09 mm). Notably, the lack of anhedral (hopper to dendritic) forms in both *ΔPs* and *ΔPf* experiments accounts for the effect of relative slow *ΔT* (14-30 °C; Table 1), consistently with previous literature data (see the review study of Giuliani et al., 2020).

Clinopyroxene crystals from *Experimental Set CR* show substantial textural differences as a function of relaxation time (Figs. 1 and 2, and Supplementary Material 2). *CR-1050-025*, *CR-1050-05*, and *CR-1050-1* are characterized by the ubiquitous occurrence of acicular and skeletal crystals, whereas *CR-1050-4*, *CR-1050-24*, and *CR-1050-72* exhibit clear euhedral morphologies (Fig. 2 and Supplementary Material 2). The shift from a diffusion-controlled to an interface-controlled crystal growth conditions is marked, taking place in a time interval comprised between 1 and 4 h. Once crystallization proceeds under nucleation-dominated regimes, L_{max} ranges from 0.07 to 0.10 mm for *CR-1050-025*, *CR-1050-05*, and *CR-1050-1*. In contrast, due to superimposition of growth-dominated regimes, L_{max} ranges from 0.08 to 0.25 mm for *CR-1050-4*, *CR-1050-24*, and *CR-1050-72*.

3.2. Crystal content variation

Fig. 3 shows the variation of clinopyroxene content (% area) in *Experimental Set ISO*, *Experimental Set ΔP*, and *Experimental Set CR.*

As the target temperature increases, the degree of crystallization decreases from 28% to 18% and from 21% to 5% for *Experimental Set ISO* and *Experimental Set ΔP*, respectively (Fig. 3a). A similar decrease is attained by increasing $H_2O_{initial}$, whereas the crystal content slightly increases by ~4% when CO_2 is added to the experimental charge.

Experimental Set CR exhibits the highest clinopyroxene content within the whole data set. As the relaxation time increases, the degree of crystallization slightly decreases from 37% to 32% (Fig. 3b). A

modest drop in crystal content takes place in the time interval comprised between 1 and 4 h, once the crystallization regime shifts from nucleation-dominated to growth-dominated regimes.

3.3. Clinopyroxene euhedrality

Fig. 4 shows the variation of S_v^P determined for *Experimental Set ISO, Experimental Set ΔP, and Experimental Set CR.* As temperature and/or H_2O content increase, clinopyroxene S_v^P decreases with decreasing the surface area of crystals per unit volume. Moreover, the probability of phase boundary intersections increases with increasing the number of crystals, thus leading to most of trends defined for S_v^P (Fig. 4).

For *Experimental Set ISO* (730-477 mm^{-1} S_v^P) and *Experimental Set ΔP* (548-113 mm^{-1} S_v^P), the euhedrality of clinopyroxene increases with increasing temperature and $H_2O_{initial}$ (Fig. 4a). Both isothermal and decompression data confirm that values of $S_v^P < 1{,}000$ mm^{-1} account for the development of well-faced morphologies (cf. Hammer, 2008).

On the other hand, the magnitude of crystal euhedrality radically changes in *Experimental Set CR* (Fig. 4b). S_v^P ranges from 1,365 to 1,194 mm^{-1} for *CR-1050-025, CR-1050-05* and *CR-1050-1*. A much more restricted S_v^P range of 896-815 mm^{-1} is measured for *CR-1050-4*, *CR-1050-24*, and *CR-1050-72*. Since the experimental cooling rate was fixed and only the relaxation time was changed, the abrupt variation of S_v^P is a proxy for the control of relaxation time on the crystallization regime, after that the system is subjected to an early stage of undercooling (Arzilli et al., 2018; Pontesilli et al., 2019).

3.4. Compositional features

Chemical changes of residual glasses and coexisting clinopyroxene crystals will be the object of a forthcoming and more comprehensive work on cation partitioning under isobaric-isothermal vs. cooling-decompression conditions. Here we briefly summarize the most important compositional features of the experimental charges (Fig. 5):

1) according to the TAS (total alkali vs. silica) classification diagram, the glass chemistry (Fig. 5a) can be divided into two groups as a function of temperature and $H_2O_{initial}$ conditions (i.e., the degree of crystallization);

2) at high-*T* (1,100 °C), high-$H_2O_{initial}$ contents (5 wt.%), residual melts exhibit basaltic-trachybasaltic compositions (Fig. 5a) similar to those of recent (post-1971) eruptions at Mt. Etna volcano (natural data set from Mollo et al., 2018);

3) at low-*T* (1,050-1,075 °C), low-$H_2O_{initial}$ contents (0-2 wt.%), residual melts are more differentiated, resembling trachybasalts to basaltic trachyandesites erupted during the historic (pre-1971) period of activity (Fig. 5a);

4) clinopyroxene chemistry follows the same evolutionary path depicted by the melt phase, with the exception of sector-zoned crystals obtained under slow and fast decompression conditions (Fig. 5b);

5) at high-*T*, high- $H_2O_{initial}$ contents, clinopyroxene crystals are enriched in Di (diopside) + Hd (hedenbergite) and depleted in CaTs (Ca-Tschermak) + CaTiTs (CaTi-Tschermak) components (Fig. 5b);

6) at low-*T*, low- $H_2O_{initial}$ contents, the amount of Di + Hd in clinopyroxene crystals decreases at the expense of CaTs + CaTiTs (Fig. 5b), responding to the higher degree of melt differentiation;

7) kinetic effects in decompression experiments produce sector-zoned clinopyroxene crystals characterized by Di-Hd-rich, CaTs-CaTiTs-poor hourglass (or basal) sectors {- 1 1 1} and Di-Hd-poor, CaTs-CaTiTs-rich prism sectors {1 0 0};

8) the chemistry of hourglass sectors {- 1 1 1} closely matches with that of experimental crystals obtained at high-*T*, high-$H_2O_{initial}$ contents, as well as with the natural hourglass sectors of phenocrysts from recent eruptions at Mt. Etna volcano;

9) the chemistry of prism sectors {1 0 0} depicts a distinct crystal population, with substantial enrichment in Tschermak components, as also observed for the prism sectors of clinopyroxene phenocrysts from recent eruptions;

10) overall, the development of sector-zoned clinopyroxene crystals from decompression experiments is consistent with kinetic cation partitioning caused by decompression and degassing of Etnean magmas (Ubide and Kamber, 2018; Masotta et al., 2020), in conjunction with charge balance mechanisms due to $Si^{4+} \leftrightarrow Al^{3+}$ substitution in the tetrahedral site and $Mg^{2+} + Fe^{2+} \leftrightarrow Ti^{4+} + Fe^{3+}$ exchange in octahedral sites (Mollo et al., 2018).

4. Discussion

4.1. Clinopyroxene growth rate and thermodynamic constraints

Values of G_{max} for clinopyroxene crystals from this study are listed in Table 1 and plotted in Fig. 6 on a logarithmic scale as a function of the different experimental conditions.

For *Experimental Set ISO* and *Experimental Set ΔP*, the value of G_{max} is positively correlated with temperature and $H_2O_{initial}$, but this correlation is more evident for the decompression experiments rather than isothermal runs where G_{max} values overlap within their uncertainty (Fig. 6a). Major changes of G_{max}

411 are measured as the experimental conditions change in the order of *Experimental Set ISO* (~10^{-15}-10^{-14}
412 mm s^{-1}), *Experimental Set ΔPs* (~10^{-14}-10^{-12} mm s^{-1}), and *Experimental Set ΔPf* (~10^{-10}-10^{-9} mm s^{-1}).

413 Under isothermal conditions, the nucleation of clinopyroxene initiates when the system is heated
414 from the room temperature to the target temperature of the experiment. At nominal $\Delta T = 0$, the degree of
415 melt supersaturation is expected to be close to near-equilibrium crystallization conditions (Baker, 2008).
416 The bulk system tends to minimize the interfacial free energy between small size crystals and the
417 surrounding melt (Bonechi et al., 2020; Masotta et al., 2020), resulting in a closer approach to equilibrium
418 far from dynamic undercooling conditions encountered by magmas rising along the shallower parts of a
419 plumbing system and/or along the volcanic conduit (Mollo and Hammer, 2017 and references therein).
420 Therefore, the rate of attachment/detachment reactions of cations from the melt onto the crystalline
421 surface (and *vice versa*) approaches a steady-state condition in a relatively short experimental time
422 (Kirkpatrick, 1981, 1983; Pontesilli et al., 2019).

423 H_2O exsolution in decompression experiments raises the liquidus region of the melt, thus
424 imposing melt supersaturation (i.e., ΔT = 14-30 °C; Table 1) and facilitating the growth of clinopyroxene
425 (Simakin et al., 2003; Orlando et al., 2008; Hammer, 2008; Mollo and Hammer, 2017). Moreover, Fig.
426 6a shows that the magnitude of G_{max} from H_2O-CO_2-bearing charges (ΔT = 14-18 °C) is systematically
427 lower than that measured for H_2O-bearing charges (ΔT = 16-30 °C), accounting for the presence of CO_2
428 and its rival effect on H_2O contents dissolved in the melt. This observation is consistent with the
429 knowledge that a slow mobility of Si and Al in low-*T*, low-H_2O melts is rate-limiting for divalent Ca and
430 Mg cations, and the addition of tetrahedral groups to the surface of a crystal is the rate-controlling step
431 of the crystal growth (Nascimento et al., 2004).

432 For *Experimental Set CR*, the effect of ΔT (125 °C) on G_{max} corresponds to a large degree of melt
433 supersaturation and the crystal growth regime shifts from interface-controlled to diffusion-controlled
434 (Lofgren, 1974; Sunagawa, 1981; Webb and Dingwell, 1995). Nonetheless, as reported in Pontesilli et
435 al. (2019), relaxation kinetics control the crystal growth as a function of dwell time. G_{max} decreases by
436 orders of magnitude, from ~10^{-11} (*CR-1050-025*) to ~10^{-15} mm s^{-1} (*CR-1050-72*) (Fig. 6b). Short
437 relaxation times of 0.25-1 h favor melt supersaturation and diffusion-limited growth regimes, with more
438 pronounced nucleation of crystals showing disequilibrium textures (Mollo et al., 2010, 2012; Lofgren,
439 1974; Sunagawa, 1981). As the relaxation time increases up to 72 h, an interface-controlled growth
440 promotes formation of euhedral crystals (Fig. 6b). This textual maturation pairs with the progressive
441 decay of G_{max} towards a steady-state condition (Hammer, 2006, 2008; Pontesilli et al., 2019).

Superheating can also fundamentally alter the structure of silicate melts and variable superheating intensity can cause textural differences in subsequently nucleated crystals (First and Hammer, 2016; First et al., 2020). However, it has been also observed that the relaxation of a basaltic melt at 1,300 °C occurs in a very short time (from milli- to micro-seconds) and can be considered independent on the superheating path used in laboratory (Vetere et al., 2013, 2015).

The dependence of crystal growth rate on the degree of undercooling can be calculated as:

$$G \propto \exp\left(\frac{-E}{RT_{exp}}\right)\left[1-\exp\left(\frac{\Delta H\,\Delta T}{R\,T_{exp}\,T_{liquidus}}\right)\right] \quad (6)$$

Eqn. (6) from Armienti (2008) is the rearranged form of equations reported in Cashman (1990) and Toramaru (1991). R is the gas constant (8.310 J mol^{-1} K^{-1}), ΔH is the molar enthalpy of fusion (50-100 kJ mol^{-1}; Weill et al., 1980; Toramaru, 1991), and E is the activation energy of clinopyroxene crystal growth (200-377 kJ mol^{-1}; Toramaru, 1991; Yilmaz et al., 1996; Karamarov et al., 2000; Burkhard, 2005). T_{exp} is the experimental temperature, whereas $T_{liquidus}$ is the liquidus temperature of 1,150-1,220 °C, as determined by rhyolite-MELTS thermodynamic simulations carried out at 300 MPa, 0-5 wt.% H_2O, and NNO+2 buffer (v.1.2.0; Gualda et al., 2012). Within these thermodynamic constraints, the growth rates estimated for clinopyroxene are ~10^{-11}-10^{-9} mm s^{-1} (*Experimental Set ΔPf*), ~10^{-13}-10^{-12} mm s^{-1} (*Experimental Set ΔPs*), and ~10^{-15}-10^{-14} mm s^{-1} (*Experimental Set CR*). Fig. 6a shows that G_{max} values modeled for *Experimental Set ΔP* are comparable with those measured in laboratory, also corroborating the strong control of ΔT on clinopyroxene crystallization. However, for *Experimental Set CR*, the derived thermodynamic quantities match only with G_{max} measured for *CR-1050-24* and *CR-1050-72* experiments (Fig. 6b), whereas Eqn. (6) fails to precinct G_{max} at shorter relaxation times of 0.25, 0.5, 1, and 4 h. From a comparative textural analysis emerges that crystal growth mismatches are caused by nucleation kinetics and abundant dendritic crystallization (Fig. 2). A higher time-averaged nucleation rate over a shorter relaxation time causes a more pronounced melt supersaturation and a diffusion-controlled growth regime (Toramaru, 1991). This agrees 4D crystallization experiments conducted by Arzilli et al. (2019) on a trachybasalt erupted during 2001 eruption at Mt. Etna. It is interesting to note that, in the first part of the experiments, crystallization was induced by decreasing the temperature from superliquidus to subliquidus conditions, with a dwell time at the final temperature of 4 h. During this dwell time, blocky and prismatic clinopyroxene and oxide crystals grew. After 4 h at subliquidus condition, the temperature was further decreased to induce a continuous increase of undercooling. At ΔT

≥ 60 °C, dendritic clinopyroxene crystals developed by diffusion-controlled branching growth in multiple directions to reach a maximum size of 40 μm. Clinopyroxene nucleated heterogeneously on plagioclase and the equilibrium crystal content was achieved in ~3 min (Arzilli et al., 2019). In the present study, however, as the relaxation time increases to 24-72 h, early clinopyroxene dendritic crystals are replaced by euhedral morphologies typical of interface-controlled growth regimes (Supplementary Material 2). The attachment of cations on the crystal surface increases with increasing the relaxation time (Kirkpatrick, 1981, 1983) and euhedral morphologies are more adequately modeled by Eqn. (6) for *CR-1050-24* and *CR-1050-72* experiments (Fig. 6b).

According to clinopyroxene growth kinetics, the transition between interface-controlled and diffusion-controlled regimes is governed by a screw dislocation growth model, where the crystal-melt interface is assumed to be smooth and growth takes place at step sites provided by screw dislocations (Kirkpatrick et al., 1981, 1983). The thermodynamic equations behind screw dislocations are approximated to a temperature-dependent growth rate system (Nascimento et al., 2004):

$$G = f\,\frac{D}{\lambda}\left[1 - \exp\left(-\frac{|\Delta G|}{R\,T}\right)\right], \tag{7}$$

$$f = \frac{\lambda\,\Delta G}{4\,\pi\,\sigma\,V}, \text{ and} \tag{8}$$

$$\sigma = \frac{\alpha\,\Delta H\,\lambda}{V} \tag{9}$$

where D is the diffusion coefficient of slow diffusing Si and Al cations in the melt (~10^{-14}-10^{-15} m^2 s^{-1} at 1,050-1,100 °C; Zhang et al., 2010). λ (2.7 Å) and V (7.59 × 10^{-5} m^3 mol^{-1}) are the diameter of the diffusing building molecules and the molar volume of a pure diopside, respectively (data from Nascimento et al., 2004). ΔG is the Gibbs free energy of clinopyroxene formation estimated by rhyolite-MELTS at the experiment conditions (~7-22 kJ mol^{-1}; Gualda et al., 2012). The parameters f, σ, and α are the fraction of preferred growth sites at the crystal interface, the crystal-melt surface energy, and the reduced surface energy, respectively (cf. Nascimento et al., 2004 and references therein). The crystal growth path modeled through this approach is depicted as green (1,050 °C) and blue (1,100 °C) trends in Fig. 7. In order to isolate the effect of ΔT, the modeled trends are compared with values of G_{max} (green and blue diamonds for 1,050 and 1,100 °C, respectively) from decompression and cooling rate

experiments conducted over similar relaxation times (i.e., on the order of minutes for *ΔPf-1100-2H2O, ΔPf-1100-5H2O, ΔPf-1100-H2O+CO2, ΔPf-1050-2H2O, ΔPf-1050-5H2O, ΔPf-1050-H2O+CO2, CR-1050-0.25, CR-1050-0.5*). Small values of ΔT from *Experimental Set ΔPf* promote an interface-controlled growth (Fig. 7) and the development of large, euhedral sector-zoned crystals characterized by well-formed prismatic morphologies (Figs. 2 and 4, and Supplementary Material 2). The lack of skeletal shapes and formation of sector-zoned clinopyroxene crystals indicate sluggish crystallization kinetics typically observed at $\Delta T \leq 30$ °C (Kouchi et al., 1983; Ubide et al., 2019a; Giuliani et al., 2020; Masotta et al., 2020). Sector-zoned crystals have identical three-dimensional atomic configurations, but the surface of each individual growing sector has a specific two-dimensional atomic arrangement (Dowty, 1976 and references therein). Adjacent crystal regions grow simultaneously and form crystallographically nonequivalent faces with distinctively intersectoral chemical variations, with Di-Hd-rich, CaTs-CaTiTs-poor hourglass sectors {- 1 1 1} and Di-Hd-poor, CaTs-CaTiTs-rich prism sectors {1 0 0} (Fig. 5). These intersectoral differences emerge only under the effect of small ΔT (Kouchi et al., 1983; Masotta et al., 2020), when slow crystal growth kinetics ensure the attainment of clinopyroxene euhedrality (Fig. 4a). As a consequence, the different types of cation substitutions in the sectors reflect the variable spatial structural distributions of M and T sites as a function of the growth velocity of polyhedral sectors (Dowty, 1976 and references therein) rather than the disequilibrium advancement of a skeletal crystal surface via kinetic roughening transition (Sunagawa, 2005).

According to the above criteria, Fig. 7 displays thermodynamic modeling paths that confirm transition between interface-controlled and diffusion-controlled growth at $\Delta T \geq 30$ °C, as texturally constrained by our experimental data set. A diffusion-controlled growth regime develops only when large ΔT from *Experimental Set CR* operate in combination with short relaxation times (Fig. 7). The interface kinetics become extremely fast and tiny, anhedral clinopyroxene crystals develop from supersaturated melt regions where nucleation kinetics strongly prevail over the growth (Figs. 2 and 4b, and Supplementary Material 2). Kinetic effects due to different cation diffusivities in the melt overprint the control exercised by the structural sites of the advancing crystal surface (Giuliani et al., 2020). As a result, there is no evident control of crystal structural sites on cation incorporation and precise chemical correlations amongst the zoning patterns of skeletal clinopyroxene crystals cannot be identified (Kouchi et al., 1983; Masotta et al., 2020).

4.3 Parameterization of clinopyroxene growth kinetics

Growth rates obtained in this study are compared in Fig. 8a with those measured by previous experimental works investigating basaltic and trachybasaltic compositions that reproduce the overall intrinsic variability of rocks from the Monte Maletto Formation (Baker, 2008; Mollo et al., 2013; Pontesilli et al., 2019; Masotta et al., 2020). As pointed out by Bonechi et al. (2020), there is a strong control of melt composition on the crystal growth rate due to polymerization effects caused by an increasing number of tetrahedral sites relative to octahedral sites, thereby increasing the melt viscosity and lowering the diffusivity of elements in the melt. Accounting also for the major effects of T and H_2O on melt viscosity, all the parameterized experiments were performed at conditions analogous to those estimated for magmas erupted at Mt. Etna volcano (i.e., P = 0.1-1,000 MPa, T = 1,050-1,150 °C, H_2O = 0-4 wt.%, fO_2 = NNO+1.5-NNO+2, ΔT = 75-233 °C, and CR = 0.001-100 °C s^{-1}; see the review study of Mollo et al., 2018 and references therein). Fig. 8a shows that G_{max} decreases by approximately six orders of magnitude, from ~10^{-9} to ~10^{-15} mm s^{-1}, as the relaxation time increases from 0.08 to 72 h (Fig. 8a). Statistical calculations were carried out on the experimental data set with the Statgraphics Centurion 18® algorithm (Statpoint Technologies, Inc., Warrenton, VA, USA) by running a weighted least square (WLS) regression analysis. While in ordinary least square (OLS) regressions the standard deviation (σ) of error is assumed constant over all values of the explanatory variable, in WLS regressions the efficiency of estimation is maximized by giving to each data its proper amount of influence (i.e., weight w) over the estimate. This is especially important in modeling of logarithmic data sets that are susceptible to uncertainties associated with the linearization of the model (i.e., heteroskedasticity; Hair et al., 1995). On this basis, error minimization is attained by 1) incorporating weights into the fitting criterion and 2) performing Monte Carlo propagation of errors (Ratkowsky, 1990). The general form of WLS model is written in matrix notation as:

$$\mathbf{Y} = \mathbf{X\beta} + \boldsymbol{\varepsilon} \quad (10)$$

where $\mathbf{Y}$ = ($n \times 1$) vector of y observations, $\mathbf{X}$ = ($n \times k$) matrix of x variables, and $\boldsymbol{\beta}$ = ($k \times 1$) vector of β regression coefficients. The $\boldsymbol{\varepsilon}$ = ($n \times 1$) vector of random errors ε is expressed as ($\mathbf{0}$, $\boldsymbol{\sigma^2 W}$). In OLS, ε has mean equals to zero and variance close to the square of the standard deviation [$var(\varepsilon) = \sigma^2$]. Conversely, in WLS, ε does not have constant variance [$var(\varepsilon) = \sigma^2/w$] and the weight given to each observation is inversely proportional to the variance of the explanatory variable. $\mathbf{W}$ represents an ($n \times n$) diagonal matrix with diagonal entries corresponding to weights and $\mathbf{Var(\varepsilon)} = \mathbf{W^{-1}\sigma^2}$. The solution of Eqn. (10) is:

$$\boldsymbol{\beta}^{*} = \frac{\mathbf{X^T W Y}^{*}}{\mathbf{X^T W X}} \quad (11)$$

where **β*** and **Y*** are estimates of **β** and **Y**, respectively, and $\mathbf{X^T}$ is the transpose of matrix **X**. WLS regression of experimental data displayed in Fig. 8a have the following form:

$$\ln G_{max} = \beta_0 + \beta_1 \ln t_{max} \quad (12)$$

The best predicting model for G_{max} has been calculated by optimizing the weighted fitting criterion and estimating the variance of the data set for each fixed covariate vector in Eqn. (11). This statistical approach allows to downweight outliers and reduce their impact on the overall model. The least square minimization of Eqn. (12) yields β_0 = -5.512 (±0.041 $\sigma_{\beta 0}$) and β_1 = -0.778 (±0.012 $\sigma_{\beta 1}$). The coefficient of determination (R^2), standard error of estimate (SEE_{Gmax}), and mean absolute error (ε) are 0.977, 0.242, and 0.181, respectively. As a further error test, the regression constants β_0 and β_1 have been also recalculated by perturbing Eqn. (12) via Monte Carlo simulations over a normal distribution with the mean centered on the original value of G_{max} and with deviation close to SEE_{Gmax} (Hair et al., 1995). After generating 1,000 sets of hypothetical regression coefficients, results from probability density functions confirm data from least square minimization. Therefore, it is calculated that ~68% of β_0 (Fig. 8b) and β_1 (Fig. 8c) have uncertainties of ±0.039 $\sigma_{\beta 0}$ and ±0.011 $\sigma_{\beta 1}$, respectively. Since most of the calibration data were obtained at 0 and 2 wt.% H_2O contents in both the present study and previous works, WLS regressions have been replicated on two distinct data sets for anhydrous (0 wt.% H_2O) and hydrous (2 wt.% H_2O) experiments. These calculations yield very similar regression coefficients ($^{anhydrous}\beta_0$ = -5.589 vs. $^{hydrous}\beta_0$ = -5.521, as well as $^{anhydrous}\beta_1$ = -0.771 vs. $^{hydrous}\beta_0$ = -0.778) and errors of estimate ($^{anhydrous}SEE_{Gmax}$ = 0.251 vs. $^{hydrous}SEE_{Gmax}$ = 0.244). Attainment of comparable regression coefficients points out that an increase in H_2O of 5 wt.% or an increase in temperature of 50 °C produce a similar magnitude of increase in G_{max} (Fig. 6a) and similar clinopyroxene contents (Fig. 3a). For example, at constant T, G_{max} increases by 20% as the melt-H_2O content increases from 0 to 5 wt.%. Analogously, at constant H_2O concentration, G_{max} increases by 18% as T increases from 1,050 to 1,100 °C. As previously observed by Pontesilli et al. (2019), the magnitude of G_{max} is mostly dictated by the duration of crystal growth (Fig. 6b), in concert with the increase in crystal size (L_{max}) and the clinopyroxene euhedrality (S_v^P).

Recalling the crystal size distribution (CSD) theory and Eqn. (5), the crystal nucleation rate is related to the growth rate as $J = N_0 \times G$. By assuming $G = G_{max}$ and $\tau = t_{max}$, we can substitute Eqn. (12) into the slope $m = 1 / (G \times \tau)$ of Eqn. (5) and then rearrange this algebraic expression to isolate the crystallization time of clinopyroxene forming under naturally undercooling conditions:

$$G_{\max} = {t_{max}}^{\beta_1} \exp\beta_0, \quad (13)$$

$$m = -\frac{1}{\left|{t_{max}}^{(\beta_1+1)} \exp\beta_0\right|}, \text{ and} \quad (14)$$

$$t_{max} = \left(-\frac{1}{m \exp\beta_0}\right)^{\left(\frac{1}{\beta_1+1}\right)} \quad (15)$$

The overall uncertainty associated with the estimate of t_{max} has been determined by propagating into Eqn. (15) the values of SEE_{Gmax}, $\sigma_{\beta 0}$, and $\sigma_{\beta 1}$ via Monte Carlo simulations. Density estimations indicate that the uncertainty of t_{max} varies from 22% to 28%, with an average close to 26% (Fig. 8d). The calculation of t_{max} can be performed through the Microsoft Excel spreadsheet available online as Supplementary Material 5.

4.4. Application to magma dynamics at Mt. Etna volcano

Mt. Etna is one of the most studied and monitored volcanoes in the world. The persistent eruptive activity of Mt. Etna threatens the populations living in its shadow, also causing regional climate changes in Sicily and the temporary closure of the Fontanarossa International airport of Catania. The plumbing system is governed by frequent input and mixing of primitive, volatile-rich magmas rising from a deeper (~10 km) storage region into shallower reservoirs (3-5 km) and, occasionally, ponding within the volcanic edifice (0.5-2.5 km; Patanè et al., 2003; Corsaro et al., 2009; Ubide and Kamber, 2018; Mollo et al., 2018). Abundant volatile exsolution and degassing are the key mechanisms controlling mineral and melt compositions, degree of crystallization, magma ascent velocity, and eruptive style (Armienti et al., 2007; Lanzafame et al., 2013). Magma can be erupted either quickly through deep dykes feeding eccentric eruptions (i.e., bypassing the central conduits) or gradually through the central conduits feeding shallow reservoirs (Ubide and Kamber, 2018).

A cyclic fountaining activity occurred at the New Southeast Crater (NSEC) in 2011–2012 and 2013, including normal paroxysmal sequences and energetic episodes with high eruption columns (7–8 km above the vent). A detailed multi-disciplinary data set referring to these eruptions can be found in literature, including mineral and melt compositions, volcanological constraints, thermal mapping, and structural surveys (Andronico et al., 2005; Ferlito et al., 2009, 2012; Mollo et al., 2015b, 2018; Perinelli et al., 2016; Giuffrida and Viccaro, 2017; Giuffrida et al., 2018; Giacomoni et al., 2018). In this study, we focus on clinopyroxene microphenocrysts and microlites from fourteen 2011-2012 scoria clasts that are representative of 12/01/2011, 18/02/2011, 10/04/2011, 12/05/2011, 30/07/2011, 20/08/2011, 29/08/2011, 08/09/2011, 15/11/2011, 05/01/2012, 04/03/2012, 18/03/2012, 01/04/2012, and 24/04/2012 lava fountains (Supplementary Material 3). These samples have variable vesicularity (15-30%) and porphyritic index (30-60%), but a uniform phase assemblage of olivine + clinopyroxene + plagioclase + titanomagnetite + glass (see Supplementary Material 3 and Giacomoni et al., 2018 for a detailed petrographic description). By analyzing cation redistributions in 2011-2012 clinopyroxene and titanomagnetite crystals, Mollo et al. (2015b) documented the ability of microphenocrysts and microlites to record variable undercooling histories between the sub-liquidus temperature of the magmatic reservoir and the closure temperature of crystal growth, when the kinetics and energetics of solidification were rapidly frozen-in at the time of eruption.

The saturation conditions of clinopyroxene crystals from 2011-2012 lava fountains, prior to dynamic ascent of magma towards the surface, have been estimated in this study through the integrated *P*-*T*-H_2O model of Mollo et al. (2018) specifically designed to Etnean minerals and their host magmas (Supplementary Material 4). The model uncertainty is minimized by adjusting the *P*-*T*-H_2O estimates within the calibration errors of the barometer (±150 MPa), thermometer (±20 °C), and hygrometer (±0.45 wt.% H_2O), in order to reduce the difference (Δ) between measured and predicted equilibrium values of $Kd_{Fe\text{-}Mg}$ (Fe-Mg exchange partition coefficient; Putirka, 2008), K_{Na} (Na partition coefficient; Blundy et al., 1995), and *DiHd* (diopside + hedenbergite; Mollo et al., 2013). These correction criteria and probability density functions are applied to microphenocryst and bulk rock compositions (Supplementary Material 4), providing the most reliable near-equilibrium conditions for clinopyroxene saturation at ~210-260 MPa (i.e., ~8-10 km, presuming a continental crust density of 2.6 g cm^{-3}; Armienti et al., 2013), ~1,070-1,080 °C, and ~2.2-2.4 wt.% H_2O (Fig. 9). Notably, the estimated pressure range matches with magma storage at an intermediate depth of 7-13 km (Murru et al., 1999) and within a major aseismic high P-wave velocity body extending down to 18 km (Aloisi et al., 2002).

Fig. 10 shows CSD curves of 2011-2012 clinopyroxene crystals, with kinked concave-up shapes and marked changes in slope, from a shallower gradient in the larger crystals to a steeper gradient in the smaller ones (Burney et al., 2020). Regression coefficients determined for microphenocrysts (m from -13.589 to -16.914 mm^{-1} and N_0 from 8.177 to 10.358 mm^{-4}) and microlites (m from -45.981 to -93.140 mm^{-1} and N_0 from 13.796 to 16.764 mm^{-4}) are characteristically different (Table 2). Coherently, the systematic kink of CSD curves attests the occurrence of distinct crystal size distributions for microphenocrysts ($L \geq 0.1$ mm) and microlites ($L < 0.1$ mm). In a few samples the kink shifts at 0.14 mm because of the higher crystallinity of the erupted products (Cashman and Marsh 1988; Higgins 1996). These kinked shape trends are generally attributed to variable crystal growth rates and undercooling histories of magmas during ascent along different portions of the plumbing system and volcanic conduit, without any gain or loss from/to external magma batches (Kirkpatrick, 1981, 1983; Maaloe et al., 1989; Armienti et al., 1994; Armienti, 2008). In this context, $N(L)$ vs. L trajectories displayed in Fig. 10 and their regression coefficients (Table 2) are principally the result of different crystallization regime upon the P-T-H_2O array experienced by dynamically erupted magmas (Armienti et al., 2013).

By applying Eqn. (15) to the slope of each CSD curve, we have quantified the growth time recorded by the textual evolution of 2011-2012 clinopyroxene crystals. Results from calculations are listed in Table 2 and return values of t_{max} ranging from ~1.4±0.3 to ~33.4±8 min and from ~50.7±13 to ~136.2±35 h for microlite and microphenocryst populations, respectively. The low magnitude of t_{max} measured for microlites testifies to fast kinetic effects and rapid crystal growth regimes, when magma acceleration within the uppermost part of the conduit leads to large ΔT (Armienti, 2008). According to this proposition, fluid mechanic mechanisms governing magma ascent indicate that, upon abundant volatile exsolution within a narrow degassing path, the volume expansion of magma by the growth of gas bubbles is balanced by an increasing acceleration towards the surface (Gonnermann and Manga, 2013). Conversely, the high magnitude of t_{max} derived for microphenocrysts indicates sluggish kinetic effects associated with small ΔT and slow crystal growth regimes from more relaxed melts. Evidently, at greater depths and within the plumbing system of Mt. Etna volcano, clinopyroxene microphenocrysts have more time to grow and equilibrate with the melt under steady-state conditions (Armienti et al., 2013).

We emphasize that values of t_{max} are intrinsically related to the kinetic aspects and thermodynamics of clinopyroxene growth. Therefore, caution should be exercised in comparing the magnitude of t_{max} with the time scale of magma dynamics derived by numerical modeling of volcanic conduit processes (e.g., La Spina et al., 2016, 2021; Polacci et al., 2019) and/or time scales from

elemental diffusion (e.g., Giuffrida et al., 2018; Ubide and Kamber, 2018). The corollary is that the crystal growth will never occur when a full thermodynamic equilibrium (i.e., a minimum energy state) is achieved throughout the crystal-melt interface. There is an energy barrier to overcome in order to promote imbalance between the attachment and detachment energies of cations at the crystal-melt interface. This excess energy is attained by melt supersaturation, when the thermodynamic driving force is higher than a critical threshold above which crystal growth takes place (Sunagawa, 2005). At large ΔT, such as those typically occurring during rapid ascent of magma within a volcanic conduit, the effective mechanism controlling clinopyroxene growth rate depends on the slow diffusivity of Si and Al in the melt with respect to Ca and Mg. The addition of network-former species to the growing surface of crystals is the rate-controlling step for the textural maturation of clinopyroxene (Mollo and Hammer, 2017). Moreover, since the strength of the ^{T}Al–O bonds in the melt is weaker than that of ^{T}Si–O bonds (Kirkpatrick, 1983), the transfer rate of incompatible cations (i.e., Al + Ti) from the melt to the crystal surface is much more facilitated than that of compatible elements (i.e., Ca + Mg; Mollo et al., 2010, 2012(a o b); Pontesilli et al., 2019; Masotta et al., 2020). According to these kinetic principles, G_{max} and t_{max} are inextricably interrelated to the morphological stability of the crystal-melt interface throughout the growth process (Sunagawa, 2005). The crystal-melt interface is the locus where growth or dissolution take place upon dynamic changes of P-T-H_2O during magma ascent towards the surface and upon decompression-cooling paths. Melt supersaturation causes morphological instability of the crystal and shifts from polyhedral to hopper to dendritic forms, by imposing temperature and concentration gradients at the interface (Sunagawa, 2005).

According to the above considerations, the magnitude of G_{max} and t_{max} mostly depends on 1) morphological instability as a function of attachment/detachment energies of cations with increasing ΔT and 2) concentration gradients in the melt next to the advancing crystal surface and disequilibrium uptake of incompatible cations within the lattice site (Pontesilli et al., 2019; Masotta et al., 2020). However, it is interesting to note that values of t_{max} (~1-41 min; Table 2) measured for 2011-2012 clinopyroxene microlites are consistent with the numerical analysis of magma ascent times of 1995–2019 eruptions at Mt. Etna (Polacci et al., 2019). The 1995–2019 explosive activity produced, among other products, significant ash emissions. The numerical analysis was performed by considering volcanic conduits with either cylindrical or dyke geometries, yielding ascent time minimum (~2.5 min) at the center of the conduit and maximum (~25 min) at the conduit walls, corresponding to ~1% of the total magma rising within the conduit (Polacci et al., 2019). Similarly, the estimated ascent time of magma within a dyke ranges from ~3.3 min to ~33 min, corresponding to less than 0.4% of the total magma (Polacci et al.,

2019). According to La Spina et al. (2021), lava fountaining at Mt. Etna consists of an eruptive style distinct from effusive and explosive eruptions, as the result of rapid magma ascent with most of fragmentation above the vent rather than within the conduit. Magma ascent times of ~40 min determined by La Spina et al. (2021) are in the same order of magnitude of t_{max} calculated for some 2011-2012 microlites and microphenocrysts from this study.

A conceptual model of open conduit dynamics at Mt. Etna is schematized in Fig. 11. Most of the clinopyroxene microlite crystallization occurs within the uppermost segment of the volcanic conduit under the effect of large ΔT and short t_{max} (Fig. 11). This short time is also comparable with that (< 60 min) estimated for plagioclase during dynamic ascent of magma and under strong disequilibrium conditions driven by abundant volatile exsolution (La Spina et al., 2016). *In-situ* experiments carried out on a typical Etnean trachybasalt reveal that ΔT = 60-140 °C drive exceptionally rapid crystallization of plagioclase and clinopyroxene microlites in several minutes, also inducing a step change in viscosity that may trigger magma fragmentation (Arzilli et al., 2019). Moreover, because of rapid fractionation of lithium between melt and fluid during magma degassing, the decrease in Li concentration in plagioclase by diffusion corresponds to magma ascent time scales variable from 0.2 to 3 min for paroxysmal sequences (Giuffrida et al., 2018). This syn-eruptive stage of magma is outlined by t_{max} of ~1-3 min calculated for 2011-2012 clinopyroxene microlites (Fig. 11), as well as by rapid decompression (12 MPa min^{-1}) and cooling experiments (12 °C min^{-1}) of Arzilli et al. (2019) showing that abundant clinopyroxene microlite crystallization occurs in only 5 min at ΔT > 100 °C. Considering that most of the disequilibrium crystallization takes place at ~1.5 km below the vent (cf. La Spina et al., 2016, 2021), we derive maximum magma ascent rates of ~1-23 m s^{-1} considering the model error (Table 2 and Fig. 11). These estimates are statistically comparable with syn-eruptive ascent rates of ~3 m s^{-1} determined for mild lava fountaining activity at Mt. Etna, Stromboli, and Kilauea (La Spina et al., 2016, 2021), as well as for syn-eruptive ascent rates measured for shallow subvolcanic magma storage zones (depth ≤10 km) feeding more silicic explosive eruptions worldwide (~0.5-50 m s^{-1}; Cassidy et al., 2018).

Notably, the compositional difference between the initial melt and the final three-dimensional structural arrangement of the crystal requires that stable nuclei can form only when the local configuration of molecular units attains a critical cluster radius (e.g., Vetere et al., 2015 and references therein). As the microlite crystallization increases during ascent of magma within the conduit, the residual melt composition becomes progressively more differentiated (i.e., SiO_2-Na_2O-rich and CaO-MgO-poor) favoring the enlargement of plagioclase stability field (i.e., albite end-member) at the expense of clinopyroxene (i.e., diopside end-member). For this reason, at ΔT > 100 °C, the growth

752 kinetics of 2011-2012 clinopyroxene microlites does not return magma ascent rates > 23 m s^{-1} (Fig. 11),
753 such as those also measured at Mt. Etna that are related to strong degassing processes governing Li
754 diffusion in plagioclase (~43 m s^{-1}; Giuffrida et al., 2018) and further magma acceleration at the vent
755 (~75 m s^{-1}; La Spina et al., 2021).

756 Differently from shallow conduit and vent dynamics, values of t_{max} (~38-171 h; Table 2)
757 calculated for 2011-2012 clinopyroxene microphenocrysts are orders of magnitude greater than the very
758 fast crystallization history recorded by microlites. Evidently, the growth of microphenocrysts does not
759 represent the timing of eruption within the upper conduit or immediately before ejection from the vent,
760 where large degrees of supersaturation are driven by fast cooling, decompression, and degassing of
761 magma (Fig. 11). Rather, most of microphenocryst growth is governed by a small ΔT and long t_{max} at
762 depth (Fig. 11), where crystallization kinetics are slow and the crystal surface has enough time to develop
763 polyhedral morphology (Armienti et al., 2013). Moreover, there is no systematic change of t_{max} with the
764 1) 2011-2012 paroxysmal phase duration, 2) Strombolian activity preceding lava fountaining, and 3)
765 associated seismic signals or volcanic tremors (data from the multidisciplinary reports of the INGV
766 Osservatorio Etneo available at www.ct.ingv.it). This suggests that the onset of microphenocryst growth
767 takes place at the early saturation condition of clinopyroxene and under a near-equilibrium crystallization
768 state corresponding to the main storage region of magma at ~8-10 km of depth. It is also not excluded
769 that microphenocryst crystallization continues via open system processes governed by the invasion of
770 the plumbing system with fresh magma (Fig. 11). Time scales from this study closely match with those
771 (~17-168 h) derived by Ubide and Kamber (2018) for the development of Cr zoning in clinopyroxene
772 caused by continuous magma recharge and mixing events at depth of ~10 km (Fig. 11). Under such
773 conditions, both volatile exsolution and crystallization are low, bubble expansion and magma buoyancy
774 are limited, and the slow upward migration of magma provides more time for mineral-melt-fluid
775 equilibration (e.g., Cassidy et al., 2018). Ubide and Kamber (2018) estimated magma ascent rates of
776 0.02-0.17 m s^{-1} that are analogous to those (0.02-0.07 m s^{-1}; Table 2) determined for the growth of 2011-
777 2012 clinopyroxene microphenocrysts. Therefore, differently from the fast acceleration of magma within
778 the conduit, open system dynamics at depth require longer time periods for the migration of magma
779 through interconnected storage regions (Fig. 11). This conclusion is supported by similar estimates
780 obtained through different methodologies based on cation redistributions in minerals (0.01-0.31 m s^{-1};
781 Mollo et al., 2015b) and geophysical signals (0.04-0.4 m s^{-1}; Aloisi et al., 2006) at Mt. Etna volcano, as
782 well as by authors investigating other volcanic settings worldwide, such as Hawaii (0.01–0.04 m s^{-1};

783 Rutherford, 2008; Gonnermann and Manga, 2013), Unzen (0.01–0.07 m s^{-1}; Toramaru et al., 2008) and
784 Mount St. Helens (0.01–0.15 m s^{-1}; Rutherford and Hill, 1993).
785
786 **5. Conclusions**
787 Clinopyroxene growth kinetics have been experimentally investigated and parameterized under a
788 broad range of isothermal-isobaric, decompression, and cooling rate conditions, representative of
789 variable crystallization conditions at Mt. Etna volcano. Through this approach, the following main
790 conclusions can be drawn:
791 1) the texture of clinopyroxene is greatly controlled by melt supersaturation (i.e., undercooling) and
792 relaxation time resulting from *P*-*T*-H_2O changes;
793 2) crystal euhedrality is maintained either under substantially subliquidus isothermal-isobaric or
794 slow-to-fast decompression conditions, with the main difference represented by the development
795 of sector-zoned clinopyroxene crystals during melt decompression;
796 3) as the relaxation time increases, the crystal growth rate radically decreases, whereas the crystal
797 euhedrality increases;
798 4) thermodynamic modeling suggests that the transition between interface-controlled and diffusion-
799 controlled growth arises at undercooling higher than 30 °C;
800 5) below this threshold value, sluggish crystallization kinetics lead to the formation of sector-zoned
801 clinopyroxene crystals, with Di-Hd-rich, CaTs-CaTiTs-poor hourglass sectors {- 1 1 1} and Di-
802 Hd-poor, CaTs-CaTiTs-rich prism sectors {1 0 0} typically observed at Mt. Etna volcano;
803 6) by integrating experimental textural data and the algebraic expression of crystal size distribution
804 (CSD), the crystallization time of clinopyroxene can be parameterized as a function of growth
805 rate;
806 7) for the case of 2011-2012 lava fountains, results from calculations return time scales variable
807 from ~10^0-10^1 min and ~10^1-10^2 h for microlite and microphenocryst populations, respectively;
808 8) while shorter time scales of microlites testify to fast kinetic effects due to large undercoolings
809 during magma acceleration in the uppermost part of the volcanic conduit, longer time scales of
810 microphenocrysts are associated with near-equilibrium crystallization due to small undercoolings
811 at depth;
812 9) we conclude that fast ascent rates of magmas (~10^0-10^1 m s^{-1}) lead to disequilibrium growth of
813 microlites and supersaturation (i.e., undercooling) effects due to strong degassing and cooling
814 before eruption from the vent. In contrast, slow ascent rates of magmas (~10^{-2} m s^{-1}) favor near-

equilibrium crystallization of microphenocrysts over longer time periods and within the interconnected storage regions that characterize the plumbing system architecture of Mt. Etna volcano.

Acknowledgments

The authors would like to thank Alessandro Vona and Alessio Pontesilli for their kind help with crystal size distribution (CSD) analysis. This work has been greatly improved by the helpful and thoughtful reviews of Fabio Arzilli and Emily First. Michael Roden is also acknowledged for his valuable editorial guidance.

References

Aloisi, M., Cocina, O., Neri, G., Orecchio, B., Privitera, E., 2002. Seismic tomography of the crust underneath the Etna volcano, Sicily. Phys. Earth Planet. Inter. 134, 139–155.

Aloisi, M., Bonaccorso, A., Gambino, S., 2006. Imaging composite dike propagation (Etna, 2002 case). J. Geophys. Res. 111.

Andronico, D., Branca, S., Calvari, S., Burton, M., Caltabiano, T., Corsaro, R.A., Del Carlo, P., Garfì, G., Lodato, L., Miraglia, L., Murè, F., Neri, M., Pecora, E., Pompilio, M., Salerno, G., Spampinato, L., 2005. A multi-disciplinary study of the 2002-03 Etna eruption: insights into a complex plumbing system. Bull Volcanol 67, 314–330.

Armienti, P., Pareschi, M.T., Innocenti, F., Pompilio, M., 1994. Effects of magma storage and ascent on the kinetics of crystal growth. Contr. Mineral. and Petrol. 115, 402–414.

Armienti, P., Francalanci, L., Landi, P., 2007. Textural effects of steady state behaviour of the Stromboli feeding system. J. Volcanol. Geotherm. Res. 160, 86–98.

Armienti, P., 2008. Decryption of Igneous Rock Textures: Crystal Size Distribution Tools. Rev Mineral Geochem 69, 623–649.

Armienti, P., Perinelli, C., Putirka, K.D., 2013. A New Model to Estimate Deep-level Magma Ascent Rates, with Applications to Mt. Etna (Sicily, Italy). J. Petrol. 54, 795–813.

Arzilli, F., Fabbrizio, A., Schmidt, M.W., Petrelli, M., Maimaiti, M., Dingwell, D.B., Paris, E., Burton, M., Carroll, M.R., 2018. The effect of diffusive re-equilibration time on trace element partitioning between alkali feldspar and trachytic melts. Chem. Geol. 495, 50–66.

Arzilli, F., La Spina, G., Burton, M.R., Polacci, M., Le Gall, N., Hartley, M.E., Di Genova, D., Cai, B., Vo, N.T., Bamber, E.C., Nonni, S., Atwood, R., Llewellin, E.W., Brooker, R.A., Mader, H.M., Lee,

P.D., 2019. Magma fragmentation in highly explosive basaltic eruptions induced by rapid crystallization. Nat. Geosci. 12, 1023–1028.

Baker, D.R., 2008. The fidelity of melt inclusions as records of melt composition. Contrib Mineral Petrol 156, 377–395.

Blundy, J.D., Falloon, T.J., Wood, B.J., Dalton, J.A., 1995. Sodium partitioning between clinopyroxene and silicate melts. J. Geophys. Res. Solid Earth 100, 15501–15515.

Bonechi, B., Perinelli, C., Gaeta, M. Clinopyroxene growth rates at high pressure: constraints on magma recharge of the deep reservoir of the Campi Flegrei Volcanic District (south Italy). Bull Volcanol 82, 5.

Botcharnikov, R.E., Almeev, R.R., Koepke, J., Holtz, F., 2008. Phase Relations and Liquid Lines of Descent in Hydrous Ferrobasalt--Implications for the Skaergaard Intrusion and Columbia River Flood Basalts. J. Petrol. 49, 1687–1727.

Burkhard, D.J.M., 2005. Nucleation and growth rates of pyroxene, plagioclase, and Fe-Ti oxides in basalt under atmospheric conditions. European Journal of Mineralogy 17, 675–686.

Burney, D., Peate, D.W., Riishuus, M.S., Ukstins, I.A., 2020. Reconstructing the plumbing system of an off-rift primitive alkaline tuya (Vatnafell, Iceland) using geothermobarometry and CSDs. J. Volcanol. Geotherm. Res. 399, 106914.

Cashman, K.V., Marsh, B.D., 1988. Crystal size distribution (CSD) in rocks and the kinetics and dynamics of crystallization II: Makaopuhi lava lake. Contr. Mineral. and Petrol. 99, 292–305.

Cashman, K.V., 1990. Textural constraints on the kinetics of crystallization of igneous rocks. Rev. Mineral. 24, 259–314.

Cassidy, M., Manga, M., Cashman, K., Bachmann, O., 2018. Controls on explosive-effusive volcanic eruption styles. Nat Commun 9.

Corsaro, R.A., Civetta, L., Di Renzo, V., Miraglia, L., 2009. Petrology of lavas from the 2004-2005 flank eruption of Mt. Etna, Italy: inferences on the dynamics of magma in the shallow plumbing system. Bull. Volcanol. 71, 781–793.

Di Stefano, F., Mollo, S., Ubide, T., Petrone, C.M., Caulfield, J., Scarlato, P., Nazzari, M., Andronico, D., Del Bello, E., 2020. Mush cannibalism and disruption recorded by clinopyroxene phenocrysts at Stromboli volcano: New insights from recent 2003–2017 activity. Lithos 360–361, 105440.

Dowty, E., 1976. Crystal structure and crystal growth: II. Sector zoning in minerals. Am. Mineral. 61, 460–469.

879 Duan, X., 2014. A general model for predicting the solubility behavior of H2O-CO2 fluids in silicate
880 melts over a wide range of pressure, temperature and compositions. Geochim. Cosmochim. Acta 125,
881 582–609. http://dx.doi.org/10.1016/j.gca.2013.10.018.
882 Ferlito, C., Coltorti, M., Cristofolini, R., Giacomoni, P.P., 2009. The contemporaneous emission of
883 low-K and high-K trachybasalts and the role of the NE Rift during the 2002 eruptive event, Mt. Etna,
884 Italy. Bull Volcanol 71, 575–587.
885 Ferlito, C., Viccaro, M., Nicotra, E., Cristofolini, R., 2012. Regimes of magma recharge and their
886 control on the eruptive behaviour during the period 2001–2005 at Mt. Etna volcano. Bull Volcanol 74,
887 533–543.
888 First, E.C., Leonhardi, T.C., Hammer, J.E., 2020. Effects of superheating magnitude on olivine
889 growth. Contrib Mineral Petrol 175, 13.
890 First E.C., Hammer J.E., 2016. Igneous cooling history of olivine-phyric shergottite Yamato 980459
891 constrained by dynamic crystallization experiments. Meteorit Planet Sci. 51, 1233–1255.
892 Giacomoni, P.P., Coltorti, M., Mollo, S., Ferlito, C., Braiato, M., Scarlato, P., 2018. The 2011–2012
893 paroxysmal eruptions at Mt. Etna volcano: Insights on the vertically zoned plumbing system. J. Volcanol.
894 Geotherm. Res. 349, 370–391.
895 Giordano, D., Nichols, A.R.L., Dingwell, D.B., 2005. Glass transition temperatures of natural
896 hydrous melts: a relationship with shear viscosity and implications for the welding process. J. Volcanol.
897 Geotherm. Res. 142, 105–118.
898 Giuffrida, M., Viccaro, M., 2017. Three years (2011–2013) of eruptive activity at Mt. Etna: Working
899 modes and timescales of the modern volcano plumbing system from micro-analytical studies of crystals.
900 Earth Sci Rev 171, 289–322.
901 Giuffrida, M., Viccaro, M., Ottolini, L., 2018. Ultrafast syn-eruptive degassing and ascent trigger
902 high-energy basic eruptions. Sci Rep 8.
903 Giuliani, L., Iezzi, G., Vetere, F., Behrens, H., Mollo, S., Cauti, F., Ventura, G., Scarlato, P., 2020.
904 Evolution of textures, crystal size distributions and growth rates of plagioclase, clinopyroxene and spinel
905 crystallized at variable cooling rates from a mid-ocean ridge basaltic melt. Earth Sci Rev 204, 103165.
906 Gonnermann, H.M., Manga, M., 2013. Dynamics of magma ascent in the volcanic conduit. In:
907 Fagents, S.A., Gregg, T.K.P., Lopes, R.M.C. (Eds.), Modeling Volcanic Processes. Cambridge Univ
908 Press, pp.55–84.
909 Gualda, G.A., Ghiorso, M.S., Lemons, R.V., Carley, T. L., 2012. Rhyolite-MELTS: a modified
910 calibration of MELTS optimized for silica-rich, fluid-bearing magmatic systems. J. Petrol. 53, 875–890.

Hammer, J.E., 2008. Experimental Studies of the Kinetics and Energetics of Magma Crystallization. Rev Mineral Geochem 69, 9–59.

Hammer, J.E., 2006. Influence of fO2 and cooling rate on the kinetics and energetics of Fe-rich basalt crystallization. Earth Planet. Sci. Lett. 248, 618–637.

Hammer, J., Jacob, S., Welsch, B., Hellebrand, E., Sinton, J., 2016. Clinopyroxene in postshield Haleakala ankaramite: 1. Efficacy of thermobarometry. Contrib Mineral Petrol 171.

Hair Jr., J.F., Anderson, R.E., Tatham, R.L., Black, W.C., 1995. Multivariate Data Analysis. 3rd ed. Macmillan, New York (742 pp.).

Higgins, M.D., 1996. Magma dynamics beneath Kameni volcano, Thera, Greece, as revealed by crystal size and shape measurements. J. Volcanol. Geotherm. Res. 70, 37–48.

Higgins, M.D., 2000. Measurement of crystal size distributions. Am. Mineral. 85, 1105–1116.

Iezzi, G., Mollo, S., Shaini, E., Cavallo, A., Scarlato, P., 2014. The cooling kinetics of plagioclase revealed by electron microprobe mapping. Am. Mineral. 99, 898–907.

Ishibashi, H., 2013. Spinel–melt oxygen barometry: a method and application to Cenozoic alkali basaltic magmas from the Higashi–Matsuura district, NW Kyushu, Japan. Geosci. Repts. 40, 21–32.

Karamanov, A., Pisciella, P., Pelino, M., 2000a. The crystallisation kinetics of iron rich glass in different atmospheres. J. Eur. Ceram. Soc. 20, 2233–2237.

Kirkpatrick, R.J., 1981. Kinetics of crystallization of igneous rocks. In: Lasaga, A.C., Kirkpatrick, R.J. (Eds.), Reviews in Mineralogy 8. pp. 321–395.

Kirkpatrick, R.J., 1983. Theory of nucleation in silicate melts. Am. Mineral. 68, 66–77.

Kostov, I., Kostov, R.I., 1999. Crystal Habits of Minerals. Bulgarian Academic Monographs, Sophia.

Kouchi, A., Sugawara, Y., Kashima, K., Sunagawa, I., 1983. Laboratory growth of sector zoned clinopyroxenes in the system CaMgSi2O6-CaTiAl2O6. Contrib. Mineral. Petrol. 83, 177–184.

Lanzafame, G., Mollo, S., Iezzi, G., Ferlito, C., Ventura, G., 2013. Unraveling the solidification path of a pahoehoe “cicirara” lava from Mount Etna volcano. Bull Volcanol 75.

La Spina, G., Burton, M., de’ Michieli Vitturi, M., Arzilli, F., 2016. Role of syn-eruptive plagioclase disequilibrium crystallization in basaltic magma ascent dynamics. Nat Commun 7.

La Spina, G., Arzilli, F., Llewellin, E.W., Burton, M.R., Clarke, A.B., de’ Michieli Vitturi, M., Polacci, M., Hartley, M.E., Di Genova, D., Mader, H.M., 2021. Explosivity of basaltic lava fountains is controlled by magma rheology, ascent rate and outgassing. Earth Planet. Sci. Lett. 553, 116658.

Lasaga, A.C., 1998. Kinetic Theory in the Earth Sciences. Princeton University Press, Princeton, New York.

Lofgren, G.E., 1974. An experimental study of plagioclase morphology: isothermal crystallization. Am. J. Sci. 264, 243–273.

Maaløe, S., Tumyr, O., James, D., 1989. Population density and zoning of olivine phenocrysts in tholeiites from Kauai, Hawaii. Contr. Mineral. and Petrol. 101, 176–186.

Marsh, B.D., 1988. Crystal size distribution (CSD) in rocks and the kinetics and dynamics of crystallization. Contr. Mineral. and Petrol. 99, 277–291.

Masotta, M., Pontesilli, A., Mollo, S., Armienti, P., Ubide, T., Nazzari, M., Scarlato, P., 2020. The role of undercooling during clinopyroxene growth in trachybasaltic magmas: Insights on magma decompression and cooling at Mt. Etna volcano. Geochim. Cosmochim. Acta 268, 258–276.

Mollo, S., Del Gaudio, P., Ventura, G., Iezzi, G., Scarlato, P., 2010. Dependence of clinopyroxene composition on cooling rate in basaltic magmas: implications for thermobarometry. Lithos 118, 302–312.

Mollo, S., Misiti, V., Scarlato, P., Soligo, M., 2012. The role of cooling rate in the origin of high temperature phases at the chilled margin of magmatic intrusions. Chem. Geol. 322–323, 28–46.

Mollo, S., Blundy, J.D., Iezzi, G., Scarlato, P., Langone, A., 2013. The partitioning of trace elements between clinopyroxene and trachybasaltic melt during rapid cooling and crystal growth. Contrib Mineral Petrol 166, 1633–1654.

Mollo, S., Masotta, M., 2014. Optimizing pre-eruptive temperature estimates in thermally and chemically zoned magma chambers. Chem. Geol. 368, 97–103.

Mollo, S., Giacomoni, P.P., Andronico, D., Scarlato, P., 2015a. Clinopyroxene and titanomagnetite cation redistributions at Mt. Etna volcano (Sicily, Italy): footprints of the final solidification history of lava fountains and lava flows. Chem. Geol. 406, 45–54

Mollo, S., Giacomoni, P.P., Coltorti, M., Ferlito, C., Iezzi, G., Scarlato, P., 2015b. Reconstruction of magmatic variables governing recent Etnean eruptions: constraints from mineral chemistry and P–T–fO2–H2O conditions. Lithos 212–215, 311–320.

Mollo, S., Hammer, J.E., 2017. Dynamic crystallization in magmas. In: EMU Notes in Mineralogy. 16. pp. 373–418.

Mollo, S., Blundy, J., Scarlato, P., De Cristofaro, S.P., Tecchiato, V., Di Stefano, F., Vetere, F., Holtz, F., Bachmann, O., 2018. An integrated P-T-H2O-lattice strain model to quantify the role of

clinopyroxene fractionation on REE+Y and HFSE patterns of mafic alkaline magmas: Application to eruptions at Mt. Etna. Earth Sci Rev 185, 32–56.

Morgan, D.J., Jerram, D.A., 2006. On estimating crystal shape for crystal size distribution analysis. J. Volcanol. Geotherm. Res. 154, 1–7.

Murru, M., Montuori, C., Wyss, M., Privitera, E., 1999. The locations of magma chambers at Mt. Etna, Italy, mapped by b-values. Geophys. Res. Lett. 26, 2553–2556.

Nascimento, M.L.F., Ferreira, E.B., Zanotto, E.D., 2004. Kinetics and mechanisms of crystal growth and diffusion in a glass-forming liquid. J. Chem. Phys. 121, 8924–8928.

Orlando, A., D'Orazio, M., Armienti, P., Borrini, D., 2008. Experimental determination of plagioclase and clinopyroxene crystal growth rates in an anhydrous trachybasalt from Mt Etna (Italy). European Journal of Mineralogy 20, 653–664.

Patanè, D., De Gori, P., Chiarabba, C., Bonaccorso, A., 2003. Magma Ascent and the Pressurization of Mount Etna's Volcanic System. Science 299, 2061–2063.

Perinelli, C., Mollo, S., Gaeta, M., De Cristofaro, S.P., Palladino, D.M., Armienti, P., Scarlato, P., Putirka, K.D., 2016. An improved clinopyroxene-based hygrometer for Etnean magmas and implications for eruption triggering mechanisms. Am. Mineral. 101, 2774–2777.

Perinelli, C., Mollo, S., Gaeta, M., De Cristofaro, S.P., Palladino, D.M., Scarlato, P., 2018. Impulsive supply of volatile-rich magmas in the shallow plumbing system of Mt. Etna Volcano. Minerals 8, 482.

Petrone, C.M., Bugatti, G., Braschi, E., Tommasini, S., 2016. Pre-eruptive magmatic processes re-timed using a non-isothermal approach to magma chamber dynamics. Nat Commun 7.

Petrone, C.M., Braschi, E., Francalanci, L., Casalini, M., Tommasini, S., 2018. Rapid mixing and short storage timescale in the magma dynamics of a steady-state volcano. Earth Planet. Sci. Lett. 492, 206–221.

Polacci, M., Arzilli, F., La Spina, G., Le Gall, N., Cai, B., Hartley, M.E., Di Genova, D., Vo, N.T., Nonni, S., Atwood, R.C., Llewellin, E.W., Lee, P.D., Burton, M.R., 2018. Crystallisation in basaltic magmas revealed via in situ 4D synchrotron X-ray microtomography. Sci Rep 8, 8377–8383.

Polacci, M., Andronico, D., de' Michieli Vitturi, M., Taddeucci, J., Cristaldi, A., 2019. Mechanisms of Ash Generation at Basaltic Volcanoes: The Case of Mount Etna, Italy. Front. Earth Sci. 7.

Pontesilli, A., Masotta, M., Nazzari, M., Mollo, S., Armienti, P., Scarlato, P., Brenna, M., 2019. Crystallization kinetics of clinopyroxene and titanomagnetite growing from a trachybasaltic melt: New insights from isothermal time-series experiments. Chem. Geol. 510, 113–129.

Putirka, K., 2008. Thermometers and barometers for volcanic systems. Rev. Mineral. Geochem. 69, 61–120. http://dx.doi.org/10.2138/rmg.2008.69.3.

Ratkowsky, D.A., 1990. Handbook of Non-linear Regression Models. Marcel Decker Inc., New York.

Rutherford, M.J., Hill, P.M., 1993. Magma ascent rates from amphibole breakdown: An experimental study applied to the 1980-1986 Mount St. Helens eruptions. J. Geophys. Res. 98, 19667–19685.

Rutherford, M.J., 2008. Magma Ascent Rates. Rev Mineral Geochem 69, 241–271.

Schanofski, M., Fanara, S., Schmidt, B.C., 2019. CO2–H2O solubility in K-rich phonolitic and leucititic melts. Contrib Mineral Petrol 174.

Shea, T., and Hammer, J.E., 2013. Kinetics of cooling- and decompression-induced crystallization in hydrous mafic-intermediate magmas. J. Volcanol. Geotherm. Res., 260, 127–145.

Simakin, A.G., Salova T.P., Armienti P., 2003. Kinetics of clinopyroxene growth from a hydrous hawaiite melt. Geochemistry Int. 41, 1275-1286.

Sunagawa, I., 1981. Characteristics of crystal growth in nature as seen from the morphology of mineral crystals. Bull. Mineral. 104, 81–87.

Sunagawa, I., 2005. Crystals: Growth, Morphology and Perfection. Cambridge University Press, Cambridge.

Toramaru, A., 1991. Model of nucleation and growth of crystals in cooling magmas. Contr. Mineral. and Petrol. 108, 106–117.

Toramaru, A., Noguchi, S., Oyoshihara, S., Tsune, A., 2008. MND(microlite number density) water exsolution rate meter. J. Volcanol. Geotherm. Res. 175, 156–167.

Ubide, T., Kamber, B.S., 2018. Volcanic crystals as time capsules of eruption history. Nat Commun 9.

Ubide, T., Mollo, S., Zhao, J., Nazzari, M., Scarlato, P., 2019a. Sector-zoned clinopyroxene as a recorder of magma history, eruption triggers, and ascent rates. Geochim. Cosmochim. Acta 251, 265–283.

Ubide, T., Caulfield, J., Brandt, C., Bussweiler, Y., Mollo, S., Di Stefano, F., Nazzari, M., Scarlato, P., 2019b. Deep Magma Storage Revealed by Multi-Method Elemental Mapping of Clinopyroxene Megacrysts at Stromboli Volcano. Front. Earth Sci. 7.

Vetere, F., Iezzi, G., Behrens, H., Holtz, F., Ventura, G., Misiti, V., Cavallo, A., Mollo, S., Dietrich, M., 2015. Glass forming ability and crystallization behavior of sub-alkaline silicate melts. Earth Sci Rev 150, 25–44.

Vetere, F., Iezzi, G., Behrens, H., Cavallo, A., Misiti, V., Dietrich, M., Knipping, J., Ventura, G., Mollo, S., 2013. Intrinsic solidification behaviour of basaltic to rhyolitic melts: a cooling rate experimental study. Chem. Geol. 354, 233–242.

Webb, S.L., Dingwell, D.B., 1995. Viscoelasticity. Rev. Mineral. Geochem. 32, 95–119.

Weill, D.E., Hon, R., Navrotsky, A., 1980. The igneous system CaMgSi2O6-CaAlaSi2O6-NaAlSi3O6: variations on a classic theme by Bowen. In: Hargraves RB (ed) Physics of magmatic processes. Princeton University Press, Princeton, pp 49-92

Welsch, B., Hammer, J., Baronnet, A., Jacob, S., Hellebrand, E., Sinton, J., 2016. Clinopyroxene in postshield Haleakala ankaramite: 2. Texture, compositional zoning and supersaturation in the magma. Contrib. Mineral. Petrol. 171, 6.

Yilmaz, S., Özkan, O.T., Günay, V., 1996. Crystallization kinetics of basalt glass. Ceram. Int. 22, 477–481.

Zhang, Y., Ni, H., Chen, Y., 2010. Diffusion data in silicate melts. Rev. Mineral. Geochem. 72, 311–408.

Figure captions

Figure 1. Example of BSE (back-scattered electron) photomicrographs processed via NIH Image J software and reduced to binary type images (i.e., black vs. white color) by grey level thresholding (i.e., image segmentation; Armienti, 2008). A Matlab© code is also reported in Supplementary Material 1 to perform image processing operations in conjunction with NIH Image J. The retrieved textural parameters are 1) the equal-area best-fit ellipses and lengths of major (L) and minor (W) axes, 2) the surface area per unit volume, and 3) the area fraction of a given population within a plane that is comparable to its volume fraction. Bright BSE intensity phases refer to titanomagnetite crystals.

Figure 2. Selected BSE (back-scattered electron) photomicrographs representative of run products from *Experimental Set ISO, Experimental Set ΔP*, and *Experimental Set CR*. Bright BSE intensity phases refer to titanomagnetite crystals.

Figure 3. Variation of clinopyroxene content (% area) as a function of experimental conditions. Data refer to *Experimental Set ISO* and *Experimental Set ΔP* (a), and *Experimental Set CR* (b). Error bars refer to the uncertainties reported in Table 1.

Figure 4. Variation of 3D aspect ratio (S_v^P) as a function of experimental conditions. Data refer to *Experimental Set ISO* and *Experimental Set ΔP* (a), and *Experimental Set CR* (b). Error bars refer to the uncertainties reported in Table 1.

Figure 5. Total alkali *versus* silica (a) and Di + Hd *versus* CaTs + CaTiTs (b) diagrams showing experimental glass and clinopyroxene compositions, respectively. Natural compositions from eruptions at Mt. Etna volcano are also displayed for comparison.

Figure 6. Variation of $\ln G_{max}$ as a function of experimental conditions. Data refer to *Experimental Set ISO* and *Experimental Set ΔP* (a), and *Experimental Set CR* (b). Values of G_{max} modeled through the thermodynamic expression of crystal growth (cf. Armienti, 2008) are also displayed for comparison. According to Eqn. (6) reported in the text, thermodynamic data can be calculated for $\Delta T \geq 0$. Error bars refer to the uncertainties reported in Table 1.

Figure 7. Thermodynamic modeling of crystal growth kinetics for the transition between interface-controlled and diffusion-controlled growth regimes arising at undercooling higher than 30 °C. Modeled trends are depicted in green and blue for temperatures of 1,050 and 1,100 °C, respectively. In order to isolate the effect of ΔT, modeled trends are also compared with values of G_{max} (green and blue diamonds for 1,050 and 1,100 °C, respectively) from decompression and cooling rate experiments conducted over similar relaxation times (i.e., in the order of minutes for *ΔPf-1100-2H2O, ΔPf-1100-5H2O, ΔPf-1100-H2O+CO2, ΔPf-1050-2H2O, ΔPf-1050-5H2O, ΔPf-1050-H2O+CO2, CR-1050-0.25, CR-1050-0.5*).

Figure 8. Regression plot of maximum growth rate (G_{max}) *versus* experimental time (t) on a logarithmic scale (a). Data from this study are compared with those from previous experimental works investigating basaltic and trachybasaltic compositions that virtually reproduce the overall intrinsic variability of Monte Maletto Formation. Experiments were performed at conditions comparable with those of magmas erupted at Mt. Etna volcano (i.e., P = 0.1-1,000 MPa, T = 1,050-1,150 °C, H_2O = 0-4 wt.%, fO_2 = NNO+1.5-

NNO+2, ΔT = 75-233 °C, and CR = 0.001-100 °C s^{-1}; Baker, 2008; Mollo et al., 2013; Pontesilli et al., 2019; Masotta et al., 2020). Probability density functions of regression coefficients β_0 (b) and β_1 (c) obtained from Monte Carlo simulations, as well model uncertainty associated with the estimate of t_{max} (d) are also displayed.

Figure 9. Saturation conditions calculated for clinopyroxene crystals from 2011-2012 lava fountains erupted at Mt. Etna volcano. Uncorrected equilibrium between microphenocryst and bulk rock compositions has been determined for values of $Kd_{Fe\text{-}Mg}$ (Fe-Mg exchange partition coefficient; Putirka, 2008), K_{Na} (Na partition coefficient; Blundy et al., 1995), and *DiHd* (diopside + hedenbergite; Mollo et al., 2013). The equilibrium state of the bulk system has been corrected by minimizing the difference (Δ) between measured and predicted values. Using the model of Mollo et al. (2018), P-T-H_2O estimates have been adjusted within the calibration errors of the barometer (±150 MPa), thermometer (±20 °C), and hygrometer (±0.45 wt.% H_2O), in order to minimize the overall uncertainty.

Figure 10. Crystal size distribution (CSD) analysis of clinopyroxene crystals from 2011-2012 lava fountains erupted at Mt. Etna volcano. *N(L) versus L* curves attest the occurrence of two distinct microphenocryst and microlite populations.

Figure 11. Conceptual model of magma dynamics at Mt. Etna volcano describing the different time scales estimated for microlite and microphenocryst crystallization. Magma ascent velocities are also modeled accounting for either slow magma ascent rates within the interconnected storage regions forming the plumbing system architecture at depth or fast magma ascent rates within the uppermost part of the volcanic conduit and before eruption at the vent.

Parameterization of clinopyroxene growth kinetics via crystal size distribution (CSD) analysis: Insights into the temporal scales of magma dynamics at Mt. Etna volcano

[1*]Piergiorgio Moschini, [1,2]Silvio Mollo, [1]Mario Gaeta, [3]Sara Fanara, [2]Manuela Nazzari, [4]Chiara Maria Petrone, [2]Piergiorgio Scarlato

[1]Department of Earth Sciences, Sapienza - University of Rome, P. le Aldo Moro 5, 00185 Roma, Italy

[2]Istituto Nazionale di Geofisica e Vulcanologia - Department Roma 1, Via di Vigna Murata 605, 00143 Roma, Italy

[3]Abteilung Experimentelle und Angewandte Mineralogie, Georg August Universität Göttingen, Goldschmidtstraße 1, 37077 Göttingen, Germany

[4]The Natural History Museum, Department of Earth Sciences, Cromwell Road, SW7 5BD, London, United Kingdom

*Corresponding author:
Piergiorgio Moschini
piergiorgio.moschini@uniroma1.it
Department of Earth Sciences
Sapienza - University of Rome
P. le Aldo Moro 5
00185 Roma, Italy

Abstract

There is increasing recognition that both textural and compositional changes of clinopyroxene crystallizing from mafic alkaline magmas are the direct expression of complex dynamic processes extending over a broad range of spatial and temporal scales. Among others, supersaturation and relaxation phenomena play a key role in controlling the final crystal cargo of variably undercooled magmas erupted from active alkaline volcanoes. Following this line of reasoning, we have carried out isothermal-isobaric, decompression, and cooling rate experiments on a basalt interpreted as the parental magma of mafic alkaline eruptions at Mt. Etna volcano (Sicily, Italy). The main purpose is to reconstruct and quantify the textural changes (i.e., length of major and minor axes, surface area per unit volume, area fraction, and maximum growth rate) of clinopyroxene at variable pressures (30-300 MPa), temperatures (1,050-1,100 °C), volatile contents (0-5 wt.% H_2O and 0-0.2 wt.% CO_2), and equilibration times (0.25-72 h). Melt supersaturation, corresponding to a degree of undercooling variable from 14 to 125 °C, drives the formation of clinopyroxene crystals with different textures and sizes as a function of growth rate and relaxation time. By integrating experimental data and thermodynamic modeling, the transition between interface-controlled (euhedral morphologies) and diffusion-controlled (anhedral morphologies) growth regimes has been determined to occur at degrees of undercooling higher than 30 °C. The decrease of clinopyroxene growth rate with increasing the equilibration time is combined with the crystal size distribution (CSD) analysis of naturally undercooled clinopyroxene crystals erupted during 2011-2012 lava fountain episodes at Mt. Etna volcano. Results indicate that the crystallization of microlites and microphenocrysts is on the order of ~10^0-10^1 min (large undercooling, short equilibration time) and ~10^1-10^2 h (small undercooling, long equilibration time), respectively. This temporal information allows to better constrain the cooling-decompression paths of Etnean magmas rising and accelerating along a vertically extended, highly dynamic plumbing system. While clinopyroxene microlites develop during the fast ascent of magmas (~10^0-10^1 m s^{-1}) within the uppermost part of the conduit or immediately before ejection from the vent, the onset of microphenocryst crystallization occurs at depth and continues within the plumbing system during the slow ascent of magmas (~10^{-2} m s^{-1}) that migrate through interconnected storage regions.

Keywords: basalt; clinopyroxene; crystallization kinetics; crystal size distribution (CSD); magma cooling and decompression; magma ascent rate; Mt. Etna volcano.

1. Introduction

Clinopyroxene is an important recorder of the physico-chemical changes explored by mafic alkaline magmas typically occurring in intraplate settings. Owing to its ubiquitous crystallization over a broad range of pressures, temperatures, and volatile contents (e.g., Mollo et al., 2018), a gamut of studies have investigated the clinopyroxene textural and compositional variations in alkaline products, with the main purpose of elucidating pre-eruptive magma storage conditions at depth and syn-eruptive dynamics during ascent of magma towards the surface (e.g., Petrone et al., 2016, 2018; Ubide and Kamber, 2018).

While the stability field of clinopyroxene is intrinsically related to the intensive and extensive variables governing the thermodynamic reactions at the interface between crystal, melt, and fluid phases, a certain degree of undercooling (ΔT) is essential to promote the growth and textural maturation of clinopyroxene. ΔT is the thermodynamic driving force of crystallization and can be defined as the difference between the temperature at which a specific mineral saturates the melt and the temperature of a naturally solidifying system. In single-step undercooling experiments characterized by a rapid, large drop in pressure-temperature, the melt composition can be assumed constant during the decompression-cooling path controlling ΔT. As a consequence, the degree of supersaturation of the mineral-forming components can be linked and quantified directly through the magnitude of ΔT (Shea and Hammer, 2013 and references therein). Several reviews examined the phenomenological aspects related to the kinetics of crystal nucleation and growth (e.g., Kirkpatrick, 1981; Cashman, 1990; Lasaga, 1998; Hammer, 2006; Iezzi et al., 2014; Mollo and Hammer, 2017; Giuliani et al., 2020), along with increasing emphasis on the importance of magma supersaturation state to resolve specific petrological and volcanological problems involving the environmental conditions of magmatic reservoirs and their dynamic evolutions.

Recently, some authors (Hammer et al., 2016; Welsch et al., 2016; Ubide et al., 2019a, 2019b; Di Stefano et al., 2020) focused their attention on the profound effect exercised by ΔT on the morphology and composition of clinopyroxene growing from mafic alkaline magmas, such as those erupted at Haleakala (Hawaii) and Mt. Etna and Stromboli (Italy). These authors documented that systematic departure from equilibrium arises by composite growth histories driven by imbalance between the rate at which the crystal surfaces advance and the rate of cation diffusion in the melt. In particular, for magmas erupted at Mt. Etna, it has been experimentally found that strong supersaturation effects correspond to large ΔT, leading to disequilibrium uptake of incompatible cations at the crystal-melt interface. These rate-limiting concentration gradients promote high nucleation rates and fast development of small, anhedral clinopyroxene crystals (Polacci et al., 2018; Arzilli et al., 2019; Masotta et al., 2020). Conversely, under the driving force of small ΔT, the bulk system attempts to return to a near-equilibrium

state between the advancing crystal surfaces and the melt composition. Because of the effect of growth kinetics, large, euhedral clinopyroxene crystals develop by minimizing the interfacial free energy between crystal and surrounding melt. Time-series experiments have also outlined that the shift from a diffusion-controlled to an interface-controlled growth regime is intimately governed by relaxation phenomena lowering the concentration gradients at the crystal-melt interface and leading to a steady-state textural maturation of clinopyroxene (Pontesilli et al., 2019). After initial supersaturation effects, the growth rate of clinopyroxene progressively decreases with increasing relaxation time, thereby approaching to a near-equilibrium condition where attachment/detachment reactions of cations from the melt onto the crystalline surface (and *vice versa*) occur at the same rate (Pontesilli et al., 2019). These time-series experiments also corroborate the textural maturation model proposed by Welsch et al. (2016) for the growth of large clinopyroxene phenocrysts from ankaramite lava flows erupted at Haleakala. According to the authors, the external morphology, chemical variation, and internal structure of these phenocrysts testify to a continuous growth rate decrease over time, in response to less effective supersaturation conditions driving gradual transition between diffusion-controlled and interface-controlled regimes (Welsch et al., 2016).

On the basis of previous laboratory data from Pontesilli et al. (2019) and Masotta et al. (2020), we have conducted complementary isothermal-isobaric, decompression, and cooling rate experiments on a primitive basalt from Mt. Etna, in order to assess the control of supersaturation and relaxation phenomena on clinopyroxene crystallization. In agreement with crystal growth thermodynamics and kinetics, the textural maturation of clinopyroxene is attained at small undercoolings and long equilibration times. Under such conditions, we measure a growth rate decay of six orders of magnitude that is modeled as a function of relaxation kinetics. This empirical relationship is interpolated to the algebraic expression of crystal size distribution (CSD) analysis, with the final purpose of quantifying the time scale of crystallization during decompression-cooling of mafic alkaline magmas. As a test case, microlites and microphenocrysts from scoria clasts ejected during 2011-2012 lava fountains at Mt. Etna have been considered. Results from calculations give rise to a conceptual model for the time scale of magma dynamics recorded by the (dis)equilibrium textural evolution of clinopyroxene and for the rapid acceleration of magma ascending within the volcanic conduit, immediately before eruption at the vent.

2. Methods

2.1. Experimental strategy

The starting material used for the experiments is a natural basalt from the Monte Maletto Formation erupted at Mt. Etna around 7,000 years ago. Monte Maletto Formation comprises basaltic to trachybasaltic products that have been interpreted by numerous authors as the parental compositions of historic and recent Etnean eruptions (see the review study of Mollo et al., 2018 and references therein). The powdered rock was melted to ensure homogeneity of the final starting material at the HP-HT Laboratory of Experimental Volcanology and Geophysics of the Istituto Nazionale di Geofisica e Vulcanologia (INGV), Rome, Italy. A crucible containing the natural powder was loaded in a 1 atm vertical tube CO–CO_2 gas-mixing furnace at 1,300 °C for 1 h. The redox state was 2 log unit above the Ni-NiO buffer (NNO+2), comparable to that estimated at the Mt. Etna (Mollo et al., 2015a). Iron loss was kept to < 5% of the initial amount by adopting an Fe pre-saturated Pt crucible. The quenched glass was analyzed by scanning electron microscopy and no crystalline phases were detected. Twenty microprobe analyses of the glass yielded an average composition (in wt.%) of 47.56 (±0.39) SiO_2, 1.48 (±0.11) TiO_2, 15.42 (±0.23) Al_2O_3, 10.79 (±0.17) FeO_{tot}, 0.21 (±0.04) MnO, 7.98 (±0.15) MgO, 12.13 (±0.18) CaO, 2.61 (±0.13) Na_2O, 1.25 (±0.12) K_2O, and 0.57 (±0.04) P_2O_5.

Isothermal and decompression experiments were carried out in an internally heated pressure vessel (IHPV) equipped with a continuum decompression system and a rapid quenching device (drop quench) at the Abteilung Experimentelle und Angewandte Mineralogie, Georg August Universität Göttingen (Germany). The powdered starting glass was loaded in Fe-presaturated Pt-capsules. Isobaric experiments (*Experimental Set ISO*) were conducted at 300 MPa and temperatures of 1,100 (*ISO-1100*), 1,075 (*ISO-1075*), and 1,050 °C (*ISO-1050*) that were kept constant over an equilibration time of ~24 hours (Table 1). The experiments were heated directly to the target temperature at a rate of 50 °C/min and were carried out under nominally anhydrous and hydrous conditions, corresponding to 0 wt.% $H_2O_{initial}$ (*ISO-0H2O*, i.e., nominally anhydrous system), 2 wt.% $H_2O_{initial}$ (*ISO-2H2O*), 5 wt.% $H_2O_{initial}$ (*ISO-5H2O*), and 2 wt.% $H_2O_{initial}$ + 0.2 wt.% $CO_{2initial}$ (*ISO-H2O+CO2*). H_2O and CO_2 were added as deionized water and oxalic acid, respectively. Decompression experiments (*Experimental Set ΔP*) were conducted at the same temperatures and anhydrous-hydrous conditions by depressurizing the charges from 300 to 30 MPa at slow (*ΔPs*) and fast (*ΔPf*) rates of 0.018 and 0.98 MPa s^{-1}, respectively (Table 1). Pressures, temperatures, and melt-H_2O+CO_2 contents have been selected in order to reproduce the most common crystallization-degassing path of magmas at Mt. Etna, as derived by thermobarometric-hygrometric calculations and melt inclusion data (Mollo et al., 2018 and references therein). Slow to fast decompression experiments correspond to magma ascent velocities in the range of 0.45-24.5 m s^{-1}, in agreement with previous estimates suggested by geophysical, crystallochemical, and numerical studies

focusing on magma conduit dynamics at Mt. Etna (Aloisi et al., 2006; Mollo et al., 2015b; La Spina et al., 2016; Giuffrida et al., 2017). Note that the solubility of H_2O in this melt composition is ~2.9 and ~0.5 wt.% at 300 (i.e., fluid-absent) and 30 (i.e., fluid-present) MPa, respectively, as derived by the thermodynamic model of Duan (2014) and corroborated by numerous studies carried out on mafic alkaline magmas (Mollo et al., 2018 and references therein). Coherently, magma dynamics at Mt. Etna volcano are frequently recognized as the result of complex crystallization regimes that, at shallow crustal levels, change from H_2O-undersaturated to H_2O-saturated (i.e., $P_{H2O} = P_{total}$) conditions, in conjunction with abundant volatile degassing (Mollo et al., 2015b, 2018; Perinelli et al., 2016, 2018). The temperature was monitored by three S-type (Pt90Rh10/Pt with uncertainty of ±3 °C) thermocouples and pressure was recorded by a transducer, calibrated against a Heise tube gauge with accuracy ±5 MPa. Experiments were quenched using a drop quench device imposing a cooling rate of ~150 °C s^{-1}. Recovered charges were mounted in epoxy and polished thin sections was produced from the epoxy blocks. The use of Ar as a pressure medium provided an intrinsic fO_2 variable from NNO+2 to NNO+4 (Schanofski et al., 2019). Within the sample capsule, fH_2 was controlled by hydrogen permeation through the capsule walls driven by the fugacity gradient between the pressure medium and the capsule interior. This in turn determined the fO_2 inside the capsule through the equilibrium $H_2 + 1/2\ O_2 \leftrightarrow H_2O$. However, under fluid-present conditions and with the addition of CO_2, the redox state of the system changed in response to the variable activity of H_2O in the melt (Botcharnikov et al. 2008). In this respect, the redox state of the system was estimated at the end of experimental runs through the oxygen barometer of Ishibashi (2013) based on spinel–melt equilibria and with uncertainty (±0.3 log unit). This model was calibrated using an alkaline data set, returning fO_2 estimates variable from NNO+1.9 and NNO+2.3 buffer (Mollo et al., 2015a).

Cooling rate experiments (Table 1) were carried out in a non-end loaded piston cylinder apparatus ("QUICKpress", Depths of the Earth co.) using a 19-mm NaCl-pyrex-graphite-MgO assembly that produced an apparent redox state close to NNO+2 buffer (Mollo and Masotta, 2014). The assembly was loaded with a Fe-presaturated Pt-capsule containing the hydrous (2 wt.% $H_2O_{initial}$) glass. The capsules were surrounded by powdered pyrophyllite to prevent H_2O loss and enhance stress homogenization during initial compression. After cold pressurization to a nominal pressure 10% higher than desired, the pressure was decreased down to 300 MPa. The temperature was monitored by a factory-calibrated C-type (W-5Re/W-26Re) thermocouple, which gives an uncertainty of ±3 °C. Following Masotta et al. (2020), the experiments were carried out by heating the starting glass to superliquidus condition of 1,300 °C at a rate of 80 °C min^{-1}. After 30 min, the temperature was cooled to 1,050 °C at the same rate of 80 °C min^{-1} (*Experimental Set CR*). This isothermal condition was kept constant for 0.25 (*CR-025*),

0.5 (*CR-05*), 1 (*CR-1*), 4 (*CR-4*), 24 (*CR-24*), and 72 (*CR-72*) hours, before isobaric quench at a rate of 100 °C s^{-1} (Table 1).

As a whole, *Experimental Set ISO*, *Experimental Set ΔP*, and *Experimental Set CR* were carried out at the temperatures (i.e., 1,100, 1,075, and 1,050 °C) more frequently encountered during the crystallization of clinopyroxene at Mt. Etna volcano (e.g., Mollo et al., 2018). Similarly, the pressure condition of 300 MPa corresponds to a magma storage region at an intermediate depth of 7-13 km (Murru et al., 1999) where microphenocrysts of clinopyroxene initiate to nucleate and grow during magma ascent towards the surface (e.g., Mollo et al., 2015b). In this context, *Experimental Set ISO* approached from the solidus directly to the subliquidus temperature (i.e., nominal $\Delta T = 0$) in order to quantify the textural parameters of clinopyroxene under interface-controlled growth regimes. Conversely, *Experimental Set ΔP* and *Experimental Set CR* were designed to impose variable supersaturation conditions (i.e., actual ΔT = 14-125 °C; Table 1), leading to diffusion-controlled growth regimes and clinopyroxene textural changes.

2.2. Image processing and CSD correction

Photomicrographs of the experimental products were collected in backscattered electron (BSE) mode of a JEOL 6500F field emission gun scanning electron microscope (FE-SEM) equipped with an energy-dispersive spectrometer (EDS) detector at the HP-HT Lab of INGV.

The acquired photomicrographs were processed via NIH Image J software and reduced to binary type images (i.e., black and white color) by grey level thresholding (i.e., image segmentation; Armienti, 2008). The segmentation method was employed to identify clinopyroxene microphenocrysts and microlites relative to other mineral phases (Fig. 1). The uncertainty associated with the segmentation process and the identification of larger crystals growing by attachment of smaller ones has been evaluated according to the method reported in Pontesilli et al. (2019) and based on the addition/subtraction of pixel layers around each crystal in the binary image. A Matlab© code (see Supplementary Material 1) was developed to perform image processing operations in conjunction with NIH Image J. The retrieved textural parameters were 1) the equal-area best-fit ellipses and lengths of major (L) and minor (W) axes (Fig. 1), 2) the surface area per unit volume (S_v^P as 3D aspect ratio; Table1), and 3) the area fraction of a given population within a plane that is comparable to its volume fraction (ϕ). Following one of the most common methods reported in literature (cf. Pontesilli et al., 2019 and references therein), L and W data were used to calculate the maximum growth rate (G_{max} in mm s^{-1}) of clinopyroxene, as an average of the ten largest crystals measured in each experimental run (Supplementary Material 2):

$$G_{max} = (L\,W)^{0.5} / (2\,t) \quad (1)$$

where t is the experimental time.

The magnitude of S_v^P was determined for the experimental crystals as (Hammer, 2006; First and Hammer, 2016):

$$S_v^P = S_v^T / \phi \quad (2)$$

S_v^T is the total interfacial area of a population per unit volume of sample and can be expressed as $2 \times N_L$, where N_L is the density of phase boundary intersections in a given length of randomly oriented test line. The Matlab© code from this study allows to overlay the desired number of circular test lines over a binary type image (Fig. 1) and determine the N_L value by counting the locus of points where crystal-melt boundaries intersect the test lines. The lower is the magnitude of S_v^P parameter, the higher is the crystal euhedrality. Therefore, clinopyroxene crystals characterized by S_v^P < 1,000 mm^{-1} are interpreted as euhedral, whereas crystal with S_v^P >1,000 mm^{-1} are anhedral (Hammer, 2008). S_v^P data listed in Table 1 are the mean resulting from the analysis of eight binary type images for sample, each one overlaid by six circles with radius variable as a function of BSE image magnification (Fig. 1).

CSD analysis was carried out on BSE images of natural rock samples from 2011-2012 lava fountains outpoured at Mt. Etna volcano. Textural data were collected at ×500 and ×100 magnifications for microlites (<0.1 mm) and microphenocrysts (≥0.1 mm) populations, respectively, and then combined each other to obtain one single CSD curve. Intersection planar data were converted in volume data by applying stereological correction (Higgins, 2000), in order to gain information on the contribution of larger crystals to the population of smaller ones. This correction method accounts for 1) potential cut-section effects in case of larger crystals are cut by a plane shifted with respect to the center, therefore contributing to smaller crystal populations, and 2) intersection probability effects when, for a poly-disperse distribution, smaller crystals are less likely to be intersected by a plane than larger crystals (Higgins, 2000). The crystal shape, assumed as the crystal aspect ratio S:I:L of short:intermediate:long dimensions (Higgins, 2000), was determined by the Excel© spreadsheet *CSDslice* developed by Morgan and Jerram (2006). Through this model, 2D raw data were compared with a crystal habit database (i.e., S:I:L of 1:10:10, 1:1:10, and 1:1:1) to constrain the five best-matching crystal shapes. The best linear binning was selected for each sample by the procedure reported in Armienti (2008) for the minimization

of residuals between the particles effectively measured and those re-calculated by CSD analysis (zeroth moment of the distribution):

$$N_{tot} = Area \sum L_i \, N_V(L_i) \quad (3)$$

where L_i is the major axis length of crystal and N_V is the volumetric number density. This latter parameter is calculated as the ratio of the area number density (N_A) to the characteristic crystal size (L_D). The routine of Armienti (2008) requires also the minimization of residuals between the measured volume crystal fraction and the volume resulting from CSD analysis (third moment of the distribution):

$$V_f = \sum N_V\,(L_i)\,\frac{4}{3}\pi\left(\frac{L_i}{2}\right)^3 = \frac{\pi}{6}\sum {L_i}^3 N_V(L_i) \quad (4)$$

According to Eqns. (3) and (4), a linear binning ΔL of 0.02 mm was derived, for a total of 21 classes ranging from 0.006 to 0.406 mm. Crystals with L < 0.006 mm (i.e., artefacts caused by image segmentation) and crystal fragments at the edge of photomicrographs were removed from the dataset (Armienti et al., 1994). The program *CSDCorrections* 1.38 of Higgins (2000) was finally employed to calculate a binned CSD curve for different crystal size classes by specifying the crystal shape values reported in Supplementary Material 3, rock fabric of massive type, and crystal roundness factor of 0.5. The formulated CSD diagrams are in the form of semi-logarithmic plots based on ln *N(L)* vs. *L* that describe the evolution of crystal size as (Marsh, 1988):

$$\ln N(L) = \frac{-L}{G\,\tau} + \ln N_0 \quad (5)$$

where *N(L)* is the number of crystals per size of length *L* per unit volume (i.e., the density distribution of crystals per unit volume per bin size), *G* is the crystal growth rate, τ is the time of a system crystallizing at steady state, and N_0 is the nucleation density (i.e., the number of crystals of zero size). When the dominant size of the crystal population results from steady growth over an appropriate duration of time, the linear regression fit of CSD curve has slope $m = 1 / (G \times \tau)$ and intercept $b = \ln(N_0)$. According to previous works focused on crystallization kinetics (see the review study of Giuliani et al., 2020 and references therein), the decrease of *m* with increasing crystal size may reflect the growth of early-formed nuclei by agglomeration and attachment. Under such kinetic growth conditions, both *m* and *b* parameters

are strictly correlated with the variation of temperature as a function of time, and G_{max} linearly decreases with decreasing $\Delta T/\Delta \tau$ (cf. Giuliani et al., 2020). CSD statistics were obtained from the quantitative study of 16 thin sections and 243 photomicrographs. CSD plots were constructed considering ~1,500-4,000 crystals.

2.3. Microanalysis

Major element concentrations were obtained at the HP-HT Lab of INGV using a JEOL-JXA8200 electron probe micro-analyzer (EPMA) equipped with five wavelength dispersive spectrometers (Supplementary Material 4). For glasses, a slightly defocused 3 μm beam was used with a counting time of 5 s on background and 15 s on peak. For crystals, beam size was 1 μm with a counting time of 20 and 10 s on peak and background, respectively. The following standards were used for calibration: jadeite (Si and Na), corundum (Al), forsterite (Mg), andradite (Fe), rutile (Ti), orthoclase (K), barite (Ba), apatite (P), spessartine (Mn) and chromite (Cr). Sodium and potassium were analyzed first to prevent alkali migration effects. The precision of the microprobe was measured through the analysis of well-characterized synthetic standards. Based on counting statistics, analytical uncertainties relative to their reported concentrations indicate that precision and accuracy were better than 5% for all cations.

3. Results

3.1. Textural features

Selected BSE photomicrographs representative of run products from *Experimental Set ISO*, *Experimental Set ΔP*, and *Experimental Set CR* are displayed in Figs. 1 and 2 (note that photomicrographs of all the experiments are reported in Supplementary Material 2). The mineral assemblage consists of abundant clinopyroxene and titanomagnetite, with subordinate plagioclase (in order of crystallization sequence).

Clinopyroxene crystals from *Experimental Set ISO* show euhedral morphologies, with a great number of well-faced crystals (Figs. 1 and 2) and L_{max} variable from 0.07 to 0.23 mm (Supplementary Material 2). Run products are characterized by a dense mosaic of either isolated or aggregated microlites, suggesting rapid attainment of an interface-controlled crystal growth regime. Indeed, most of clinopyroxene crystallization initiated upon crossing the glass transition temperature (Tg = 723 °C, Giordano et al., 2005) and further continued over time (i.e., there is no effective ΔT caused by cooling and/or decompression). The amount of residual glass found in the experimental charges increases with increasing T and $H_2O_{initial}$ (Figs. 1 and 2, and Supplementary Material 2). In contrast, the presence of CO_2

lowers the amount of H_2O dissolved in the melt, raising the liquidus temperature of the experimental system and increasing the crystal content (Supplementary Material 2).

Clinopyroxene crystals from *Experimental Set ΔP* consist of sector-zoned crystals with prismatic shapes and well-formed planar edges (Figs. 1 and 2, and Supplementary Material 2). L_{max} ranges from 0.02 to 0.25 mm, depicting an increasing trend with increasing T and $H_2O_{initial}$. Under slow decompression regimes, the crystal size substantially increases due to the effect of sluggish decompression-driven crystal growth kinetics. Therefore, L_{max} measured for *ΔPs-1100-5H2O* (0.14-0.25 mm) is much higher than that determined for *ΔPf-1100-5H2O* (0.06-0.09 mm). Notably, the lack of anhedral (hopper to dendritic) forms in both *ΔPs* and *ΔPf* experiments accounts for the effect of relative slow *ΔT* (14-30 °C; Table 1), consistently with previous literature data (see the review study of Giuliani et al., 2020).

Clinopyroxene crystals from *Experimental Set CR* show substantial textural differences as a function of relaxation time (Figs. 1 and 2, and Supplementary Material 2). *CR-1050-025*, *CR-1050-05*, and *CR-1050-1* are characterized by the ubiquitous occurrence of acicular and skeletal crystals, whereas *CR-1050-4*, *CR-1050-24*, and *CR-1050-72* exhibit clear euhedral morphologies (Fig. 2 and Supplementary Material 2). The shift from a diffusion-controlled to an interface-controlled crystal growth conditions is marked, taking place in a time interval comprised between 1 and 4 h. Once crystallization proceeds under nucleation-dominated regimes, L_{max} ranges from 0.07 to 0.10 mm for *CR-1050-025*, *CR-1050-05*, and *CR-1050-1*. In contrast, due to superimposition of growth-dominated regimes, L_{max} ranges from 0.08 to 0.25 mm for *CR-1050-4*, *CR-1050-24*, and *CR-1050-72*.

3.2. Crystal content variation

Fig. 3 shows the variation of clinopyroxene content (% area) in *Experimental Set ISO*, *Experimental Set ΔP*, and *Experimental Set CR*.

As the target temperature increases, the degree of crystallization decreases from 28% to 18% and from 21% to 5% for *Experimental Set ISO* and *Experimental Set ΔP*, respectively (Fig. 3a). A similar decrease is attained by increasing $H_2O_{initial}$, whereas the crystal content slightly increases by ~4% when CO_2 is added to the experimental charge.

Experimental Set CR exhibits the highest clinopyroxene content within the whole data set. As the relaxation time increases, the degree of crystallization slightly decreases from 37% to 32% (Fig. 3b). A

modest drop in crystal content takes place in the time interval comprised between 1 and 4 h, once the crystallization regime shifts from nucleation-dominated to growth-dominated regimes.

3.3. Clinopyroxene euhedrality

Fig. 4 shows the variation of S_v^P determined for *Experimental Set ISO, Experimental Set ΔP, and Experimental Set CR*. As temperature and/or H_2O content increase, clinopyroxene S_v^P decreases with decreasing the surface area of crystals per unit volume. Moreover, the probability of phase boundary intersections increases with increasing the number of crystals, thus leading to most of trends defined for S_v^P (Fig. 4).

For *Experimental Set ISO* (730-477 mm^{-1} S_v^P) and *Experimental Set ΔP* (548-113 mm^{-1} S_v^P), the euhedrality of clinopyroxene increases with increasing temperature and $H_2O_{initial}$ (Fig. 4a). Both isothermal and decompression data confirm that values of $S_v^P < 1{,}000$ mm^{-1} account for the development of well-faced morphologies (cf. Hammer, 2008).

On the other hand, the magnitude of crystal euhedrality radically changes in *Experimental Set CR* (Fig. 4b). S_v^P ranges from 1,365 to 1,194 mm^{-1} for *CR-1050-025*, *CR-1050-05* and *CR-1050-1*. A much more restricted S_v^P range of 896-815 mm^{-1} is measured for *CR-1050-4*, *CR-1050-24*, and *CR-1050-72*. Since the experimental cooling rate was fixed and only the relaxation time was changed, the abrupt variation of S_v^P is a proxy for the control of relaxation time on the crystallization regime, after that the system is subjected to an early stage of undercooling (Arzilli et al., 2018; Pontesilli et al., 2019).

3.4. Compositional features

Chemical changes of residual glasses and coexisting clinopyroxene crystals will be the object of a forthcoming and more comprehensive work on cation partitioning under isobaric-isothermal vs. cooling-decompression conditions. Here we briefly summarize the most important compositional features of the experimental charges (Fig. 5):

1) according to the TAS (total alkali vs. silica) classification diagram, the glass chemistry (Fig. 5a) can be divided into two groups as a function of temperature and $H_2O_{initial}$ conditions (i.e., the degree of crystallization);

2) at high-*T* (1,100 °C), high-$H_2O_{initial}$ contents (5 wt.%), residual melts exhibit basaltic-trachybasaltic compositions (Fig. 5a) similar to those of recent (post-1971) eruptions at Mt. Etna volcano (natural data set from Mollo et al., 2018);

3) at low-*T* (1,050-1,075 °C), low-$H_2O_{initial}$ contents (0-2 wt.%), residual melts are more differentiated, resembling trachybasalts to basaltic trachyandesites erupted during the historic (pre-1971) period of activity (Fig. 5a);

4) clinopyroxene chemistry follows the same evolutionary path depicted by the melt phase, with the exception of sector-zoned crystals obtained under slow and fast decompression conditions (Fig. 5b);

5) at high-*T*, high- $H_2O_{initial}$ contents, clinopyroxene crystals are enriched in Di (diopside) + Hd (hedenbergite) and depleted in CaTs (Ca-Tschermak) + CaTiTs (CaTi-Tschermak) components (Fig. 5b);

6) at low-*T*, low- $H_2O_{initial}$ contents, the amount of Di + Hd in clinopyroxene crystals decreases at the expense of CaTs + CaTiTs (Fig. 5b), responding to the higher degree of melt differentiation;

7) kinetic effects in decompression experiments produce sector-zoned clinopyroxene crystals characterized by Di-Hd-rich, CaTs-CaTiTs-poor hourglass (or basal) sectors {- 1 1 1} and Di-Hd-poor, CaTs-CaTiTs-rich prism sectors {1 0 0};

8) the chemistry of hourglass sectors {- 1 1 1} closely matches with that of experimental crystals obtained at high-*T*, high-$H_2O_{initial}$ contents, as well as with the natural hourglass sectors of phenocrysts from recent eruptions at Mt. Etna volcano;

9) the chemistry of prism sectors {1 0 0} depicts a distinct crystal population, with substantial enrichment in Tschermak components, as also observed for the prism sectors of clinopyroxene phenocrysts from recent eruptions;

10) overall, the development of sector-zoned clinopyroxene crystals from decompression experiments is consistent with kinetic cation partitioning caused by decompression and degassing of Etnean magmas (Ubide and Kamber, 2018; Masotta et al., 2020), in conjunction with charge balance mechanisms due to $Si^{4+} \leftrightarrow Al^{3+}$ substitution in the tetrahedral site and $Mg^{2+} + Fe^{2+} \leftrightarrow Ti^{4+} + Fe^{3+}$ exchange in octahedral sites (Mollo et al., 2018).

4. Discussion

4.1. Clinopyroxene growth rate and thermodynamic constraints

Values of G_{max} for clinopyroxene crystals from this study are listed in Table 1 and plotted in Fig. 6 on a logarithmic scale as a function of the different experimental conditions.

For *Experimental Set ISO* and *Experimental Set ΔP*, the value of G_{max} is positively correlated with temperature and $H_2O_{initial}$, but this correlation is more evident for the decompression experiments rather than isothermal runs where G_{max} values overlap within their uncertainty (Fig. 6a). Major changes of G_{max}

411 are measured as the experimental conditions change in the order of *Experimental Set ISO* (~10^{-15}-10^{-14}
412 mm s^{-1}), *Experimental Set ΔPs* (~10^{-14}-10^{-12} mm s^{-1}), and *Experimental Set ΔPf* (~10^{-10}-10^{-9} mm s^{-1}).

413 Under isothermal conditions, the nucleation of clinopyroxene initiates when the system is heated
414 from the room temperature to the target temperature of the experiment. At nominal $\Delta T = 0$, the degree of
415 melt supersaturation is expected to be close to near-equilibrium crystallization conditions (Baker, 2008).
416 The bulk system tends to minimize the interfacial free energy between small size crystals and the
417 surrounding melt (Bonechi et al., 2020; Masotta et al., 2020), resulting in a closer approach to equilibrium
418 far from dynamic undercooling conditions encountered by magmas rising along the shallower parts of a
419 plumbing system and/or along the volcanic conduit (Mollo and Hammer, 2017 and references therein).
420 Therefore, the rate of attachment/detachment reactions of cations from the melt onto the crystalline
421 surface (and *vice versa*) approaches a steady-state condition in a relatively short experimental time
422 (Kirkpatrick, 1981, 1983; Pontesilli et al., 2019).

423 H_2O exsolution in decompression experiments raises the liquidus region of the melt, thus
424 imposing melt supersaturation (i.e., ΔT = 14-30 °C; Table 1) and facilitating the growth of clinopyroxene
425 (Simakin et al., 2003; Orlando et al., 2008; Hammer, 2008; Mollo and Hammer, 2017). Moreover, Fig.
426 6a shows that the magnitude of G_{max} from H_2O-CO_2-bearing charges (ΔT = 14-18 °C) is systematically
427 lower than that measured for H_2O-bearing charges (ΔT = 16-30 °C), accounting for the presence of CO_2
428 and its rival effect on H_2O contents dissolved in the melt. This observation is consistent with the
429 knowledge that a slow mobility of Si and Al in low-*T*, low-H_2O melts is rate-limiting for divalent Ca and
430 Mg cations, and the addition of tetrahedral groups to the surface of a crystal is the rate-controlling step
431 of the crystal growth (Nascimento et al., 2004).

432 For *Experimental Set CR*, the effect of ΔT (125 °C) on G_{max} corresponds to a large degree of melt
433 supersaturation and the crystal growth regime shifts from interface-controlled to diffusion-controlled
434 (Lofgren, 1974; Sunagawa, 1981; Webb and Dingwell, 1995). Nonetheless, as reported in Pontesilli et
435 al. (2019), relaxation kinetics control the crystal growth as a function of dwell time. G_{max} decreases by
436 orders of magnitude, from ~10^{-11} (*CR-1050-025*) to ~10^{-15} mm s^{-1} (*CR-1050-72*) (Fig. 6b). Short
437 relaxation times of 0.25-1 h favor melt supersaturation and diffusion-limited growth regimes, with more
438 pronounced nucleation of crystals showing disequilibrium textures (Mollo et al., 2010, 2012; Lofgren,
439 1974; Sunagawa, 1981). As the relaxation time increases up to 72 h, an interface-controlled growth
440 promotes formation of euhedral crystals (Fig. 6b). This textual maturation pairs with the progressive
441 decay of G_{max} towards a steady-state condition (Hammer, 2006, 2008; Pontesilli et al., 2019).

Superheating can also fundamentally alter the structure of silicate melts and variable superheating intensity can cause textural differences in subsequently nucleated crystals (First and Hammer, 2016; First et al., 2020). However, it has been also observed that the relaxation of a basaltic melt at 1,300 °C occurs in a very short time (from milli- to micro-seconds) and can be considered independent on the superheating path used in laboratory (Vetere et al., 2013, 2015).

The dependence of crystal growth rate on the degree of undercooling can be calculated as:

$$G \propto \exp\left(\frac{-E}{RT_{exp}}\right)\left[1-\exp\left(\frac{\Delta H\,\Delta T}{R\,T_{exp}\,T_{liquidus}}\right)\right] \quad (6)$$

Eqn. (6) from Armienti (2008) is the rearranged form of equations reported in Cashman (1990) and Toramaru (1991). R is the gas constant (8.310 J mol^{-1} K^{-1}), ΔH is the molar enthalpy of fusion (50-100 kJ mol^{-1}; Weill et al., 1980; Toramaru, 1991), and E is the activation energy of clinopyroxene crystal growth (200-377 kJ mol^{-1}; Toramaru, 1991; Yilmaz et al., 1996; Karamarov et al., 2000; Burkhard, 2005). T_{exp} is the experimental temperature, whereas $T_{liquidus}$ is the liquidus temperature of 1,150-1,220 °C, as determined by rhyolite-MELTS thermodynamic simulations carried out at 300 MPa, 0-5 wt.% H_2O, and NNO+2 buffer (v.1.2.0; Gualda et al., 2012). Within these thermodynamic constraints, the growth rates estimated for clinopyroxene are ~10^{-11}-10^{-9} mm s^{-1} (*Experimental Set ΔPf*), ~10^{-13}-10^{-12} mm s^{-1} (*Experimental Set ΔPs*), and ~10^{-15}-10^{-14} mm s^{-1} (*Experimental Set CR*). Fig. 6a shows that G_{max} values modeled for *Experimental Set ΔP* are comparable with those measured in laboratory, also corroborating the strong control of ΔT on clinopyroxene crystallization. However, for *Experimental Set CR*, the derived thermodynamic quantities match only with G_{max} measured for *CR-1050-24* and *CR-1050-72* experiments (Fig. 6b), whereas Eqn. (6) fails to precinct G_{max} at shorter relaxation times of 0.25, 0.5, 1, and 4 h. From a comparative textural analysis emerges that crystal growth mismatches are caused by nucleation kinetics and abundant dendritic crystallization (Fig. 2). A higher time-averaged nucleation rate over a shorter relaxation time causes a more pronounced melt supersaturation and a diffusion-controlled growth regime (Toramaru, 1991). This agrees 4D crystallization experiments conducted by Arzilli et al. (2019) on a trachybasalt erupted during 2001 eruption at Mt. Etna. It is interesting to note that, in the first part of the experiments, crystallization was induced by decreasing the temperature from superliquidus to subliquidus conditions, with a dwell time at the final temperature of 4 h. During this dwell time, blocky and prismatic clinopyroxene and oxide crystals grew. After 4 h at subliquidus condition, the temperature was further decreased to induce a continuous increase of undercooling. At ΔT

≥ 60 °C, dendritic clinopyroxene crystals developed by diffusion-controlled branching growth in multiple directions to reach a maximum size of 40 μm. Clinopyroxene nucleated heterogeneously on plagioclase and the equilibrium crystal content was achieved in ~3 min (Arzilli et al., 2019). In the present study, however, as the relaxation time increases to 24-72 h, early clinopyroxene dendritic crystals are replaced by euhedral morphologies typical of interface-controlled growth regimes (Supplementary Material 2). The attachment of cations on the crystal surface increases with increasing the relaxation time (Kirkpatrick, 1981, 1983) and euhedral morphologies are more adequately modeled by Eqn. (6) for *CR-1050-24* and *CR-1050-72* experiments (Fig. 6b).

According to clinopyroxene growth kinetics, the transition between interface-controlled and diffusion-controlled regimes is governed by a screw dislocation growth model, where the crystal-melt interface is assumed to be smooth and growth takes place at step sites provided by screw dislocations (Kirkpatrick et al., 1981, 1983). The thermodynamic equations behind screw dislocations are approximated to a temperature-dependent growth rate system (Nascimento et al., 2004):

$$G = f\,\frac{D}{\lambda}\left[1 - \exp\left(-\frac{|\Delta G|}{R\,T}\right)\right], \tag{7}$$

$$f = \frac{\lambda\,\Delta G}{4\,\pi\,\sigma\,V}, \text{ and} \tag{8}$$

$$\sigma = \frac{\alpha\,\Delta H\,\lambda}{V} \tag{9}$$

where D is the diffusion coefficient of slow diffusing Si and Al cations in the melt (~10^{-14}-10^{-15} m^2 s^{-1} at 1,050-1,100 °C; Zhang et al., 2010). λ (2.7 Å) and V (7.59 × 10^{-5} m^3 mol^{-1}) are the diameter of the diffusing building molecules and the molar volume of a pure diopside, respectively (data from Nascimento et al., 2004). ΔG is the Gibbs free energy of clinopyroxene formation estimated by rhyolite-MELTS at the experiment conditions (~7-22 kJ mol^{-1}; Gualda et al., 2012). The parameters f, σ, and α are the fraction of preferred growth sites at the crystal interface, the crystal-melt surface energy, and the reduced surface energy, respectively (cf. Nascimento et al., 2004 and references therein). The crystal growth path modeled through this approach is depicted as green (1,050 °C) and blue (1,100 °C) trends in Fig. 7. In order to isolate the effect of ΔT, the modeled trends are compared with values of G_{max} (green and blue diamonds for 1,050 and 1,100 °C, respectively) from decompression and cooling rate

experiments conducted over similar relaxation times (i.e., on the order of minutes for *ΔPf-1100-2H2O, ΔPf-1100-5H2O, ΔPf-1100-H2O+CO2, ΔPf-1050-2H2O, ΔPf-1050-5H2O, ΔPf-1050-H2O+CO2, CR-1050-0.25, CR-1050-0.5*). Small values of ΔT from *Experimental Set ΔPf* promote an interface-controlled growth (Fig. 7) and the development of large, euhedral sector-zoned crystals characterized by well-formed prismatic morphologies (Figs. 2 and 4, and Supplementary Material 2). The lack of skeletal shapes and formation of sector-zoned clinopyroxene crystals indicate sluggish crystallization kinetics typically observed at $\Delta T \leq 30$ °C (Kouchi et al., 1983; Ubide et al., 2019a; Giuliani et al., 2020; Masotta et al., 2020). Sector-zoned crystals have identical three-dimensional atomic configurations, but the surface of each individual growing sector has a specific two-dimensional atomic arrangement (Dowty, 1976 and references therein). Adjacent crystal regions grow simultaneously and form crystallographically nonequivalent faces with distinctively intersectoral chemical variations, with Di-Hd-rich, CaTs-CaTiTs-poor hourglass sectors {- 1 1 1} and Di-Hd-poor, CaTs-CaTiTs-rich prism sectors {1 0 0} (Fig. 5). These intersectoral differences emerge only under the effect of small ΔT (Kouchi et al., 1983; Masotta et al., 2020), when slow crystal growth kinetics ensure the attainment of clinopyroxene euhedrality (Fig. 4a). As a consequence, the different types of cation substitutions in the sectors reflect the variable spatial structural distributions of M and T sites as a function of the growth velocity of polyhedral sectors (Dowty, 1976 and references therein) rather than the disequilibrium advancement of a skeletal crystal surface via kinetic roughening transition (Sunagawa, 2005).

According to the above criteria, Fig. 7 displays thermodynamic modeling paths that confirm transition between interface-controlled and diffusion-controlled growth at $\Delta T \geq 30$ °C, as texturally constrained by our experimental data set. A diffusion-controlled growth regime develops only when large ΔT from *Experimental Set CR* operate in combination with short relaxation times (Fig. 7). The interface kinetics become extremely fast and tiny, anhedral clinopyroxene crystals develop from supersaturated melt regions where nucleation kinetics strongly prevail over the growth (Figs. 2 and 4b, and Supplementary Material 2). Kinetic effects due to different cation diffusivities in the melt overprint the control exercised by the structural sites of the advancing crystal surface (Giuliani et al., 2020). As a result, there is no evident control of crystal structural sites on cation incorporation and precise chemical correlations amongst the zoning patterns of skeletal clinopyroxene crystals cannot be identified (Kouchi et al., 1983; Masotta et al., 2020).

4.3 Parameterization of clinopyroxene growth kinetics

Growth rates obtained in this study are compared in Fig. 8a with those measured by previous experimental works investigating basaltic and trachybasaltic compositions that reproduce the overall intrinsic variability of rocks from the Monte Maletto Formation (Baker, 2008; Mollo et al., 2013; Pontesilli et al., 2019; Masotta et al., 2020). As pointed out by Bonechi et al. (2020), there is a strong control of melt composition on the crystal growth rate due to polymerization effects caused by an increasing number of tetrahedral sites relative to octahedral sites, thereby increasing the melt viscosity and lowering the diffusivity of elements in the melt. Accounting also for the major effects of T and H_2O on melt viscosity, all the parameterized experiments were performed at conditions analogous to those estimated for magmas erupted at Mt. Etna volcano (i.e., P = 0.1-1,000 MPa, T = 1,050-1,150 °C, H_2O = 0-4 wt.%, fO_2 = NNO+1.5-NNO+2, ΔT = 75-233 °C, and CR = 0.001-100 °C s^{-1}; see the review study of Mollo et al., 2018 and references therein). Fig. 8a shows that G_{max} decreases by approximately six orders of magnitude, from ~10^{-9} to ~10^{-15} mm s^{-1}, as the relaxation time increases from 0.08 to 72 h (Fig. 8a). Statistical calculations were carried out on the experimental data set with the Statgraphics Centurion 18® algorithm (Statpoint Technologies, Inc., Warrenton, VA, USA) by running a weighted least square (WLS) regression analysis. While in ordinary least square (OLS) regressions the standard deviation (σ) of error is assumed constant over all values of the explanatory variable, in WLS regressions the efficiency of estimation is maximized by giving to each data its proper amount of influence (i.e., weight w) over the estimate. This is especially important in modeling of logarithmic data sets that are susceptible to uncertainties associated with the linearization of the model (i.e., heteroskedasticity; Hair et al., 1995). On this basis, error minimization is attained by 1) incorporating weights into the fitting criterion and 2) performing Monte Carlo propagation of errors (Ratkowsky, 1990). The general form of WLS model is written in matrix notation as:

$$\mathbf{Y} = \mathbf{X\beta} + \boldsymbol{\varepsilon} \quad (10)$$

where $\mathbf{Y}$ = ($n \times 1$) vector of y observations, $\mathbf{X}$ = ($n \times k$) matrix of x variables, and $\boldsymbol{\beta}$ = ($k \times 1$) vector of β regression coefficients. The $\boldsymbol{\varepsilon}$ = ($n \times 1$) vector of random errors ε is expressed as ($\mathbf{0}$, $\boldsymbol{\sigma^2 W}$). In OLS, ε has mean equals to zero and variance close to the square of the standard deviation [$var(\varepsilon) = \sigma^2$]. Conversely, in WLS, ε does not have constant variance [$var(\varepsilon) = \sigma^2/w$] and the weight given to each observation is inversely proportional to the variance of the explanatory variable. $\mathbf{W}$ represents an ($n \times n$) diagonal matrix with diagonal entries corresponding to weights and $\mathbf{Var(\varepsilon)} = \mathbf{W^{-1}\sigma^2}$. The solution of Eqn. (10) is:

$$\boldsymbol{\beta}^{*} = \frac{\mathbf{X}^{\mathbf{T}}\,\mathbf{W}\,\mathbf{Y}^{*}}{\mathbf{X}^{\mathbf{T}}\,\mathbf{W}\,\mathbf{X}} \quad (11)$$

where **β*** and **Y*** are estimates of **β** and **Y**, respectively, and $\mathbf{X}^{\mathbf{T}}$ is the transpose of matrix **X**. WLS regression of experimental data displayed in Fig. 8a have the following form:

$$\ln G_{max} = \beta_0 + \beta_1 \ln t_{max} \quad (12)$$

The best predicting model for G_{max} has been calculated by optimizing the weighted fitting criterion and estimating the variance of the data set for each fixed covariate vector in Eqn. (11). This statistical approach allows to downweight outliers and reduce their impact on the overall model. The least square minimization of Eqn. (12) yields β_0 = -5.512 (±0.041 $\sigma_{\beta 0}$) and β_1 = -0.778 (±0.012 $\sigma_{\beta 1}$). The coefficient of determination (R^2), standard error of estimate (SEE_{Gmax}), and mean absolute error (ε) are 0.977, 0.242, and 0.181, respectively. As a further error test, the regression constants β_0 and β_1 have been also recalculated by perturbing Eqn. (12) via Monte Carlo simulations over a normal distribution with the mean centered on the original value of G_{max} and with deviation close to SEE_{Gmax} (Hair et al., 1995). After generating 1,000 sets of hypothetical regression coefficients, results from probability density functions confirm data from least square minimization. Therefore, it is calculated that ~68% of β_0 (Fig. 8b) and β_1 (Fig. 8c) have uncertainties of ±0.039 $\sigma_{\beta 0}$ and ±0.011 $\sigma_{\beta 1}$, respectively. Since most of the calibration data were obtained at 0 and 2 wt.% H_2O contents in both the present study and previous works, WLS regressions have been replicated on two distinct data sets for anhydrous (0 wt.% H_2O) and hydrous (2 wt.% H_2O) experiments. These calculations yield very similar regression coefficients ($^{anhydrous}\beta_0$ = -5.589 vs. $^{hydrous}\beta_0$ = -5.521, as well as $^{anhydrous}\beta_1$ = -0.771 vs. $^{hydrous}\beta_0$ = -0.778) and errors of estimate ($^{anhydrous}SEE_{Gmax}$ = 0.251 vs. $^{hydrous}SEE_{Gmax}$ = 0.244). Attainment of comparable regression coefficients points out that an increase in H_2O of 5 wt.% or an increase in temperature of 50 °C produce a similar magnitude of increase in G_{max} (Fig. 6a) and similar clinopyroxene contents (Fig. 3a). For example, at constant T, G_{max} increases by 20% as the melt-H_2O content increases from 0 to 5 wt.%. Analogously, at constant H_2O concentration, G_{max} increases by 18% as T increases from 1,050 to 1,100 °C. As previously observed by Pontesilli et al. (2019), the magnitude of G_{max} is mostly dictated by the duration of crystal growth (Fig. 6b), in concert with the increase in crystal size (L_{max}) and the clinopyroxene euhedrality (S_v^P).

Recalling the crystal size distribution (CSD) theory and Eqn. (5), the crystal nucleation rate is related to the growth rate as $J = N_0 \times G$. By assuming $G = G_{max}$ and $\tau = t_{max}$, we can substitute Eqn. (12) into the slope $m = 1 / (G \times \tau)$ of Eqn. (5) and then rearrange this algebraic expression to isolate the crystallization time of clinopyroxene forming under naturally undercooling conditions:

$$G_{\max} = t_{max}^{\beta_1} \exp\beta_0, \quad (13)$$

$$m = -\frac{1}{\left|t_{max}^{(\beta_1+1)} \exp\beta_0\right|}, \text{ and} \quad (14)$$

$$t_{max} = \left(-\frac{1}{m \exp\beta_0}\right)^{\left(\frac{1}{\beta_1+1}\right)} \quad (15)$$

The overall uncertainty associated with the estimate of t_{max} has been determined by propagating into Eqn. (15) the values of SEE_{Gmax}, $\sigma_{\beta 0}$, and $\sigma_{\beta 1}$ via Monte Carlo simulations. Density estimations indicate that the uncertainty of t_{max} varies from 22% to 28%, with an average close to 26% (Fig. 8d). The calculation of t_{max} can be performed through the Microsoft Excel spreadsheet available online as Supplementary Material 5.

4.4. Application to magma dynamics at Mt. Etna volcano

Mt. Etna is one of the most studied and monitored volcanoes in the world. The persistent eruptive activity of Mt. Etna threatens the populations living in its shadow, also causing regional climate changes in Sicily and the temporary closure of the Fontanarossa International airport of Catania. The plumbing system is governed by frequent input and mixing of primitive, volatile-rich magmas rising from a deeper (~10 km) storage region into shallower reservoirs (3-5 km) and, occasionally, ponding within the volcanic edifice (0.5-2.5 km; Patanè et al., 2003; Corsaro et al., 2009; Ubide and Kamber, 2018; Mollo et al., 2018). Abundant volatile exsolution and degassing are the key mechanisms controlling mineral and melt compositions, degree of crystallization, magma ascent velocity, and eruptive style (Armienti et al., 2007; Lanzafame et al., 2013). Magma can be erupted either quickly through deep dykes feeding eccentric eruptions (i.e., bypassing the central conduits) or gradually through the central conduits feeding shallow reservoirs (Ubide and Kamber, 2018).

A cyclic fountaining activity occurred at the New Southeast Crater (NSEC) in 2011–2012 and 2013, including normal paroxysmal sequences and energetic episodes with high eruption columns (7–8 km above the vent). A detailed multi-disciplinary data set referring to these eruptions can be found in literature, including mineral and melt compositions, volcanological constraints, thermal mapping, and structural surveys (Andronico et al., 2005; Ferlito et al., 2009, 2012; Mollo et al., 2015b, 2018; Perinelli et al., 2016; Giuffrida and Viccaro, 2017; Giuffrida et al., 2018; Giacomoni et al., 2018). In this study, we focus on clinopyroxene microphenocrysts and microlites from fourteen 2011-2012 scoria clasts that are representative of 12/01/2011, 18/02/2011, 10/04/2011, 12/05/2011, 30/07/2011, 20/08/2011, 29/08/2011, 08/09/2011, 15/11/2011, 05/01/2012, 04/03/2012, 18/03/2012, 01/04/2012, and 24/04/2012 lava fountains (Supplementary Material 3). These samples have variable vesicularity (15-30%) and porphyritic index (30-60%), but a uniform phase assemblage of olivine + clinopyroxene + plagioclase + titanomagnetite + glass (see Supplementary Material 3 and Giacomoni et al., 2018 for a detailed petrographic description). By analyzing cation redistributions in 2011-2012 clinopyroxene and titanomagnetite crystals, Mollo et al. (2015b) documented the ability of microphenocrysts and microlites to record variable undercooling histories between the sub-liquidus temperature of the magmatic reservoir and the closure temperature of crystal growth, when the kinetics and energetics of solidification were rapidly frozen-in at the time of eruption.

The saturation conditions of clinopyroxene crystals from 2011-2012 lava fountains, prior to dynamic ascent of magma towards the surface, have been estimated in this study through the integrated *P*-*T*-H_2O model of Mollo et al. (2018) specifically designed to Etnean minerals and their host magmas (Supplementary Material 4). The model uncertainty is minimized by adjusting the *P*-*T*-H_2O estimates within the calibration errors of the barometer (±150 MPa), thermometer (±20 °C), and hygrometer (±0.45 wt.% H_2O), in order to reduce the difference (Δ) between measured and predicted equilibrium values of $Kd_{Fe\text{-}Mg}$ (Fe-Mg exchange partition coefficient; Putirka, 2008), K_{Na} (Na partition coefficient; Blundy et al., 1995), and *DiHd* (diopside + hedenbergite; Mollo et al., 2013). These correction criteria and probability density functions are applied to microphenocryst and bulk rock compositions (Supplementary Material 4), providing the most reliable near-equilibrium conditions for clinopyroxene saturation at ~210-260 MPa (i.e., ~8-10 km, presuming a continental crust density of 2.6 g cm^{-3}; Armienti et al., 2013), ~1,070-1,080 °C, and ~2.2-2.4 wt.% H_2O (Fig. 9). Notably, the estimated pressure range matches with magma storage at an intermediate depth of 7-13 km (Murru et al., 1999) and within a major aseismic high P-wave velocity body extending down to 18 km (Aloisi et al., 2002).

Fig. 10 shows CSD curves of 2011-2012 clinopyroxene crystals, with kinked concave-up shapes and marked changes in slope, from a shallower gradient in the larger crystals to a steeper gradient in the smaller ones (Burney et al., 2020). Regression coefficients determined for microphenocrysts (m from -13.589 to -16.914 mm^{-1} and N_0 from 8.177 to 10.358 mm^{-4}) and microlites (m from -45.981 to -93.140 mm^{-1} and N_0 from 13.796 to 16.764 mm^{-4}) are characteristically different (Table 2). Coherently, the systematic kink of CSD curves attests the occurrence of distinct crystal size distributions for microphenocrysts ($L \geq 0.1$ mm) and microlites ($L < 0.1$ mm). In a few samples the kink shifts at 0.14 mm because of the higher crystallinity of the erupted products (Cashman and Marsh 1988; Higgins 1996). These kinked shape trends are generally attributed to variable crystal growth rates and undercooling histories of magmas during ascent along different portions of the plumbing system and volcanic conduit, without any gain or loss from/to external magma batches (Kirkpatrick, 1981, 1983; Maaloe et al., 1989; Armienti et al., 1994; Armienti, 2008). In this context, $N(L)$ vs. L trajectories displayed in Fig. 10 and their regression coefficients (Table 2) are principally the result of different crystallization regime upon the P-T-H_2O array experienced by dynamically erupted magmas (Armienti et al., 2013).

By applying Eqn. (15) to the slope of each CSD curve, we have quantified the growth time recorded by the textual evolution of 2011-2012 clinopyroxene crystals. Results from calculations are listed in Table 2 and return values of t_{max} ranging from ~1.4±0.3 to ~33.4±8 min and from ~50.7±13 to ~136.2±35 h for microlite and microphenocryst populations, respectively. The low magnitude of t_{max} measured for microlites testifies to fast kinetic effects and rapid crystal growth regimes, when magma acceleration within the uppermost part of the conduit leads to large ΔT (Armienti, 2008). According to this proposition, fluid mechanic mechanisms governing magma ascent indicate that, upon abundant volatile exsolution within a narrow degassing path, the volume expansion of magma by the growth of gas bubbles is balanced by an increasing acceleration towards the surface (Gonnermann and Manga, 2013). Conversely, the high magnitude of t_{max} derived for microphenocrysts indicates sluggish kinetic effects associated with small ΔT and slow crystal growth regimes from more relaxed melts. Evidently, at greater depths and within the plumbing system of Mt. Etna volcano, clinopyroxene microphenocrysts have more time to grow and equilibrate with the melt under steady-state conditions (Armienti et al., 2013).

We emphasize that values of t_{max} are intrinsically related to the kinetic aspects and thermodynamics of clinopyroxene growth. Therefore, caution should be exercised in comparing the magnitude of t_{max} with the time scale of magma dynamics derived by numerical modeling of volcanic conduit processes (e.g., La Spina et al., 2016, 2021; Polacci et al., 2019) and/or time scales from

688 elemental diffusion (e.g., Giuffrida et al., 2018; Ubide and Kamber, 2018). The corollary is that the
689 crystal growth will never occur when a full thermodynamic equilibrium (i.e., a minimum energy state)
690 is achieved throughout the crystal-melt interface. There is an energy barrier to overcome in order to
691 promote imbalance between the attachment and detachment energies of cations at the crystal-melt
692 interface. This excess energy is attained by melt supersaturation, when the thermodynamic driving force
693 is higher than a critical threshold above which crystal growth takes place (Sunagawa, 2005). At large ΔT,
694 such as those typically occurring during rapid ascent of magma within a volcanic conduit, the effective
695 mechanism controlling clinopyroxene growth rate depends on the slow diffusivity of Si and Al in the
696 melt with respect to Ca and Mg. The addition of network-former species to the growing surface of crystals
697 is the rate-controlling step for the textural maturation of clinopyroxene (Mollo and Hammer, 2017).
698 Moreover, since the strength of the ^{T}Al–O bonds in the melt is weaker than that of ^{T}Si–O bonds
699 (Kirkpatrick, 1983), the transfer rate of incompatible cations (i.e., Al + Ti) from the melt to the crystal
700 surface is much more facilitated than that of compatible elements (i.e., Ca + Mg; Mollo et al., 2010,
701 2012(a o b); Pontesilli et al., 2019; Masotta et al., 2020). According to these kinetic principles, G_{max} and
702 t_{max} are inextricably interrelated to the morphological stability of the crystal-melt interface throughout
703 the growth process (Sunagawa, 2005). The crystal-melt interface is the locus where growth or dissolution
704 take place upon dynamic changes of P-T-H_2O during magma ascent towards the surface and upon
705 decompression-cooling paths. Melt supersaturation causes morphological instability of the crystal and
706 shifts from polyhedral to hopper to dendritic forms, by imposing temperature and concentration gradients
707 at the interface (Sunagawa, 2005).

708 According to the above considerations, the magnitude of G_{max} and t_{max} mostly depends on 1)
709 morphological instability as a function of attachment/detachment energies of cations with increasing ΔT
710 and 2) concentration gradients in the melt next to the advancing crystal surface and disequilibrium uptake
711 of incompatible cations within the lattice site (Pontesilli et al., 2019; Masotta et al., 2020). However, it
712 is interesting to note that values of t_{max} (~1-41 min; Table 2) measured for 2011-2012 clinopyroxene
713 microlites are consistent with the numerical analysis of magma ascent times of 1995–2019 eruptions at
714 Mt. Etna (Polacci et al., 2019). The 1995–2019 explosive activity produced, among other products,
715 significant ash emissions. The numerical analysis was performed by considering volcanic conduits with
716 either cylindrical or dyke geometries, yielding ascent time minimum (~2.5 min) at the center of the
717 conduit and maximum (~25 min) at the conduit walls, corresponding to ~1% of the total magma rising
718 within the conduit (Polacci et al., 2019). Similarly, the estimated ascent time of magma within a dyke
719 ranges from ~3.3 min to ~33 min, corresponding to less than 0.4% of the total magma (Polacci et al.,

2019). According to La Spina et al. (2021), lava fountaining at Mt. Etna consists of an eruptive style distinct from effusive and explosive eruptions, as the result of rapid magma ascent with most of fragmentation above the vent rather than within the conduit. Magma ascent times of ~40 min determined by La Spina et al. (2021) are in the same order of magnitude of t_{max} calculated for some 2011-2012 microlites and microphenocrysts from this study.

A conceptual model of open conduit dynamics at Mt. Etna is schematized in Fig. 11. Most of the clinopyroxene microlite crystallization occurs within the uppermost segment of the volcanic conduit under the effect of large ΔT and short t_{max} (Fig. 11). This short time is also comparable with that (< 60 min) estimated for plagioclase during dynamic ascent of magma and under strong disequilibrium conditions driven by abundant volatile exsolution (La Spina et al., 2016). *In-situ* experiments carried out on a typical Etnean trachybasalt reveal that ΔT = 60-140 °C drive exceptionally rapid crystallization of plagioclase and clinopyroxene microlites in several minutes, also inducing a step change in viscosity that may trigger magma fragmentation (Arzilli et al., 2019). Moreover, because of rapid fractionation of lithium between melt and fluid during magma degassing, the decrease in Li concentration in plagioclase by diffusion corresponds to magma ascent time scales variable from 0.2 to 3 min for paroxysmal sequences (Giuffrida et al., 2018). This syn-eruptive stage of magma is outlined by t_{max} of ~1-3 min calculated for 2011-2012 clinopyroxene microlites (Fig. 11), as well as by rapid decompression (12 MPa min^{-1}) and cooling experiments (12 °C min^{-1}) of Arzilli et al. (2019) showing that abundant clinopyroxene microlite crystallization occurs in only 5 min at ΔT > 100 °C. Considering that most of the disequilibrium crystallization takes place at ~1.5 km below the vent (cf. La Spina et al., 2016, 2021), we derive maximum magma ascent rates of ~1-23 m s^{-1} considering the model error (Table 2 and Fig. 11). These estimates are statistically comparable with syn-eruptive ascent rates of ~3 m s^{-1} determined for mild lava fountaining activity at Mt. Etna, Stromboli, and Kilauea (La Spina et al., 2016, 2021), as well as for syn-eruptive ascent rates measured for shallow subvolcanic magma storage zones (depth ≤10 km) feeding more silicic explosive eruptions worldwide (~0.5-50 m s^{-1}; Cassidy et al., 2018).

Notably, the compositional difference between the initial melt and the final three-dimensional structural arrangement of the crystal requires that stable nuclei can form only when the local configuration of molecular units attains a critical cluster radius (e.g., Vetere et al., 2015 and references therein). As the microlite crystallization increases during ascent of magma within the conduit, the residual melt composition becomes progressively more differentiated (i.e., SiO_2-Na_2O-rich and CaO-MgO-poor) favoring the enlargement of plagioclase stability field (i.e., albite end-member) at the expense of clinopyroxene (i.e., diopside end-member). For this reason, at ΔT > 100 °C, the growth

752 kinetics of 2011-2012 clinopyroxene microlites does not return magma ascent rates > 23 m s^{-1} (Fig. 11),
753 such as those also measured at Mt. Etna that are related to strong degassing processes governing Li
754 diffusion in plagioclase (~43 m s^{-1}; Giuffrida et al., 2018) and further magma acceleration at the vent
755 (~75 m s^{-1}; La Spina et al., 2021).
756 Differently from shallow conduit and vent dynamics, values of t_{max} (~38-171 h; Table 2)
757 calculated for 2011-2012 clinopyroxene microphenocrysts are orders of magnitude greater than the very
758 fast crystallization history recorded by microlites. Evidently, the growth of microphenocrysts does not
759 represent the timing of eruption within the upper conduit or immediately before ejection from the vent,
760 where large degrees of supersaturation are driven by fast cooling, decompression, and degassing of
761 magma (Fig. 11). Rather, most of microphenocryst growth is governed by a small ΔT and long t_{max} at
762 depth (Fig. 11), where crystallization kinetics are slow and the crystal surface has enough time to develop
763 polyhedral morphology (Armienti et al., 2013). Moreover, there is no systematic change of t_{max} with the
764 1) 2011-2012 paroxysmal phase duration, 2) Strombolian activity preceding lava fountaining, and 3)
765 associated seismic signals or volcanic tremors (data from the multidisciplinary reports of the INGV
766 Osservatorio Etneo available at www.ct.ingv.it). This suggests that the onset of microphenocryst growth
767 takes place at the early saturation condition of clinopyroxene and under a near-equilibrium crystallization
768 state corresponding to the main storage region of magma at ~8-10 km of depth. It is also not excluded
769 that microphenocryst crystallization continues via open system processes governed by the invasion of
770 the plumbing system with fresh magma (Fig. 11). Time scales from this study closely match with those
771 (~17-168 h) derived by Ubide and Kamber (2018) for the development of Cr zoning in clinopyroxene
772 caused by continuous magma recharge and mixing events at depth of ~10 km (Fig. 11). Under such
773 conditions, both volatile exsolution and crystallization are low, bubble expansion and magma buoyancy
774 are limited, and the slow upward migration of magma provides more time for mineral-melt-fluid
775 equilibration (e.g., Cassidy et al., 2018). Ubide and Kamber (2018) estimated magma ascent rates of
776 0.02-0.17 m s^{-1} that are analogous to those (0.02-0.07 m s^{-1}; Table 2) determined for the growth of 2011-
777 2012 clinopyroxene microphenocrysts. Therefore, differently from the fast acceleration of magma within
778 the conduit, open system dynamics at depth require longer time periods for the migration of magma
779 through interconnected storage regions (Fig. 11). This conclusion is supported by similar estimates
780 obtained through different methodologies based on cation redistributions in minerals (0.01-0.31 m s^{-1};
781 Mollo et al., 2015b) and geophysical signals (0.04-0.4 m s^{-1}; Aloisi et al., 2006) at Mt. Etna volcano, as
782 well as by authors investigating other volcanic settings worldwide, such as Hawaii (0.01–0.04 m s^{-1};

Rutherford, 2008; Gonnermann and Manga, 2013), Unzen (0.01–0.07 m s^{-1}; Toramaru et al., 2008) and Mount St. Helens (0.01–0.15 m s^{-1}; Rutherford and Hill, 1993).

5. Conclusions

Clinopyroxene growth kinetics have been experimentally investigated and parameterized under a broad range of isothermal-isobaric, decompression, and cooling rate conditions, representative of variable crystallization conditions at Mt. Etna volcano. Through this approach, the following main conclusions can be drawn:

1) the texture of clinopyroxene is greatly controlled by melt supersaturation (i.e., undercooling) and relaxation time resulting from *P*-*T*-H_2O changes;
2) crystal euhedrality is maintained either under substantially subliquidus isothermal-isobaric or slow-to-fast decompression conditions, with the main difference represented by the development of sector-zoned clinopyroxene crystals during melt decompression;
3) as the relaxation time increases, the crystal growth rate radically decreases, whereas the crystal euhedrality increases;
4) thermodynamic modeling suggests that the transition between interface-controlled and diffusion-controlled growth arises at undercooling higher than 30 °C;
5) below this threshold value, sluggish crystallization kinetics lead to the formation of sector-zoned clinopyroxene crystals, with Di-Hd-rich, CaTs-CaTiTs-poor hourglass sectors {- 1 1 1} and Di-Hd-poor, CaTs-CaTiTs-rich prism sectors {1 0 0} typically observed at Mt. Etna volcano;
6) by integrating experimental textural data and the algebraic expression of crystal size distribution (CSD), the crystallization time of clinopyroxene can be parameterized as a function of growth rate;
7) for the case of 2011-2012 lava fountains, results from calculations return time scales variable from ~10^0-10^1 min and ~10^1-10^2 h for microlite and microphenocryst populations, respectively;
8) while shorter time scales of microlites testify to fast kinetic effects due to large undercoolings during magma acceleration in the uppermost part of the volcanic conduit, longer time scales of microphenocrysts are associated with near-equilibrium crystallization due to small undercoolings at depth;
9) we conclude that fast ascent rates of magmas (~10^0-10^1 m s^{-1}) lead to disequilibrium growth of microlites and supersaturation (i.e., undercooling) effects due to strong degassing and cooling before eruption from the vent. In contrast, slow ascent rates of magmas (~10^{-2} m s^{-1}) favor near-

equilibrium crystallization of microphenocrysts over longer time periods and within the interconnected storage regions that characterize the plumbing system architecture of Mt. Etna volcano.

Acknowledgments

The authors would like to thank Alessandro Vona and Alessio Pontesilli for their kind help with crystal size distribution (CSD) analysis. This work has been greatly improved by the helpful and thoughtful reviews of Fabio Arzilli and Emily First. Michael Roden is also acknowledged for his valuable editorial guidance.

References

Aloisi, M., Cocina, O., Neri, G., Orecchio, B., Privitera, E., 2002. Seismic tomography of the crust underneath the Etna volcano, Sicily. Phys. Earth Planet. Inter. 134, 139–155.

Aloisi, M., Bonaccorso, A., Gambino, S., 2006. Imaging composite dike propagation (Etna, 2002 case). J. Geophys. Res. 111.

Andronico, D., Branca, S., Calvari, S., Burton, M., Caltabiano, T., Corsaro, R.A., Del Carlo, P., Garfì, G., Lodato, L., Miraglia, L., Murè, F., Neri, M., Pecora, E., Pompilio, M., Salerno, G., Spampinato, L., 2005. A multi-disciplinary study of the 2002-03 Etna eruption: insights into a complex plumbing system. Bull Volcanol 67, 314–330.

Armienti, P., Pareschi, M.T., Innocenti, F., Pompilio, M., 1994. Effects of magma storage and ascent on the kinetics of crystal growth. Contr. Mineral. and Petrol. 115, 402–414.

Armienti, P., Francalanci, L., Landi, P., 2007. Textural effects of steady state behaviour of the Stromboli feeding system. J. Volcanol. Geotherm. Res. 160, 86–98.

Armienti, P., 2008. Decryption of Igneous Rock Textures: Crystal Size Distribution Tools. Rev Mineral Geochem 69, 623–649.

Armienti, P., Perinelli, C., Putirka, K.D., 2013. A New Model to Estimate Deep-level Magma Ascent Rates, with Applications to Mt. Etna (Sicily, Italy). J. Petrol. 54, 795–813.

Arzilli, F., Fabbrizio, A., Schmidt, M.W., Petrelli, M., Maimaiti, M., Dingwell, D.B., Paris, E., Burton, M., Carroll, M.R., 2018. The effect of diffusive re-equilibration time on trace element partitioning between alkali feldspar and trachytic melts. Chem. Geol. 495, 50–66.

Arzilli, F., La Spina, G., Burton, M.R., Polacci, M., Le Gall, N., Hartley, M.E., Di Genova, D., Cai, B., Vo, N.T., Bamber, E.C., Nonni, S., Atwood, R., Llewellin, E.W., Brooker, R.A., Mader, H.M., Lee,

P.D., 2019. Magma fragmentation in highly explosive basaltic eruptions induced by rapid crystallization. Nat. Geosci. 12, 1023–1028.

Baker, D.R., 2008. The fidelity of melt inclusions as records of melt composition. Contrib Mineral Petrol 156, 377–395.

Blundy, J.D., Falloon, T.J., Wood, B.J., Dalton, J.A., 1995. Sodium partitioning between clinopyroxene and silicate melts. J. Geophys. Res. Solid Earth 100, 15501–15515.

Bonechi, B., Perinelli, C., Gaeta, M. Clinopyroxene growth rates at high pressure: constraints on magma recharge of the deep reservoir of the Campi Flegrei Volcanic District (south Italy). Bull Volcanol 82, 5.

Botcharnikov, R.E., Almeev, R.R., Koepke, J., Holtz, F., 2008. Phase Relations and Liquid Lines of Descent in Hydrous Ferrobasalt--Implications for the Skaergaard Intrusion and Columbia River Flood Basalts. J. Petrol. 49, 1687–1727.

Burkhard, D.J.M., 2005. Nucleation and growth rates of pyroxene, plagioclase, and Fe-Ti oxides in basalt under atmospheric conditions. European Journal of Mineralogy 17, 675–686.

Burney, D., Peate, D.W., Riishuus, M.S., Ukstins, I.A., 2020. Reconstructing the plumbing system of an off-rift primitive alkaline tuya (Vatnafell, Iceland) using geothermobarometry and CSDs. J. Volcanol. Geotherm. Res. 399, 106914.

Cashman, K.V., Marsh, B.D., 1988. Crystal size distribution (CSD) in rocks and the kinetics and dynamics of crystallization II: Makaopuhi lava lake. Contr. Mineral. and Petrol. 99, 292–305.

Cashman, K.V., 1990. Textural constraints on the kinetics of crystallization of igneous rocks. Rev. Mineral. 24, 259–314.

Cassidy, M., Manga, M., Cashman, K., Bachmann, O., 2018. Controls on explosive-effusive volcanic eruption styles. Nat Commun 9.

Corsaro, R.A., Civetta, L., Di Renzo, V., Miraglia, L., 2009. Petrology of lavas from the 2004-2005 flank eruption of Mt. Etna, Italy: inferences on the dynamics of magma in the shallow plumbing system. Bull. Volcanol. 71, 781–793.

Di Stefano, F., Mollo, S., Ubide, T., Petrone, C.M., Caulfield, J., Scarlato, P., Nazzari, M., Andronico, D., Del Bello, E., 2020. Mush cannibalism and disruption recorded by clinopyroxene phenocrysts at Stromboli volcano: New insights from recent 2003–2017 activity. Lithos 360–361, 105440.

Dowty, E., 1976. Crystal structure and crystal growth: II. Sector zoning in minerals. Am. Mineral. 61, 460–469.

Duan, X., 2014. A general model for predicting the solubility behavior of H2O-CO2 fluids in silicate melts over a wide range of pressure, temperature and compositions. Geochim. Cosmochim. Acta 125, 582–609. http://dx.doi.org/10.1016/j.gca.2013.10.018.

Ferlito, C., Coltorti, M., Cristofolini, R., Giacomoni, P.P., 2009. The contemporaneous emission of low-K and high-K trachybasalts and the role of the NE Rift during the 2002 eruptive event, Mt. Etna, Italy. Bull Volcanol 71, 575–587.

Ferlito, C., Viccaro, M., Nicotra, E., Cristofolini, R., 2012. Regimes of magma recharge and their control on the eruptive behaviour during the period 2001–2005 at Mt. Etna volcano. Bull Volcanol 74, 533–543.

First, E.C., Leonhardi, T.C., Hammer, J.E., 2020. Effects of superheating magnitude on olivine growth. Contrib Mineral Petrol 175, 13.

First E.C., Hammer J.E., 2016. Igneous cooling history of olivine-phyric shergottite Yamato 980459 constrained by dynamic crystallization experiments. Meteorit Planet Sci. 51, 1233–1255.

Giacomoni, P.P., Coltorti, M., Mollo, S., Ferlito, C., Braiato, M., Scarlato, P., 2018. The 2011–2012 paroxysmal eruptions at Mt. Etna volcano: Insights on the vertically zoned plumbing system. J. Volcanol. Geotherm. Res. 349, 370–391.

Giordano, D., Nichols, A.R.L., Dingwell, D.B., 2005. Glass transition temperatures of natural hydrous melts: a relationship with shear viscosity and implications for the welding process. J. Volcanol. Geotherm. Res. 142, 105–118.

Giuffrida, M., Viccaro, M., 2017. Three years (2011–2013) of eruptive activity at Mt. Etna: Working modes and timescales of the modern volcano plumbing system from micro-analytical studies of crystals. Earth Sci Rev 171, 289–322.

Giuffrida, M., Viccaro, M., Ottolini, L., 2018. Ultrafast syn-eruptive degassing and ascent trigger high-energy basic eruptions. Sci Rep 8.

Giuliani, L., Iezzi, G., Vetere, F., Behrens, H., Mollo, S., Cauti, F., Ventura, G., Scarlato, P., 2020. Evolution of textures, crystal size distributions and growth rates of plagioclase, clinopyroxene and spinel crystallized at variable cooling rates from a mid-ocean ridge basaltic melt. Earth Sci Rev 204, 103165.

Gonnermann, H.M., Manga, M., 2013. Dynamics of magma ascent in the volcanic conduit. In: Fagents, S.A., Gregg, T.K.P., Lopes, R.M.C. (Eds.), Modeling Volcanic Processes. Cambridge Univ Press, pp.55–84.

Gualda, G.A., Ghiorso, M.S., Lemons, R.V., Carley, T. L., 2012. Rhyolite-MELTS: a modified calibration of MELTS optimized for silica-rich, fluid-bearing magmatic systems. J. Petrol. 53, 875–890.

Hammer, J.E., 2008. Experimental Studies of the Kinetics and Energetics of Magma Crystallization. Rev Mineral Geochem 69, 9–59.

Hammer, J.E., 2006. Influence of fO2 and cooling rate on the kinetics and energetics of Fe-rich basalt crystallization. Earth Planet. Sci. Lett. 248, 618–637.

Hammer, J., Jacob, S., Welsch, B., Hellebrand, E., Sinton, J., 2016. Clinopyroxene in postshield Haleakala ankaramite: 1. Efficacy of thermobarometry. Contrib Mineral Petrol 171.

Hair Jr., J.F., Anderson, R.E., Tatham, R.L., Black, W.C., 1995. Multivariate Data Analysis. 3rd ed. Macmillan, New York (742 pp.).

Higgins, M.D., 1996. Magma dynamics beneath Kameni volcano, Thera, Greece, as revealed by crystal size and shape measurements. J. Volcanol. Geotherm. Res. 70, 37–48.

Higgins, M.D., 2000. Measurement of crystal size distributions. Am. Mineral. 85, 1105–1116.

Iezzi, G., Mollo, S., Shaini, E., Cavallo, A., Scarlato, P., 2014. The cooling kinetics of plagioclase revealed by electron microprobe mapping. Am. Mineral. 99, 898–907.

Ishibashi, H., 2013. Spinel–melt oxygen barometry: a method and application to Cenozoic alkali basaltic magmas from the Higashi–Matsuura district, NW Kyushu, Japan. Geosci. Repts. 40, 21–32.

Karamanov, A., Pisciella, P., Pelino, M., 2000a. The crystallisation kinetics of iron rich glass in different atmospheres. J. Eur. Ceram. Soc. 20, 2233–2237.

Kirkpatrick, R.J., 1981. Kinetics of crystallization of igneous rocks. In: Lasaga, A.C., Kirkpatrick, R.J. (Eds.), Reviews in Mineralogy 8. pp. 321–395.

Kirkpatrick, R.J., 1983. Theory of nucleation in silicate melts. Am. Mineral. 68, 66–77.

Kostov, I., Kostov, R.I., 1999. Crystal Habits of Minerals. Bulgarian Academic Monographs, Sophia.

Kouchi, A., Sugawara, Y., Kashima, K., Sunagawa, I., 1983. Laboratory growth of sector zoned clinopyroxenes in the system CaMgSi2O6-CaTiAl2O6. Contrib. Mineral. Petrol. 83, 177–184.

Lanzafame, G., Mollo, S., Iezzi, G., Ferlito, C., Ventura, G., 2013. Unraveling the solidification path of a pahoehoe “cicirara” lava from Mount Etna volcano. Bull Volcanol 75.

La Spina, G., Burton, M., de’ Michieli Vitturi, M., Arzilli, F., 2016. Role of syn-eruptive plagioclase disequilibrium crystallization in basaltic magma ascent dynamics. Nat Commun 7.

La Spina, G., Arzilli, F., Llewellin, E.W., Burton, M.R., Clarke, A.B., de’ Michieli Vitturi, M., Polacci, M., Hartley, M.E., Di Genova, D., Mader, H.M., 2021. Explosivity of basaltic lava fountains is controlled by magma rheology, ascent rate and outgassing. Earth Planet. Sci. Lett. 553, 116658.

Lasaga, A.C., 1998. Kinetic Theory in the Earth Sciences. Princeton University Press, Princeton, New York.

Lofgren, G.E., 1974. An experimental study of plagioclase morphology: isothermal crystallization. Am. J. Sci. 264, 243–273.

Maaløe, S., Tumyr, O., James, D., 1989. Population density and zoning of olivine phenocrysts in tholeiites from Kauai, Hawaii. Contr. Mineral. and Petrol. 101, 176–186.

Marsh, B.D., 1988. Crystal size distribution (CSD) in rocks and the kinetics and dynamics of crystallization. Contr. Mineral. and Petrol. 99, 277–291.

Masotta, M., Pontesilli, A., Mollo, S., Armienti, P., Ubide, T., Nazzari, M., Scarlato, P., 2020. The role of undercooling during clinopyroxene growth in trachybasaltic magmas: Insights on magma decompression and cooling at Mt. Etna volcano. Geochim. Cosmochim. Acta 268, 258–276.

Mollo, S., Del Gaudio, P., Ventura, G., Iezzi, G., Scarlato, P., 2010. Dependence of clinopyroxene composition on cooling rate in basaltic magmas: implications for thermobarometry. Lithos 118, 302–312.

Mollo, S., Misiti, V., Scarlato, P., Soligo, M., 2012. The role of cooling rate in the origin of high temperature phases at the chilled margin of magmatic intrusions. Chem. Geol. 322–323, 28–46.

Mollo, S., Blundy, J.D., Iezzi, G., Scarlato, P., Langone, A., 2013. The partitioning of trace elements between clinopyroxene and trachybasaltic melt during rapid cooling and crystal growth. Contrib Mineral Petrol 166, 1633–1654.

Mollo, S., Masotta, M., 2014. Optimizing pre-eruptive temperature estimates in thermally and chemically zoned magma chambers. Chem. Geol. 368, 97–103.

Mollo, S., Giacomoni, P.P., Andronico, D., Scarlato, P., 2015a. Clinopyroxene and titanomagnetite cation redistributions at Mt. Etna volcano (Sicily, Italy): footprints of the final solidification history of lava fountains and lava flows. Chem. Geol. 406, 45–54

Mollo, S., Giacomoni, P.P., Coltorti, M., Ferlito, C., Iezzi, G., Scarlato, P., 2015b. Reconstruction of magmatic variables governing recent Etnean eruptions: constraints from mineral chemistry and P–T–fO2–H2O conditions. Lithos 212–215, 311–320.

Mollo, S., Hammer, J.E., 2017. Dynamic crystallization in magmas. In: EMU Notes in Mineralogy. 16. pp. 373–418.

Mollo, S., Blundy, J., Scarlato, P., De Cristofaro, S.P., Tecchiato, V., Di Stefano, F., Vetere, F., Holtz, F., Bachmann, O., 2018. An integrated P-T-H2O-lattice strain model to quantify the role of

clinopyroxene fractionation on REE+Y and HFSE patterns of mafic alkaline magmas: Application to eruptions at Mt. Etna. Earth Sci Rev 185, 32–56.

Morgan, D.J., Jerram, D.A., 2006. On estimating crystal shape for crystal size distribution analysis. J. Volcanol. Geotherm. Res. 154, 1–7.

Murru, M., Montuori, C., Wyss, M., Privitera, E., 1999. The locations of magma chambers at Mt. Etna, Italy, mapped by b-values. Geophys. Res. Lett. 26, 2553–2556.

Nascimento, M.L.F., Ferreira, E.B., Zanotto, E.D., 2004. Kinetics and mechanisms of crystal growth and diffusion in a glass-forming liquid. J. Chem. Phys. 121, 8924–8928.

Orlando, A., D'Orazio, M., Armienti, P., Borrini, D., 2008. Experimental determination of plagioclase and clinopyroxene crystal growth rates in an anhydrous trachybasalt from Mt Etna (Italy). European Journal of Mineralogy 20, 653–664.

Patanè, D., De Gori, P., Chiarabba, C., Bonaccorso, A., 2003. Magma Ascent and the Pressurization of Mount Etna's Volcanic System. Science 299, 2061–2063.

Perinelli, C., Mollo, S., Gaeta, M., De Cristofaro, S.P., Palladino, D.M., Armienti, P., Scarlato, P., Putirka, K.D., 2016. An improved clinopyroxene-based hygrometer for Etnean magmas and implications for eruption triggering mechanisms. Am. Mineral. 101, 2774–2777.

Perinelli, C., Mollo, S., Gaeta, M., De Cristofaro, S.P., Palladino, D.M., Scarlato, P., 2018. Impulsive supply of volatile-rich magmas in the shallow plumbing system of Mt. Etna Volcano. Minerals 8, 482.

Petrone, C.M., Bugatti, G., Braschi, E., Tommasini, S., 2016. Pre-eruptive magmatic processes re-timed using a non-isothermal approach to magma chamber dynamics. Nat Commun 7.

Petrone, C.M., Braschi, E., Francalanci, L., Casalini, M., Tommasini, S., 2018. Rapid mixing and short storage timescale in the magma dynamics of a steady-state volcano. Earth Planet. Sci. Lett. 492, 206–221.

Polacci, M., Arzilli, F., La Spina, G., Le Gall, N., Cai, B., Hartley, M.E., Di Genova, D., Vo, N.T., Nonni, S., Atwood, R.C., Llewellin, E.W., Lee, P.D., Burton, M.R., 2018. Crystallisation in basaltic magmas revealed via in situ 4D synchrotron X-ray microtomography. Sci Rep 8, 8377–8383.

Polacci, M., Andronico, D., de' Michieli Vitturi, M., Taddeucci, J., Cristaldi, A., 2019. Mechanisms of Ash Generation at Basaltic Volcanoes: The Case of Mount Etna, Italy. Front. Earth Sci. 7.

Pontesilli, A., Masotta, M., Nazzari, M., Mollo, S., Armienti, P., Scarlato, P., Brenna, M., 2019. Crystallization kinetics of clinopyroxene and titanomagnetite growing from a trachybasaltic melt: New insights from isothermal time-series experiments. Chem. Geol. 510, 113–129.

Putirka, K., 2008. Thermometers and barometers for volcanic systems. Rev. Mineral. Geochem. 69, 61–120. http://dx.doi.org/10.2138/rmg.2008.69.3.

Ratkowsky, D.A., 1990. Handbook of Non-linear Regression Models. Marcel Decker Inc., New York.

Rutherford, M.J., Hill, P.M., 1993. Magma ascent rates from amphibole breakdown: An experimental study applied to the 1980-1986 Mount St. Helens eruptions. J. Geophys. Res. 98, 19667–19685.

Rutherford, M.J., 2008. Magma Ascent Rates. Rev Mineral Geochem 69, 241–271.

Schanofski, M., Fanara, S., Schmidt, B.C., 2019. CO2–H2O solubility in K-rich phonolitic and leucititic melts. Contrib Mineral Petrol 174.

Shea, T., and Hammer, J.E., 2013. Kinetics of cooling- and decompression-induced crystallization in hydrous mafic-intermediate magmas. J. Volcanol. Geotherm. Res., 260, 127–145.

Simakin, A.G., Salova T.P., Armienti P., 2003. Kinetics of clinopyroxene growth from a hydrous hawaiite melt. Geochemistry Int. 41, 1275-1286.

Sunagawa, I., 1981. Characteristics of crystal growth in nature as seen from the morphology of mineral crystals. Bull. Mineral. 104, 81–87.

Sunagawa, I., 2005. Crystals: Growth, Morphology and Perfection. Cambridge University Press, Cambridge.

Toramaru, A., 1991. Model of nucleation and growth of crystals in cooling magmas. Contr. Mineral. and Petrol. 108, 106–117.

Toramaru, A., Noguchi, S., Oyoshihara, S., Tsune, A., 2008. MND(microlite number density) water exsolution rate meter. J. Volcanol. Geotherm. Res. 175, 156–167.

Ubide, T., Kamber, B.S., 2018. Volcanic crystals as time capsules of eruption history. Nat Commun 9.

Ubide, T., Mollo, S., Zhao, J., Nazzari, M., Scarlato, P., 2019a. Sector-zoned clinopyroxene as a recorder of magma history, eruption triggers, and ascent rates. Geochim. Cosmochim. Acta 251, 265–283.

Ubide, T., Caulfield, J., Brandt, C., Bussweiler, Y., Mollo, S., Di Stefano, F., Nazzari, M., Scarlato, P., 2019b. Deep Magma Storage Revealed by Multi-Method Elemental Mapping of Clinopyroxene Megacrysts at Stromboli Volcano. Front. Earth Sci. 7.

Vetere, F., Iezzi, G., Behrens, H., Holtz, F., Ventura, G., Misiti, V., Cavallo, A., Mollo, S., Dietrich, M., 2015. Glass forming ability and crystallization behavior of sub-alkaline silicate melts. Earth Sci Rev 150, 25–44.

Vetere, F., Iezzi, G., Behrens, H., Cavallo, A., Misiti, V., Dietrich, M., Knipping, J., Ventura, G., Mollo, S., 2013. Intrinsic solidification behaviour of basaltic to rhyolitic melts: a cooling rate experimental study. Chem. Geol. 354, 233–242.

Webb, S.L., Dingwell, D.B., 1995. Viscoelasticity. Rev. Mineral. Geochem. 32, 95–119.

Weill, D.E., Hon, R., Navrotsky, A., 1980. The igneous system CaMgSi2O6-CaAlaSi2O6-NaAlSi3O6: variations on a classic theme by Bowen. In: Hargraves RB (ed) Physics of magmatic processes. Princeton University Press, Princeton, pp 49-92

Welsch, B., Hammer, J., Baronnet, A., Jacob, S., Hellebrand, E., Sinton, J., 2016. Clinopyroxene in postshield Haleakala ankaramite: 2. Texture, compositional zoning and supersaturation in the magma. Contrib. Mineral. Petrol. 171, 6.

Yilmaz, S., Özkan, O.T., Günay, V., 1996. Crystallization kinetics of basalt glass. Ceram. Int. 22, 477–481.

Zhang, Y., Ni, H., Chen, Y., 2010. Diffusion data in silicate melts. Rev. Mineral. Geochem. 72, 311–408.

Figure captions

Figure 1. Example of BSE (back-scattered electron) photomicrographs processed via NIH Image J software and reduced to binary type images (i.e., black vs. white color) by grey level thresholding (i.e., image segmentation; Armienti, 2008). A Matlab© code is also reported in Supplementary Material 1 to perform image processing operations in conjunction with NIH Image J. The retrieved textural parameters are 1) the equal-area best-fit ellipses and lengths of major (L) and minor (W) axes, 2) the surface area per unit volume, and 3) the area fraction of a given population within a plane that is comparable to its volume fraction. Bright BSE intensity phases refer to titanomagnetite crystals.

Figure 2. Selected BSE (back-scattered electron) photomicrographs representative of run products from *Experimental Set ISO*, *Experimental Set ΔP*, and *Experimental Set CR*. Bright BSE intensity phases refer to titanomagnetite crystals.

Figure 3. Variation of clinopyroxene content (% area) as a function of experimental conditions. Data refer to *Experimental Set ISO* and *Experimental Set ΔP* (a), and *Experimental Set CR* (b). Error bars refer to the uncertainties reported in Table 1.

Figure 4. Variation of 3D aspect ratio (S_v^P) as a function of experimental conditions. Data refer to *Experimental Set ISO* and *Experimental Set ΔP* (a), and *Experimental Set CR* (b). Error bars refer to the uncertainties reported in Table 1.

Figure 5. Total alkali *versus* silica (a) and Di + Hd *versus* CaTs + CaTiTs (b) diagrams showing experimental glass and clinopyroxene compositions, respectively. Natural compositions from eruptions at Mt. Etna volcano are also displayed for comparison.

Figure 6. Variation of $\ln G_{max}$ as a function of experimental conditions. Data refer to *Experimental Set ISO* and *Experimental Set ΔP* (a), and *Experimental Set CR* (b). Values of G_{max} modeled through the thermodynamic expression of crystal growth (cf. Armienti, 2008) are also displayed for comparison. According to Eqn. (6) reported in the text, thermodynamic data can be calculated for $\Delta T \geq 0$. Error bars refer to the uncertainties reported in Table 1.

Figure 7. Thermodynamic modeling of crystal growth kinetics for the transition between interface-controlled and diffusion-controlled growth regimes arising at undercooling higher than 30 °C. Modeled trends are depicted in green and blue for temperatures of 1,050 and 1,100 °C, respectively. In order to isolate the effect of ΔT, modeled trends are also compared with values of G_{max} (green and blue diamonds for 1,050 and 1,100 °C, respectively) from decompression and cooling rate experiments conducted over similar relaxation times (i.e., in the order of minutes for *ΔPf-1100-2H2O, ΔPf-1100-5H2O, ΔPf-1100-H2O+CO2, ΔPf-1050-2H2O, ΔPf-1050-5H2O, ΔPf-1050-H2O+CO2, CR-1050-0.25, CR-1050-0.5*).

Figure 8. Regression plot of maximum growth rate (G_{max}) *versus* experimental time (t) on a logarithmic scale (a). Data from this study are compared with those from previous experimental works investigating basaltic and trachybasaltic compositions that virtually reproduce the overall intrinsic variability of Monte Maletto Formation. Experiments were performed at conditions comparable with those of magmas erupted at Mt. Etna volcano (i.e., P = 0.1-1,000 MPa, T = 1,050-1,150 °C, H_2O = 0-4 wt.%, fO_2 = NNO+1.5-

NNO+2, ΔT = 75-233 °C, and CR = 0.001-100 °C s^{-1}; Baker, 2008; Mollo et al., 2013; Pontesilli et al., 2019; Masotta et al., 2020). Probability density functions of regression coefficients β_0 (b) and β_1 (c) obtained from Monte Carlo simulations, as well model uncertainty associated with the estimate of t_{max} (d) are also displayed.

Figure 9. Saturation conditions calculated for clinopyroxene crystals from 2011-2012 lava fountains erupted at Mt. Etna volcano. Uncorrected equilibrium between microphenocryst and bulk rock compositions has been determined for values of $Kd_{Fe\text{-}Mg}$ (Fe-Mg exchange partition coefficient; Putirka, 2008), K_{Na} (Na partition coefficient; Blundy et al., 1995), and *DiHd* (diopside + hedenbergite; Mollo et al., 2013). The equilibrium state of the bulk system has been corrected by minimizing the difference (Δ) between measured and predicted values. Using the model of Mollo et al. (2018), *P*-*T*-H_2O estimates have been adjusted within the calibration errors of the barometer (±150 MPa), thermometer (±20 °C), and hygrometer (±0.45 wt.% H_2O), in order to minimize the overall uncertainty.

Figure 10. Crystal size distribution (CSD) analysis of clinopyroxene crystals from 2011-2012 lava fountains erupted at Mt. Etna volcano. *N(L) versus L* curves attest the occurrence of two distinct microphenocryst and microlite populations.

Figure 11. Conceptual model of magma dynamics at Mt. Etna volcano describing the different time scales estimated for microlite and microphenocryst crystallization. Magma ascent velocities are also modeled accounting for either slow magma ascent rates within the interconnected storage regions forming the plumbing system architecture at depth or fast magma ascent rates within the uppermost part of the volcanic conduit and before eruption at the vent.

Figure 1

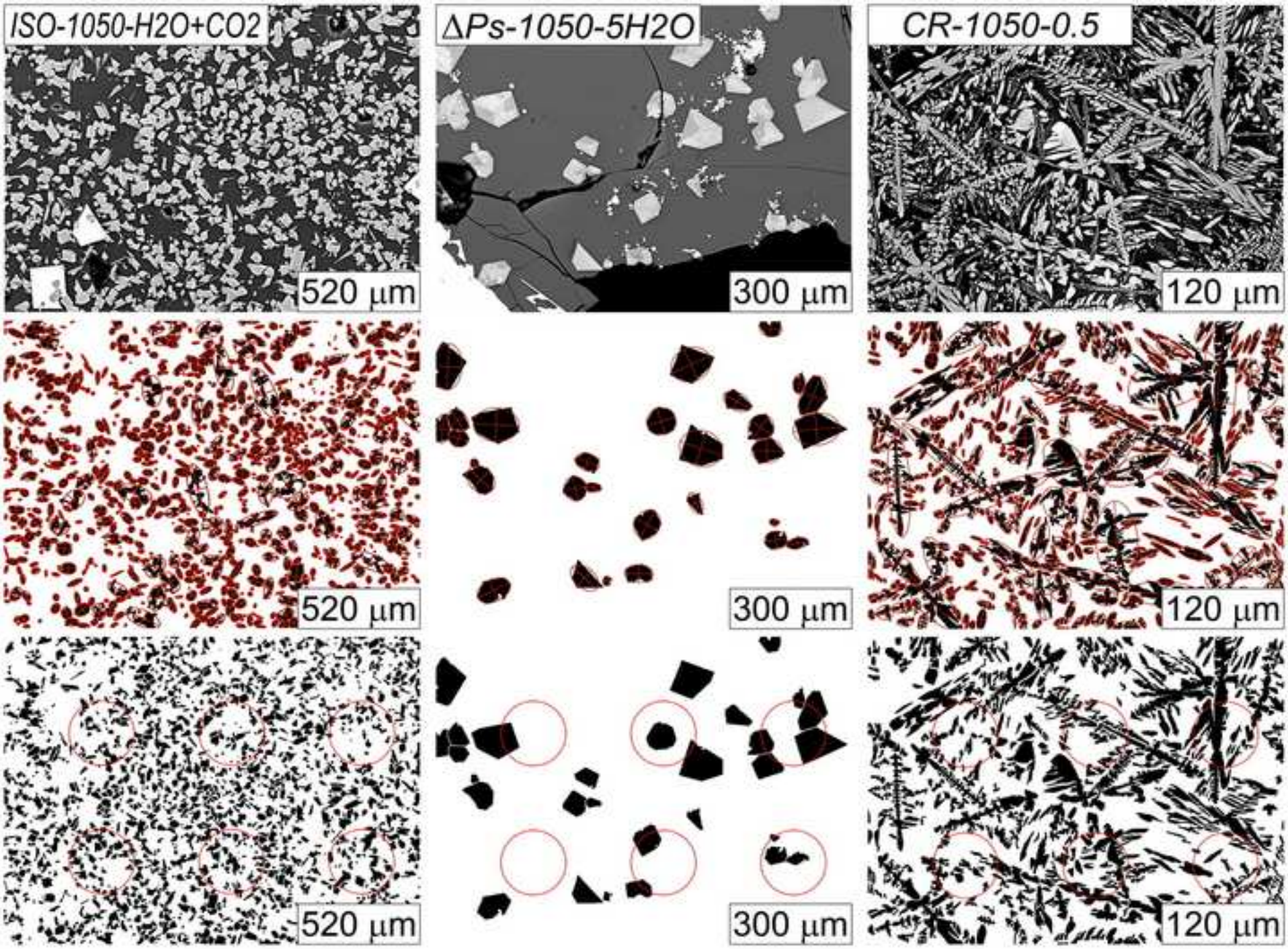

Figure 2

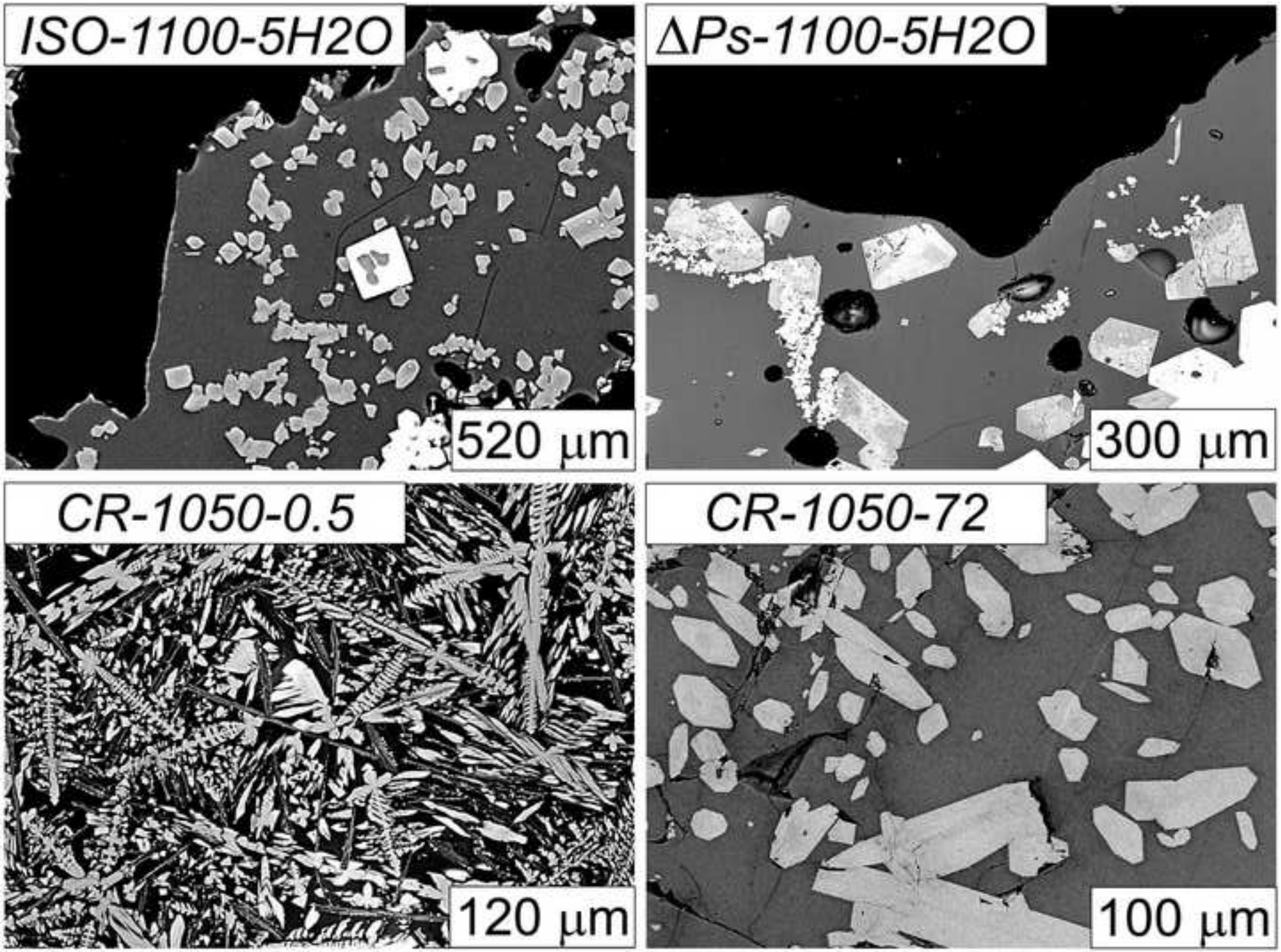

Figure 3

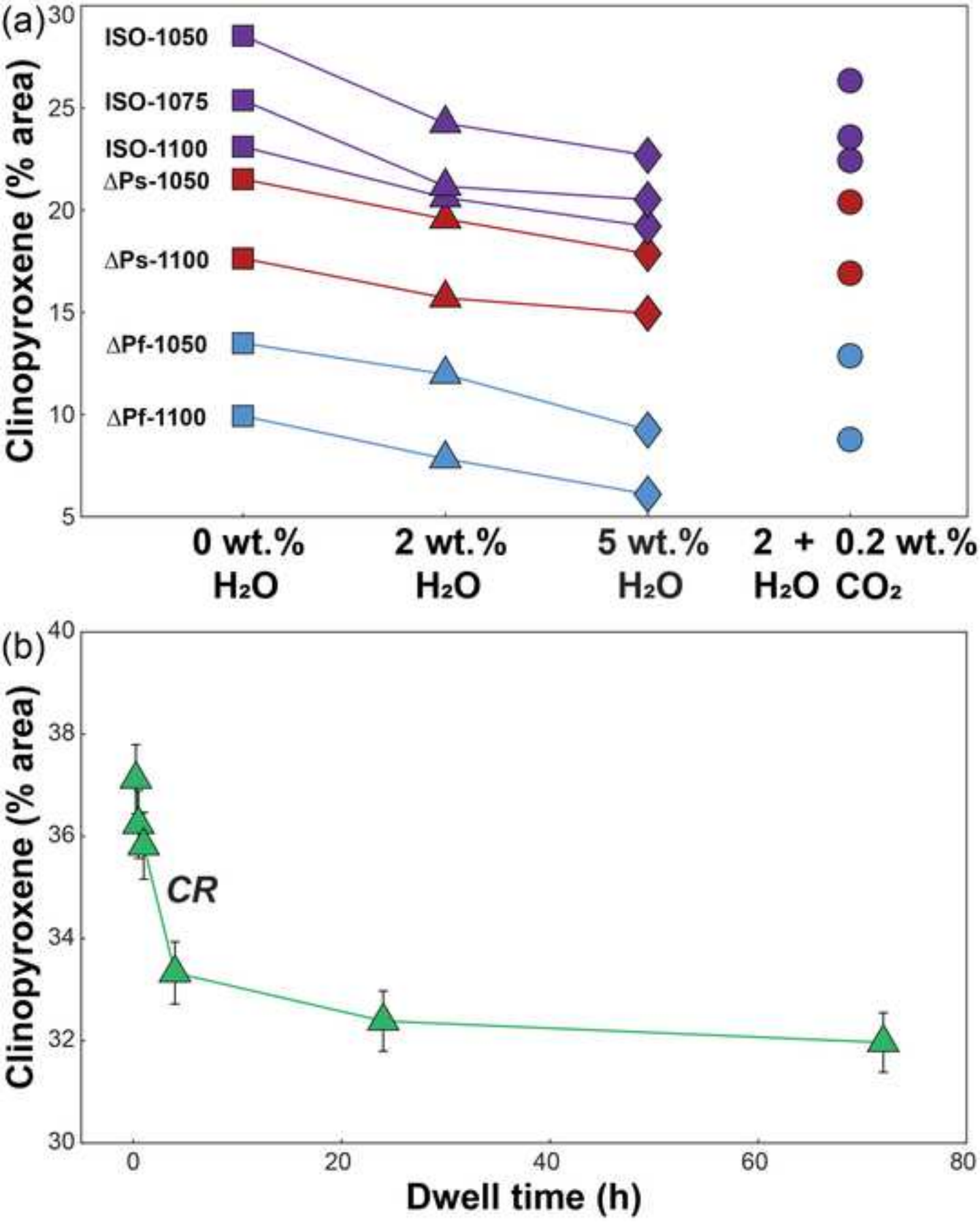

Figure 4

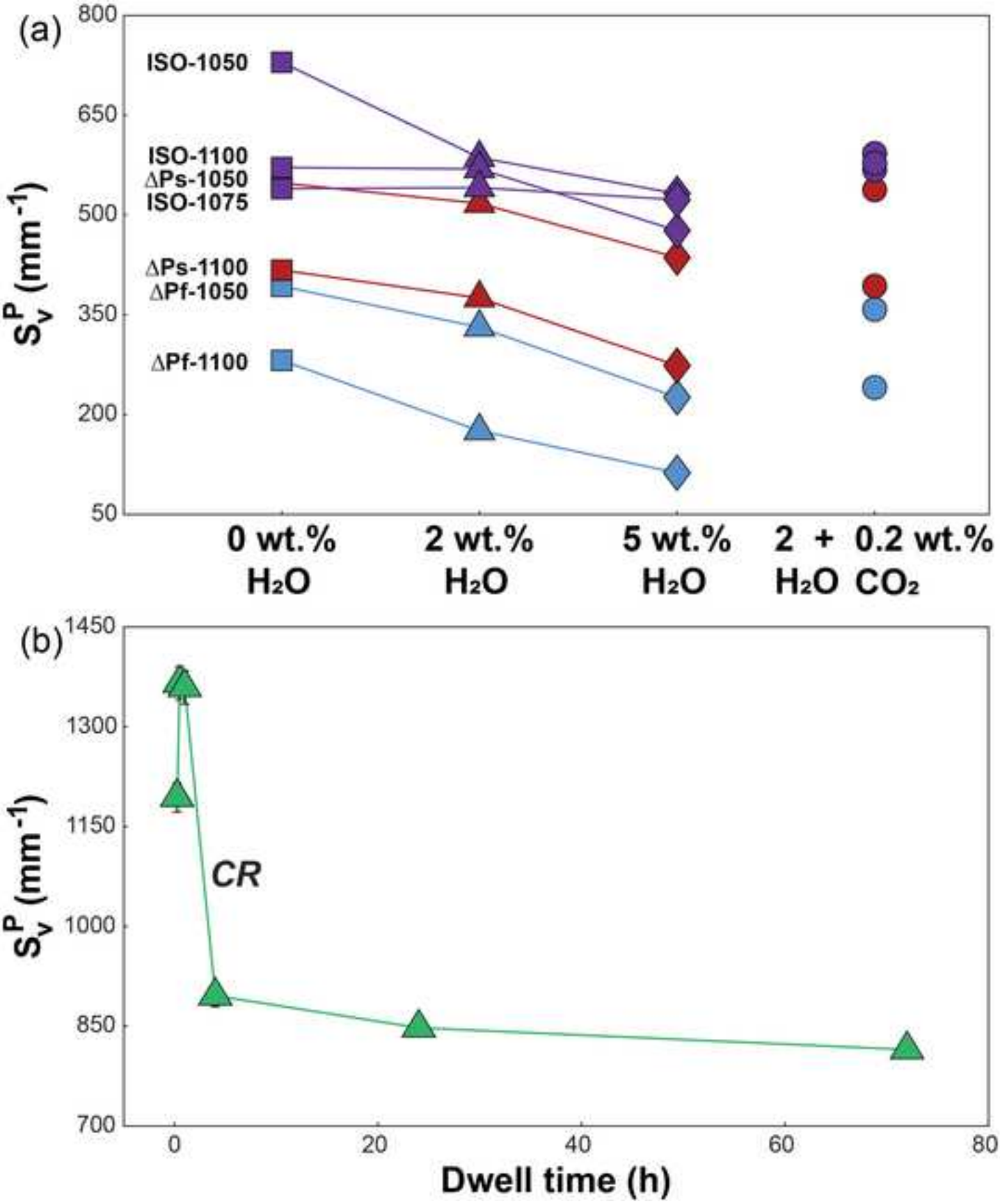

Figure 5

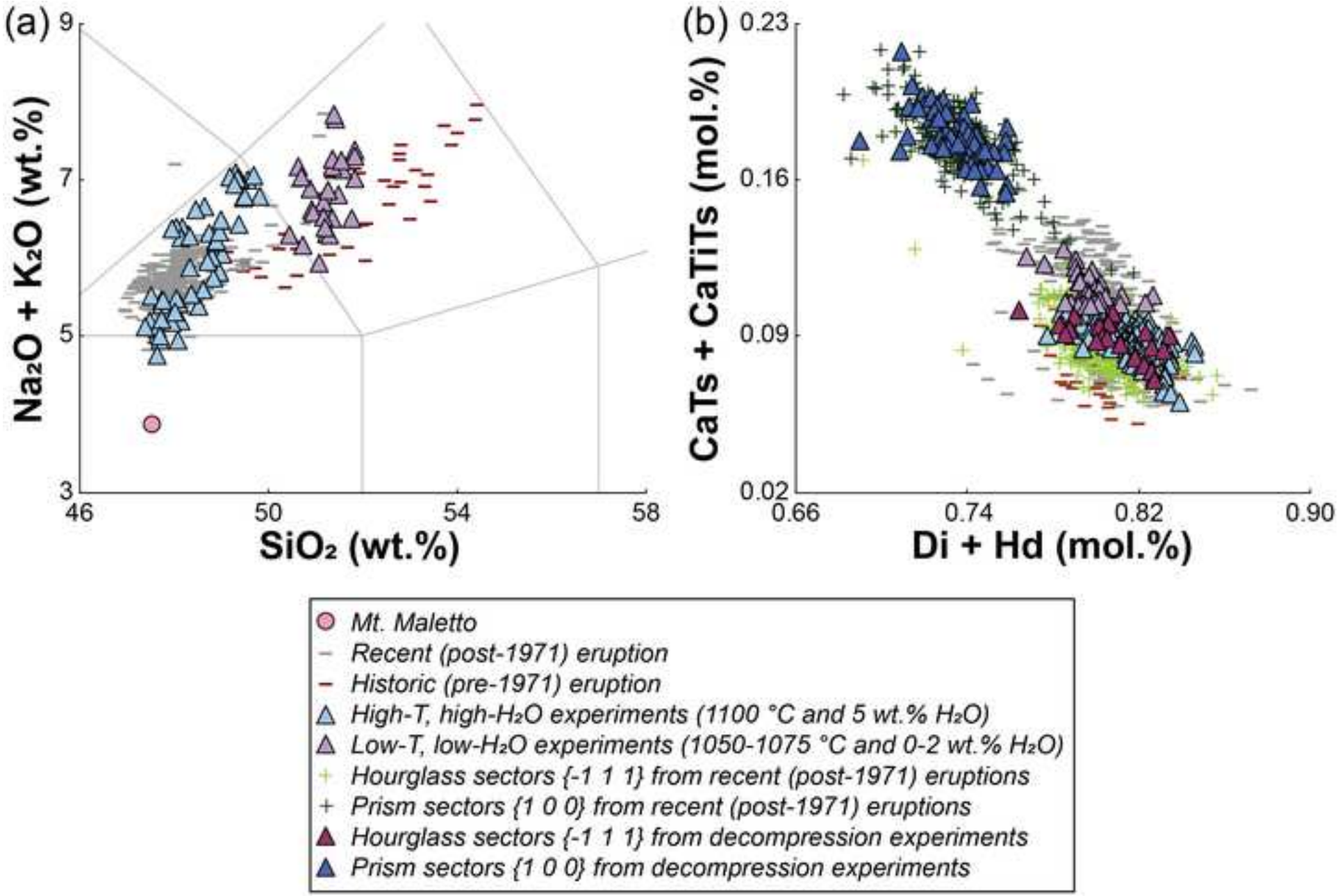

Figure 6

Click here to access/download;Figure;Fig.06.jpg

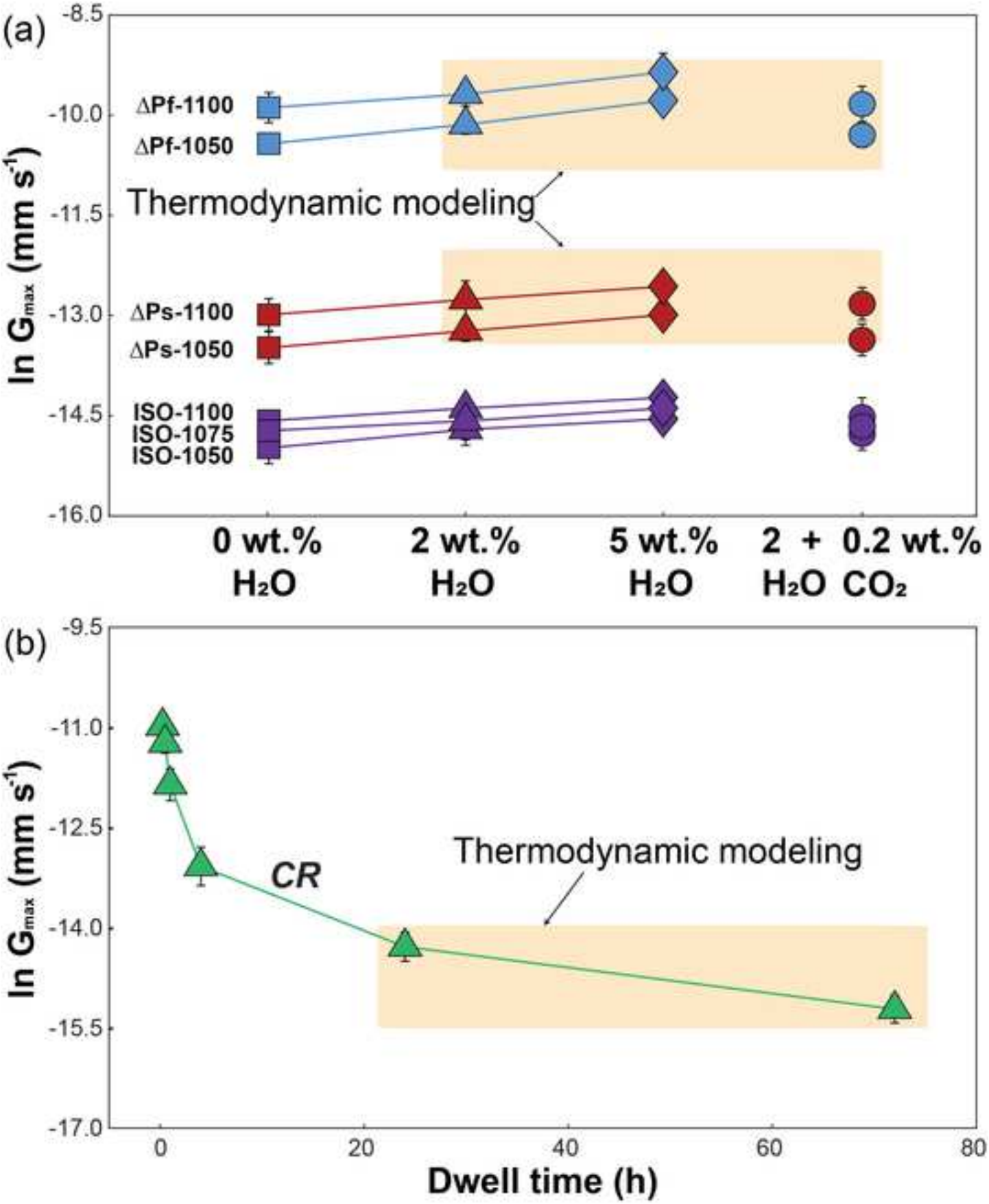

Figure 7

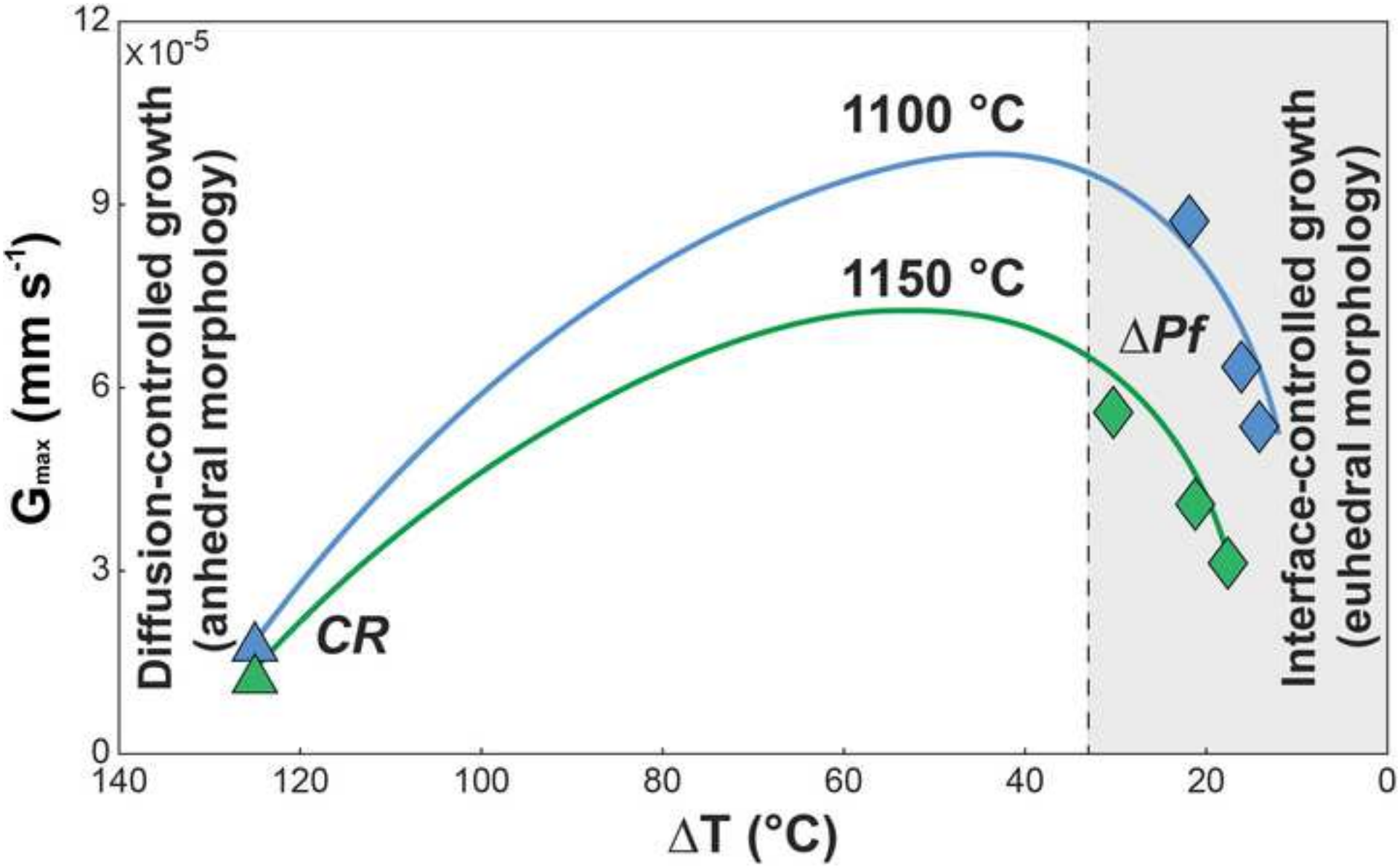

Figure 8

Click here to access/download;Figure;Fig.08.jpg

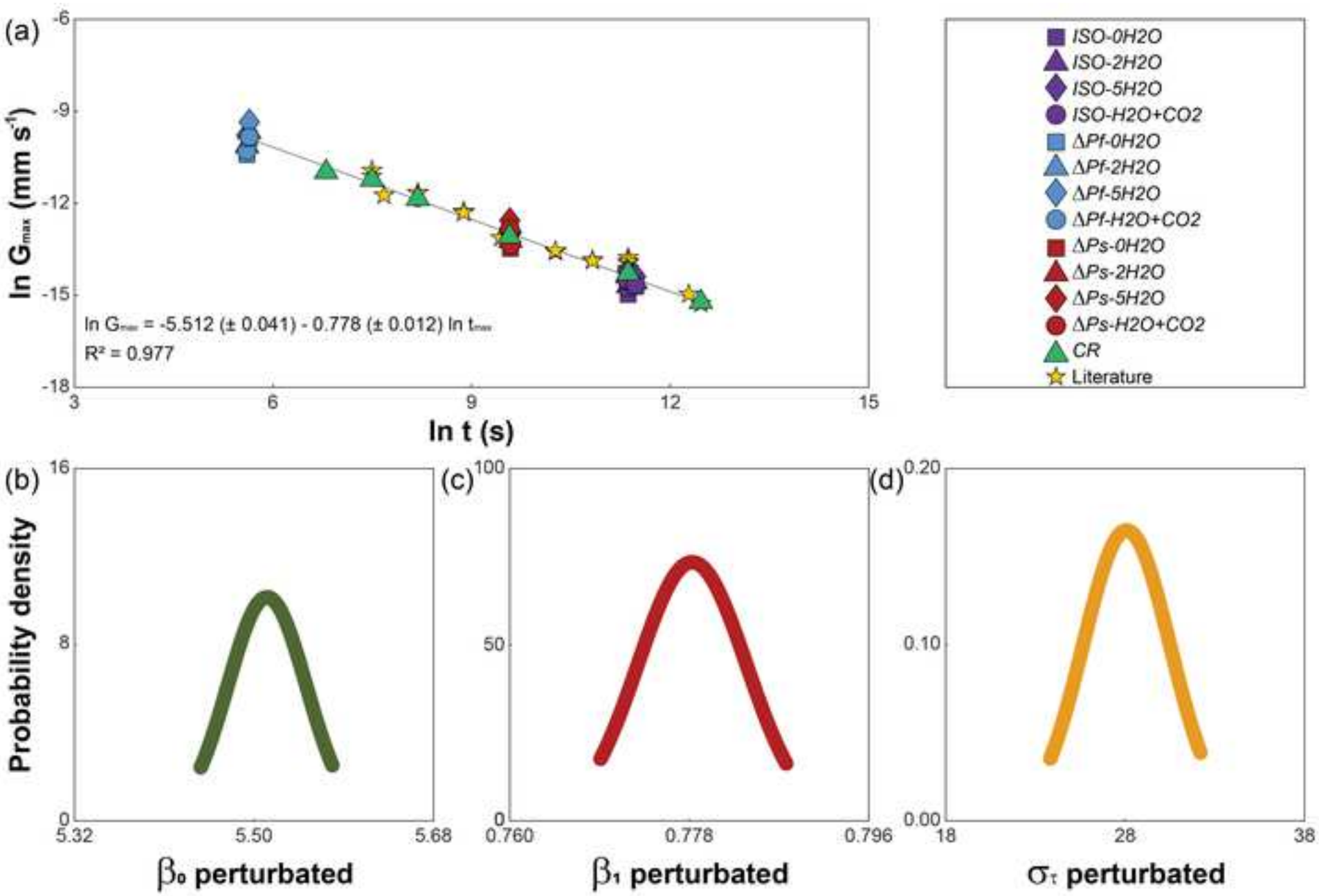

Figure 9

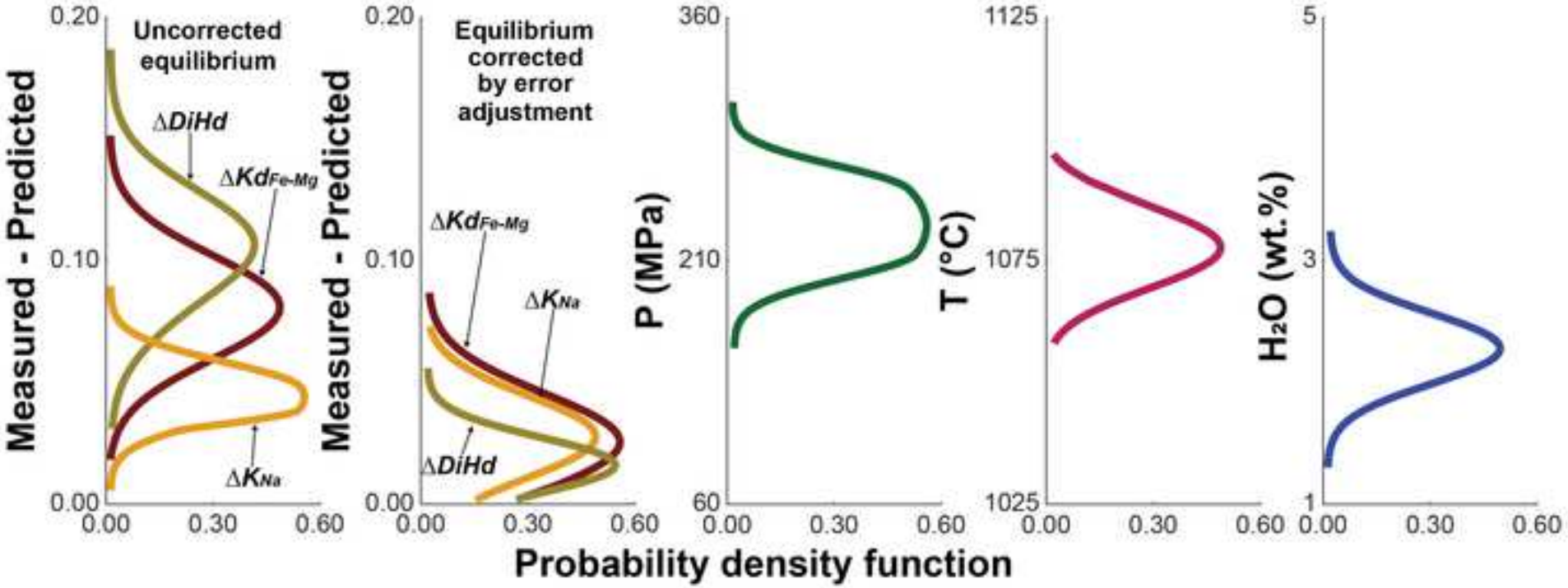

Figure 10

Click here to access/download;Figure;Fig.10.jpg

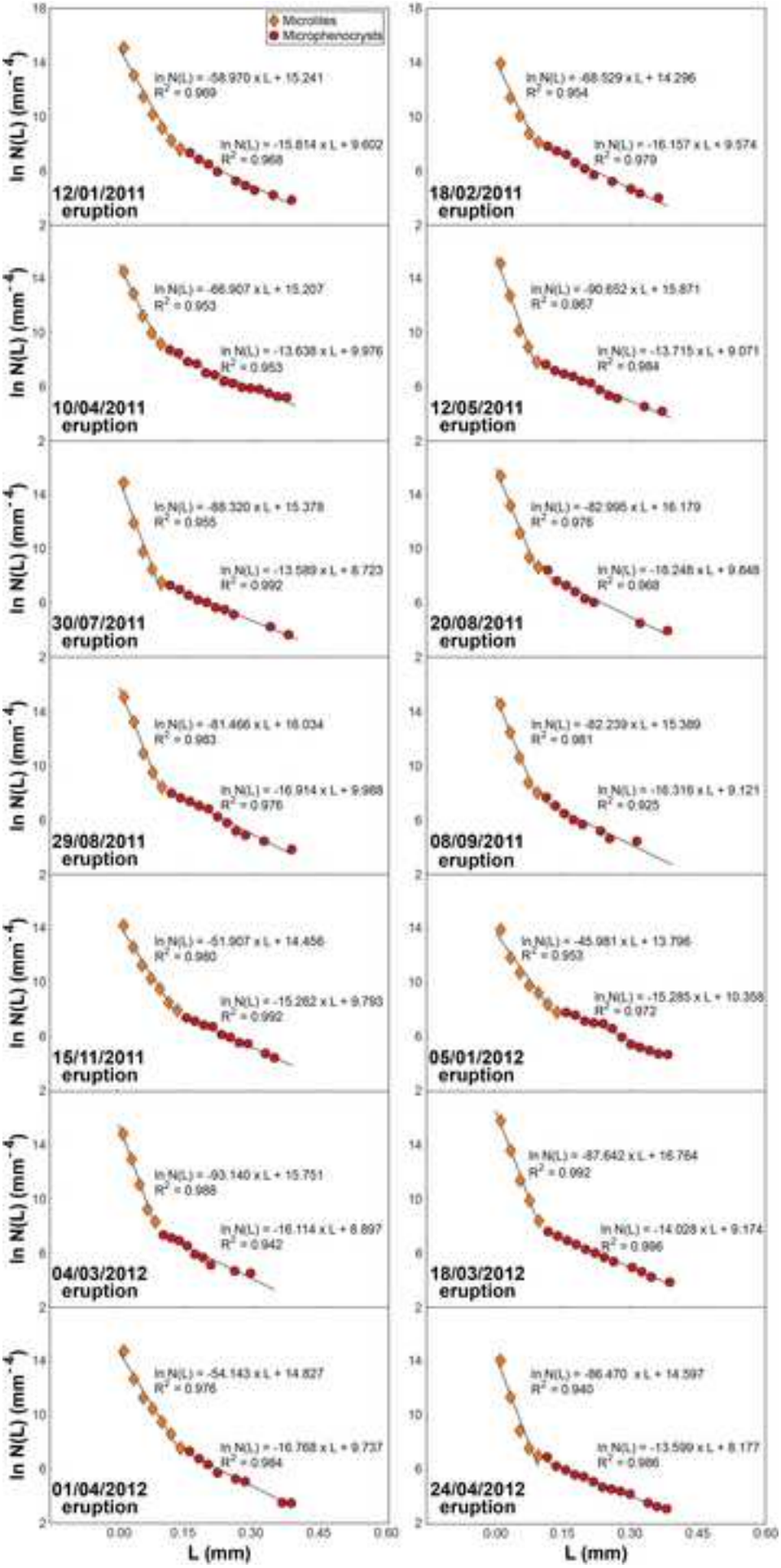

Figure 11

Click here to access/download;Figure;Fig.11.jpg

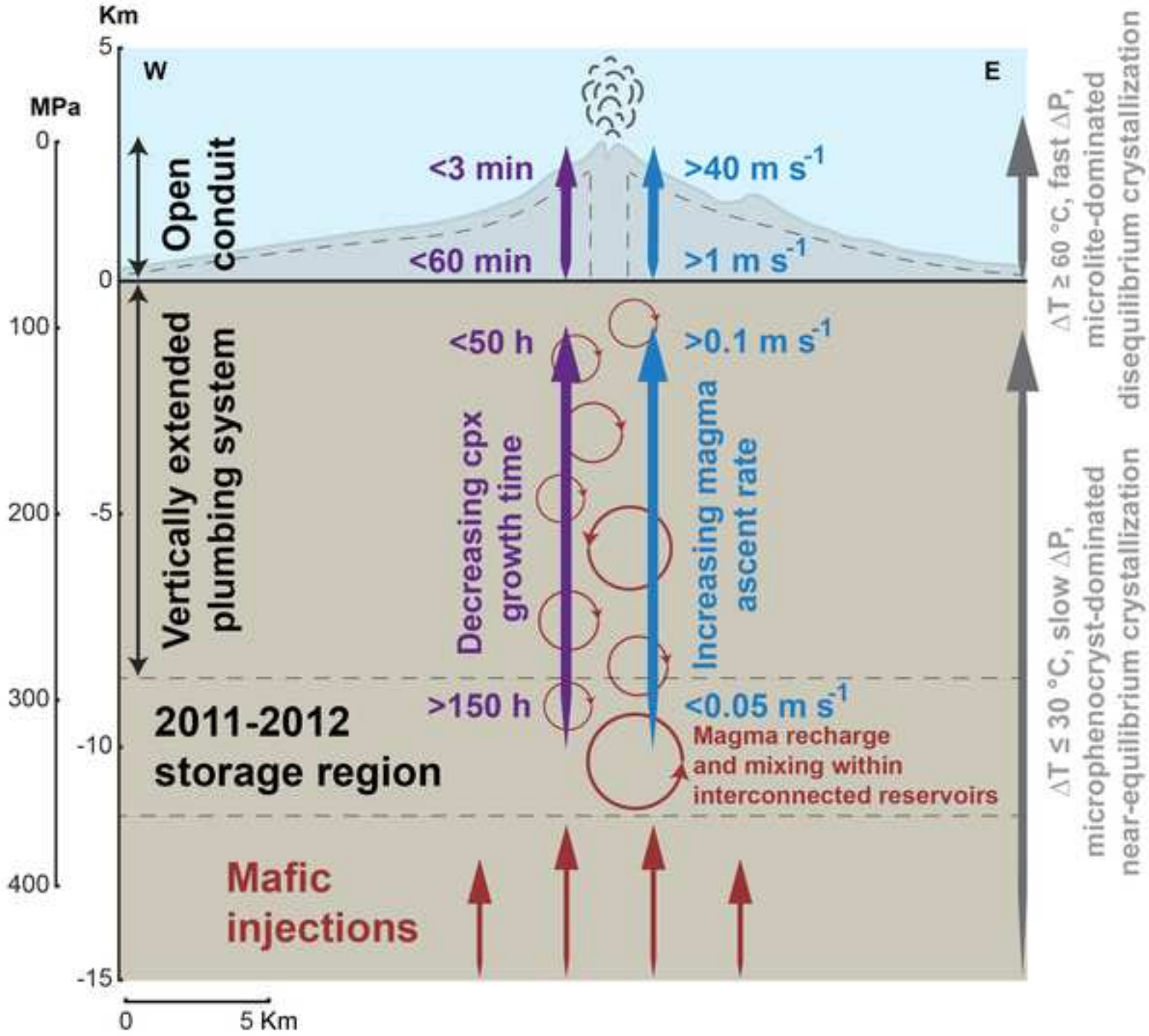

Table 1. Experimental conditions and clinopyroxene textural parameters.

	T (°C)	ΔT (°C)	H_2O (wt.%)	CO_2 (wt.%)	t (h)	fO_2 buffer	P_f (MPa)	ΔP (MPa s^{-1})	CR (°C min^{-1})	$G_{max} \times 10^8$ (mm s^{-1})	Area %	S_v^P (mm^{-1})
Isothermal experiments - 300 MPa												
ISO-1100-0H2O	1100	-	0	-	23.70	NNO+2.1±0.2	-	-	-	46.88±7.1	22.82±0.43	571.43±10.42
ISO-1100-2H2O	1100	-	2	-	23.70	NNO+2.1±0.2	-	-	-	56.45±4.96	20.23±0.38	569.3±10.38
ISO-1100-5H2O	1100	-	5	-	23.70	NNO+2.1±0.2	-	-	-	66.25±3.84	18.77±0.35	476.81±8.7
ISO-1100-H2O+CO2	1100	-	2	0.2	23.70	NNO+2.1±0.2	-	-	-	49.44±8.24	22.12±0.42	568.1±10.36
ISO-1075-0H2O	1075	-	0	-	26.87	NNO+2.1±0.2	-	-	-	40.36±4.13	25.18±0.47	539.67±9.84
ISO-1075-2H2O	1075	-	2	-	26.87	NNO+2.1±0.2	-	-	-	46.7±7.76	20.81±0.39	541.16±9.87
ISO-1075-5H2O	1075	-	5	-	26.87	NNO+2.1±0.2	-	-	-	56.53±5.02	20.13±0.38	523.06±9.54
ISO-1075-H2O+CO2	1075	-	2	0.2	26.87	NNO+2.1±0.2	-	-	-	43.14±4.41	23.32±0.44	577.96±10.54
ISO-1050-0H2O	1050	-	0	-	24.00	NNO+2.1±0.2	-	-	-	31.17±3.68	28.47±0.54	729.64±13.31
ISO-1050-2H2O	1050	-	2	-	24.00	NNO+2.1±0.2	-	-	-	41.09±4.85	24±0.45	586.28±10.69
ISO-1050-5H2O	1050	-	5	-	24.00	NNO+2.1±0.2	-	-	-	48.19±1.94	22.38±0.42	532.11±9.71
ISO-1050-H2O+CO2	1050	-	2	0.2	24.00	NNO+2.1±0.2	-	-	-	38.25±4.51	26.18±0.49	592.65±10.81
Decompression experiments - 300 MPa												
DPf-1100-0H2O	1100	-	0	-	0.08	NNO+2.1±0.2	30	0.965	-	5092.01±565.09	9.12±0.16	281.59±5.13
DPf-1100-2H2O	1100	16	2	-	0.08	NNO+2.1±0.2	30	0.965	-	6240.78±832.28	6.94±0.12	175.67±3.2
DPf-1100-5H2O	1100	22	5	-	0.08	NNO+2.1±0.2	30	0.965	-	8677.78±1090.97	5.14±0.09	112.56±2.05
DPf-1100-H2O+CO2	1100	14	2	0.2	0.08	NNO+2.1±0.2	30	0.965	-	5370.43±684.36	7.93±0.14	240.81±4.39
DPf-1050-0H2O	1050	-	0	-	0.08	NNO+2.1±0.2	30	0.980	-	2970.19±225.2	12.83±0.23	392.86±7.16
DPf-1050-2H2O	1050	20	2	-	0.08	NNO+2.1±0.2	30	0.980	-	3960.26±300.26	11.24±0.2	331.47±6.04
DPf-1050-5H2O	1050	30	5	-	0.08	NNO+2.1±0.2	30	0.980	-	5673.47±558.95	8.4±0.15	226.13±4.12
DPf-1050-H2O+CO2	1050	18	2	0.2	0.08	NNO+2.1±0.2	30	0.980	-	3377.53±307.94	12.18±0.22	358.13±6.53
DPs-1100-0H2O	1100	-	0	-	4.01	NNO+2.1±0.2	30	0.019	-	228.86±26.83	17.13±0.31	417.19±7.61
DPs-1100-2H2O	1100	16	2	-	4.01	NNO+2.1±0.2	30	0.019	-	287.4±38.34	15.12±0.27	375.47±6.85
DPs-1100-5H2O	1100	22	5	-	4.01	NNO+2.1±0.2	30	0.019	-	350.34±24.56	14.34±0.26	273.84±4.99
DPs-1100-H2O+CO2	1100	14	2	0.2	4.01	NNO+2.1±0.2	30	0.019	-	270.06±31.66	16.39±0.29	393.29±7.17
DPs-1050-0H2O	1050	-	0	-	4.05	NNO+2.1±0.2	30	0.018	-	139.81±16.51	21.17±0.38	548.21±10
DPs-1050-2H2O	1050	20	2	-	4.05	NNO+2.1±0.2	30	0.018	-	179.9±14.01	19.14±0.34	517.53±9.44
DPs-1050-5H2O	1050	30	5	-	4.05	NNO+2.1±0.2	30	0.018	-	228.94±7.34	17.38±0.31	436.09±7.95
DPs-1050-H2O+CO2	1050	18	2	0.2	4.05	NNO+2.1±0.2	30	0.018	-	157.29±18.57	20±0.36	537.89±9.81
Cooling rate experiments - 300 MPa												
CR-1050-0.25	1050	125	2	-	0.25	NNO+2	-	-	80	1706.11±134.49	37.11±0.67	1194.08±21.79

CR-1050-0.5	1050	125	2	-	0.5	NNO+2	-	-	80	1323.1±104.61	36.23±0.66	1365.44±24.91
CR-1050-1	1050	125	2	-	1	NNO+2	-	-	80	708.45±83.66	35.81±0.65	1359.31±24.8
CR-1050-4	1050	125	2	-	4	NNO+2	-	-	80	208.29±26.34	33.32±0.6	895.86±16.34
CR-1050-24	1050	125	2	-	24	NNO+2	-	-	80	62.53±6.47	32.38±0.59	847.57±2.74
CR-1050-72	1050	125	2	-	72	NNO+2	-	-	80	24.58±2.53	31.96±0.58	814.87±1.73

Table 2. Clinopyroxene lenght, CSD slope and intercept, maximum growth time and ascent rate of 2011-2012 lava fountains.

Eruption date	Clinopyroxene population	Crystal length (L) (mm)	CSD slope (m) (mm^{-1})	CSD intercept (N_0) (mm^{-4})	Maximum growth time (min)	error (±)	Maximum growth time (h)	error (±)	Ascent rate ($m\ s^{-1}$) 1.5 km depth	error (±)	Ascent rate ($m\ s^{-1}$) 10 km depth	error (±)
12/01/2011	Microlite	L < 0.14	-58.970	15.241	10.85	2.82	0.18	0.05	2.30	0.60	-	-
	Microphenocryst	0.14≤ L <0.4	-15.814	9.602	4122.86	1071.94	68.71	17.87	-	-	0.04	0.01
18/02/2011	Microlite	L < 0.1	-68.529	14.296	5.51	1.43	0.09	0.02	4.54	1.18	-	-
	Microphenocryst	0.1 ≤ L < 0.4	-16.157	9.574	3742.32	973.00	62.37	16.22	-	-	0.04	0.01
10/04/2011	Microlite	L < 0.1	-66.907	15.207	6.14	1.60	0.10	0.03	4.07	1.06	-	-
	Microphenocryst	0.1 ≤ L < 0.4	-13.638	9.976	8039.13	2090.17	133.99	34.84	-	-	0.02	0.01
12/05/2011	Microlite	L < 0.1	-90.652	15.871	1.56	0.41	0.03	0.01	16.04	4.17	-	-
	Microphenocryst	0.1 ≤ L < 0.4	-13.715	9.071	7837.45	2037.74	130.62	33.96	-	-	0.02	0.01
30/07/2011	Microlite	L < 0.1	-88.320	15.378	1.75	0.46	0.03	0.01	14.26	3.71	-	-
	Microphenocryst	0.1 ≤ L < 0.4	-13.589	8.723	8173.49	2125.11	136.22	35.42	-	-	0.02	0.01
20/08/2011	Microlite	L < 0.1	-82.995	16.179	2.32	0.60	0.04	0.01	10.77	2.80	-	-
	Microphenocryst	0.1 ≤ L < 0.4	-16.248	9.848	3648.66	948.65	60.81	15.81	-	-	0.05	0.01
29/08/2011	Microlite	L < 0.1	-81.466	16.034	2.52	0.66	0.04	0.01	9.90	2.57	-	-
	Microphenocryst	0.1 ≤ L < 0.4	-16.914	9.988	3043.65	791.35	50.73	13.19	-	-	0.05	0.01
08/09/2011	Microlite	L < 0.1	-82.239	15.389	2.42	0.63	0.04	0.01	10.34	2.69	-	-
	Microphenocryst	0.1 ≤ L < 0.4	-16.316	9.121	3580.53	930.94	59.68	15.52	-	-	0.05	0.01
15/11/2011	Microlite	L < 0.14	-51.907	14.456	19.30	5.02	0.32	0.08	1.30	0.34	-	-
	Microphenocryst	0.14 ≤ L < 0.4	-15.262	9.793	4839.92	1258.38	80.67	20.97	-	-	0.03	0.01
05/01/2012	Microlite	L < 0.14	-45.981	13.796	33.36	8.67	0.56	0.14	0.75	0.19	-	-
	Microphenocryst	0.14 ≤ L < 0.4	-15.285	10.358	4807.14	1249.86	80.12	20.83	-	-	0.03	0.01
04/03/2012	Microlite	L < 0.1	-93.140	15.751	1.38	0.36	0.02	0.01	18.13	4.71	-	-
	Microphenocryst	0.1 ≤ L < 0.4	-16.114	8.897	3787.60	984.78	63.13	16.41	-	-	0.04	0.01
18/03/2012	Microlite	L < 0.1	-87.642	16.764	1.82	0.47	0.03	0.01	13.77	3.58	-	-
	Microphenocryst	0.1 ≤ L < 0.4	-14.028	9.174	7080.91	1841.04	118.02	30.68	-	-	0.02	0.01
01/04/2012	Microlite	L < 0.14	-54.143	14.827	15.96	4.15	0.27	0.07	1.57	0.41	-	-
	Microphenocryst	0.14 ≤ L < 0.4	-16.768	9.737	3165.10	822.93	52.75	13.72	-	-	0.05	0.01
24/04/2012	Microlite	L < 0.1	-86.470	14.597	1.93	0.50	0.03	0.01	12.96	3.37	-	-
	Microphenocryst	0.1 ≤ L < 0.4	-13.599	8.177	8146.40	2118.06	135.77	35.30	-	-	0.02	0.01